Xenon Saturation Transfer Magnetic Resonance in Model Biological Systems

Im Fachbereich Physik
der Freien Universität Berlin
eingereichte
Dissertation
von

Matthias Schnurr

Berlin 2015

Erster Gutachter: Dr. Leif Schröder
Zweiter Gutachter: Prof. Dr. Robert Bittl

Tag der Disputation: 23. Juli 2015

Hiermit versichere ich, die vorliegende Arbeit selbst und ohne weitere Hilfsmittel, außer den angegebenen, angefertigt zu haben.

_____ Berlin, den _____

Abstract

Xenon (^{129}Xe) nuclei are sensitive probes for nuclear magnetic resonance (NMR) applications. Spin exchange optical pumping yields a significantly increased Xe nuclear spin polarization for studying interactions of the noble gas with other molecules at dilute spin densities. Sensitivity can be further enhanced in dynamic systems where Xe binds reversibly to macromolecular host structures. Such molecules can functionalize the chemically inert atoms, which can then be used as reporters for Hyper-CEST (chemical exchange saturation transfer of hyperpolarized nuclei), a novel and highly sensitive molecular imaging technique.

Here we investigate the Hyper-CEST signatures of exchanging Xe in macromolecular hosts when interacting with dynamic biological model systems. This is required for proper understanding of the Hyper-CEST signal formation.

The tendency of Xe and its hosts to embed into biomembranes was first discovered in 2011. Biomembranes are complex and highly dynamic systems and are diverse in terms of composition. We show that differences in biomembrane composition yield different Hyper-CEST signals, which can be used to generate magnetic resonance imaging (MRI) contrast based on membrane fluidity. This enabled us to detect changes of biomembrane properties in terms of (i) fluidity phase, (ii) lipid raft formation, (iii) cholesterol incorporation and (iv) pore formation, the latter upon antimicrobial peptide action. Moreover, we took advantage of the hydrophobic-driven membrane interaction to deliver Xe hosts as a MRI contrast agent selectively to cells via a peptide-labeled nanocarrier, which bypasses elaborate chemistry of the host molecules. Furthermore, we show that the competitive binding into host molecules between Xe atoms and small organic molecules produced by enzymes can be used to detect enzymatic activity.

The obtained results illustrate that Hyper-CEST can be used as an alternative to optical methods for investigating biomembrane dynamics or enzymatic activity. This can be particularly helpful when existing methods are not applicable, for example fluorescence techniques in combination with opaque samples. Furthermore, the gained knowledge will be substantial when interpreting Hyper-CEST data in biological systems as biomembrane dynamics can interfere with other contrast-relevant parameters, such as Xe host concentration. In particular the development of liposomal nanocarriers will enable Hyper-CEST to be a complementary diagnostic imaging method and help to understand the development, diagnosis and therapy of different diseases, such as cancer.

Kurzzusammenfassung

Xenon-Kerne (^{129}Xe) stellen sehr sensitive Sonden für Kernspinresonanzanwendungen (NMR) dar. Eine deutlich erhöhte Xe-Kernspinpolarisation kann durch optisches Pumpen von Rubidium-Atomen mit darauffolgendem Spinaustausch erreicht werden. Dies ermöglicht Studien über die Wechselwirkung des Edelgases mit anderen Molekülen bei geringer Spin-Dichte. In dynamischen Systemen kann mittels Xe-bindenden Makromolekülen, die Sensitivität zusätzlich erhöht werden. Solche Wirts-Moleküle dienen auch dazu, die chemisch inerten Atome zu funktionalisieren, wodurch eine neuartige sensitive NMR-Anwendung, die auf dem chemischem Austauschsättigungstransfer von hyperpolarisierten Kernen (Hyper-CEST) beruht, möglich wird.

Hier untersuchen wir Hyper-CEST Signaturen von Xe-Atomen und deren Wechselwirkung mit Molekülen, in die sie vorrübergehend binden, in biologisch relevanten Modellsystemen. Diese Studien ermöglichen ein systematisches Verständnis des Hyper-CEST-Signalaufbaus.

Im Jahr 2011 wurde zum ersten Mal die verstärkte Wechselwirkung von Xe-Atomen und deren molekularen Bindungspartnern mit Biomembranen nachgewiesen. Biomembrane sind komplexe und hoch dynamische Systeme, die unterschiedlich aufgebaut sein können. Wir zeigen, dass Unterschiede in der Biomembranzusammensetzung zu unterschiedlichen Hyper-CEST-Signalen führen, was zur Kontrastgenerierung in der NMR-Bildgebung verwendet werden kann. Dies ermöglichte die Detektion von Änderungen unterschiedlicher Biomembraneigenschaften wie (i) der Phase der Biomembranfluidität, (ii) der Separierung solcher Biomembranfluiditätphasen innerhalb einer Biomembran, (iii) der Inkorporierung von Cholesterin und (iv) der Porenbildung, wobei letzteres durch antimikrobielle Peptide induziert wurde. Des Weiteren konnten wir basierend auf der hydrophoben Wechselwirkung des Xe-Kontrastmittels mit Biomembranen Zellen selektiv mittels liposomaler Träger markieren. Dadurch können in Zukunft aufwendige chemische Modifikationen am Wirts-Molekül als Kontrastmittel umgangen werden. Zusätzlich zeigen wir, dass die kompetitive Bindung von Xe-Atomen und von durch Enzyme produzierten organischen Verbindungen mit den Wirts-Molekülen dazu benutzt werden kann, die Enzymaktivität nachzuweisen.

Die erlangten Ergebnisse zeigen, dass Hyper-CEST als Alternative zu optischen Methoden angewendet werden kann, um dynamische Aspekte von Biomembranen oder Enzymaktivität zu untersuchen. Dies kann vor allem dann von Vorteil sein, wenn vorhandene Methoden nicht angewandt werden können, wie zum Beispiel Fluoreszenz bei undurchsichtigen Proben. Weiterhin werden die Ergebnisse entscheidend sein, um Hyper-CEST-Daten von biologischen Systemen korrekt zu interpretieren, da zum Beispiel die Effekte der Biomembrandynamik andere Kontrast-relevante Parameter, wie etwa die Kontrastmittel-Konzentration, überlagern können. Insbesondere durch die Entwicklung des Nanoträgersystems bringen unsere Studien Hyper-CEST einen Schritt weiter, um in Zukunft als komplementäre diagnostische Bildgebungsmethode zu fungieren und damit zum Verständnis über die Entwicklung, Diagnose und Therapie von verschiedenen Krankheiten, wie zum Beispiel Krebs, beizutragen.

Für Emil.

Contents

1 Motivation

Nuclear magnetic resonance (NMR) provides the possibility to sense non-invasively dynamic processes. For example, on the macroscopic scale the diffusion and non-covalent interaction of xenon (Xe) atoms can be used to probe the ventilation of void spaces such as human lungs [1, 2] and the transition from gas phase into blood and tissue. In model solutions of mixed phases, Xe atoms also partition into aqueous and lipid environments [3, 4], which enables investigations of dynamic microscopic processes as they particularly take place in biology.

Biological membranes are dynamical systems and feature high complexity and diversity [5]. Membrane fluidity, which is mainly determined by the membrane components, plays a key role in essential biological functions such as membrane trafficking and signal transduction. Therefore, it is an important parameter in development of diseases. For instance, higher membrane fluidity allows a higher cell metabolism which enhances the malignancy of cancer cells [6, 7] or is a requirement for bacterial cell division [8].

Physics provides many techniques to probe for those membrane properties, and some of them come with the ability of spatial encoding to allow for diagnostic imaging. An emerging field is molecular imaging that can help to understand disease development in general and allows to diagnose diseases specifically to make therapies more efficient [9]. It enables to visualize, characterize and quantify biological processes at cellular and subcellular levels in living organisms [10]. In the past decades the diversity of molecular imaging technologies has increased, but still several challenges remain [11]. The classical different imaging technologies comprise ultrasound, radionuclide, optical, computer tomography, magnetic resonance (MR) techniques and combinations thereof. Beside these, novel techniques are emerging such as Raman imaging [12], photoacoustic imaging [13] and intravital microscopy [14].

Typically, molecular imaging techniques require imaging agents when they are not performed with endogenous tracers. In this thesis we use Hyper-CEST [15], a highly sensitive indirect MR-based detection technique, which uses hyperpolarized Xe atoms as the imaging agent. These can be functionalized through encapsulation in molecular hosts to form sensitive probes. Recently, first in vitro studies of untargeted [16] and targeted [17–20] cell labeling were performed. Both Xe and its molecular hosts favor to partition into biomembrane environment [21], which provides favorable conditions for Hyper-CEST. Based on the efficient partitioning into phospholipid

bilayer, we demonstrate that Hyper-CEST is capable to sense biophysical properties of biomembranes, such as the fluidity and lipid raft formation, which can – among others – be used to generate MRI contrast. Furthermore, we show that beside the dynamics of biomembranes also small organic molecules can influence these signatures which has to be considered when interpreting results, e.g. in terms of concentration determination, in future in vivo experiments.

Xe MRI in the context of existing molecular imaging techniques

As an inexpensive and readily to implement technique ultrasound imaging takes advantage of low-dosed contrast agents that are nontoxic. By varying the ultrasound frequency, it is possible to obtain images of tissue which lies close below the organism's surface as well as from deeper tissue [9]. Also targeted ultrasound contrast agents are available and can be used for drug delivery [22]. However, compared to other existing molecular imaging techniques it lacks sensitivity which is needed to detect disease biomarkers at low concentrations. It also lacks sensitivity to detect membrane internalization of molecular probes.

Higher sensitivity can be obtained by positron emission tomography (PET) and single photon emission computed tomography (SPECT) which detect decaying radionuclides [23]. Although these techniques provide high sensitivity, the obtained images often have high background signal and again, the detected signal is not responsive to membrane internalization. The production of the radioactive tracers can be complex and expensive as they have to be produced close to the imaging modality and are therefore limited available. Furthermore, patients and clinical staff suffer from the radioactive dose.

Optical imaging techniques comprise fluorescence [24] and bioluminescence [25] imaging. Both provide comparable high sensitivity as the radionuclide-based techniques, regarding the possibility to detect low contrast agent concentrations, but are more stable over time as the molecules do not decay radioactively. Fluorescence detection can be tailored to detect membrane-related association, e.g. by Förster Resonance Energy Transfer (FRET). Its main drawback is the restriction to image superficial tissues which makes it commonly used in small animal research. Yet, fluorescence imaging can be clinically applied, for example in breast studies, for which already two-near infrared dyes, methylene blue [26] and indocyanine green [27], have been approved for clinical usage. In contrast to this, bioluminescence can solely be used in small animals research as it requires the gene expression of luciferase.

MRI provides non-invasively high soft-tissue contrast and is in contrast to the optical imaging techniques not restricted by penetration depth. In terms of sensitivity, conventional MRI cannot compete with the radionuclide-based and optical techniques which can result into long acquisition times. However, contrast agents help to decrease this sensitivity gap which can almost be leveled by the possibility to boost the signal of the detected nuclei up to a factor 10^5 through hyperpolarization [28]. Furthermore, MR techniques allow functional imaging through, for example, diffusion weighted

imaging [29]. The possibility to image different nuclei and the extra dimension of chemical shift allow to selectively image for example different target sites or micro-environments [30] similar to multicolor fluorescence imaging which is not possible with radionuclide-based techniques.

As such, the molecular specificity of MRI is therefore not yet fully exploited to develop sensors for interrogating membrane-related parameters.

Structure of the thesis

To provide sufficient background knowledge to the reader, the fundamentals of NMR, with focus on the ^{129}Xe nucleus, are introduced in chapter 2 of this thesis. In chapter 3 the experimental methods which were used during this thesis are discussed in detail. In particular the sensitivity boost that can be obtained through the methodologies of spin hyperpolarization and the indirect detection method Hyper-CEST are described as well as the principle of magnetic resonance image encoding. The methodology chapter ends with a discussion of the properties of the environment of interest, the biological membrane environment.

The experimental results are presented and discussed in chapter 4 as the main part of this thesis. The chapter starts with a detailed investigation of how xenon and its molecular host interact with biological membranes. The following section presents the first ^{129}Xe-NMR studies that were performed on biomembranes that are composed of well-determined lipid mixtures. The gained knowledge allowed us to interpret changes in ^{129}Xe-NMR data, which occurred upon the action of antimicrobial peptide on different biomembranes. The concept that the interaction of Xe and its host cannot only be used to obtain information about biomembranes and their structure, but also to deliver the sensor selectively and biocompatible to cells of the blood brain barrier is demonstrated afterwards. The chapter closes with the presentation of an approach to detect enzymatic activity via competitive binding in ^{129}Xe-NMR.

Lastly, chapter 5 provides an overall summary and discusses the perspectives of ^{129}Xe-NMR in molecular imaging.

2

Xenon NMR fundamentals

2.1 The noble gas xenon

Because of its unexpected discovery, Ramsay named the noble gas he discovered in 1898 "Xenon", referring to the Greek word $\zeta\epsilon\nu o\varsigma$ [xenos] which means foreigner, stranger or guest. For his research on noble gases Ramsay was honored with the Nobel Prize in chemistry in 1904.

With only a concentration of 0.087 ppm Xe is the rarest non-radioactive element in the atmosphere [31]. The inhalation of an air mixture that contains more than 70 % Xe can induce faint [32] and therefore Xe can also be used as an anesthetic with no side effects because of xenon's chemical inertness. This aspect has to be considered for biomedical applications.

The nucleus of a Xe atom consists of 54 protons and can exist in more than 30 isotopes and isomers whereof 9 isotopes occur in nature which are listed in table 2.1. Two of them, ^{124}Xe and ^{136}Xe, decay radioactively, yet with a very long half-life. Because of their non-vanishing nuclear spins the isotopes ^{129}Xe and ^{131}Xe can be detected via NMR. The more than 3 times larger gyromagnetic ratio $\gamma/2\pi$ of ^{129}Xe over the one of ^{131}Xe (-11.777 MHz/T of ^{129}Xe vs. 3.491 MHz/T of ^{131}Xe) makes the detection of ^{129}Xe easier. Additionally its nuclear spin I of $\hbar/2$ does not underly quadrupolar interaction and thus comes along with longer relaxation times compared to ^{131}Xe with a nuclear spin of $3/2\hbar$. The T_1 relaxation time (as a measure for recovery of the Boltzmann population (see section 2.2.3) of ^{129}Xe is several hours in gas phase [33], several minutes dissolved in aqueous solutions [34], around ten seconds in the presence of red blood cells [35] and 3.6 s after arterial injection into a rat brain [36].

Fortunately, with 26.4 % the natural abundance of ^{129}Xe is relatively high compared to the other Xe isotopes, yet low compared to the 99.99 % natural abundance of the NMR detectable hydrogen (^{1}H) atoms in H_2O molecules.

Table 2.1 – Properties of the naturally occurring Xe isotopes. Adapted from [37].

Isotope	I / $\hbar$	$\gamma/2\pi$ $\frac{\text{MHz}}{\text{T}}$	nat. abundance / %	half life
^{124}Xe	0		0.09	$> 4.8 \times 10^{16}$ a[a]
^{126}Xe	0		0.09	stable
^{128}Xe	0		1.92	stable
^{129}Xe	1/2	11.8	26.44	stable
^{130}Xe	0		4.08	stable
^{131}Xe	3/2	3.5	21.18	stable
^{132}Xe	0		26.89	stable
^{134}Xe	0		10.44	stable
^{136}Xe	0		8.87	$> 10 \times 10^{21}$ a[b]

[a]: radioactive decay via double electron capture

[b]: radioactive decay via double beta decay

2.2 Basics of Nuclear Magnetic Resonance

Nuclear Magnetic Resonance (NMR) is based on a quantum mechanical phenomenon. However, several different fields in physics and chemistry rely on NMR applications. The existence of a quantum mechanical property, termed spin, was initially proposed by Uhlenbeck and Goudsmit in 1925 [38] to be able to explain certain properties of optical spectra of atoms. This property is linked to a magnetic moment which can be probed in magnetic resonance experiments. In the following years Felix Bloch [39] and Edward Mills Purcell [40] performed independently from each other the first NMR experiments on condensed matter for which both were honored with the 1952's Nobel Prize in physics. Paul C. Lauterbur [41] and Sir Peter Mansfield [42] received the Nobel Prize in Physiology or Medicine in 2003 for their contributions to the development of Magnetic Resonance Imaging (MRI).

This thesis cannot offer an in-depth discussion of all theory of NMR spectroscopy and imaging. Instead, it will focus on a short description of the basic quantum mechanical principles of NMR and the more exotic principles that are essential for the understanding of the presented research will be introduced.

2.2.1 Nuclear spin

The nucleus of hydrogen (^{1}H) contains only a single proton and no neutron, whereas the nucleus of a ^{129}Xe atom is composed of 54 protons and 75 neutrons. Basically, protons and neutrons consist of three "constituent" quarks each, *uud* and *udd* respectively, and gluons which bind these quarks together. The nucleons have a spin $I = \hbar/2$. However, this picture is only true in low-energy systems, as it is the case in NMR experiments. In high-energy physics experiments the components of the nucleons can be described through almost massless "current" quarks which are surrounded by a sea

of quark-antiquark pairs and gluons [43]. This can also change the spin configuration. For instance, the spin-state $I = 3/2\hbar$ of the proton is known as the Δ^+ particle.

The simple structure of a ^{1}H nucleus with one proton gives it a spin $\hbar/2$. In a ^{129}Xe nucleus the single spins of the nucleons add up to a total spin, which is $\hbar/2$.

A spin $\hat{\vec{I}}$ is a quantum mechanical property of a particle for which the same mathematical description obeys as for the classical definition of angular momentum. Its rotations around different axis do not commutate and the fundamental commutation relation of the spin components $\hat{I}_k$ obeys

$$\left[\hat{I}_k, \hat{I}_l\right] = i\hbar\epsilon_{klm}\hat{I}_m \tag{2.1}$$

Because of this relation $\hat{I}^2$ commutates with the spin component $\hat{I}_z$ and every quantum mechanical spin state $|I, m_z\rangle$ is uniquely defined by its angular momentum quantum number I and magnetic spin quantum number m_z. Thus the equations that describe the eigenstates of a spin are

$$\begin{aligned} \hat{I}^2 |I, m_z\rangle &= \hbar^2(I(I+1)) |I, m_z\rangle \\ \hat{I}_z |I, m_z\rangle &= m\hbar |I, m_z\rangle . \end{aligned} \tag{2.2}$$

2.2.2 Magnetic moment

Every nuclear spin possesses a magnetic moment $\vec{\mu}$ that is proportional to $\vec{I}$:

$$\hat{\vec{\mu}} = \gamma\hat{\vec{I}} = \frac{ge}{2Mc}\hat{\vec{I}} \tag{2.3}$$

The constant γ is known as the gyromagnetic ratio that is specific for every particle or nucleus as it depends on its mass M and on the Landé factor g. The Landé factor of a proton is $g_{\text{proton}} \approx 5,586$ whereas of a neutron it is $g_{\text{neutron}} \approx -3,826$. In equation 2.3, e is the elementary charge and c the speed of light.

If a non-vanishing magnetic field $\vec{B}_0$ is present at the position of a magnetic moment, its m degenerate energy levels split into $2I + 1$ defined energy levels. This energy splitting is called Zeeman splitting and can be described by the action of the Hamiltonian

$$\begin{aligned} \hat{H} &= -\hat{\vec{\mu}} \cdot \vec{B}_0 = -\gamma\hat{\vec{I}} \cdot \vec{B}_0 \\ &\Downarrow \\ \hat{H} |I, m_z\rangle &= -\gamma m\hbar B_0 |I, m_z\rangle . \end{aligned} \tag{2.4}$$

Where we used the assumption $\vec{B}_0 = (0, 0, B_0)$, without loss of generality. Hence, a nucleus with spin $\hbar/2$ that has the two quantum numbers $m = \pm 1/2$ can be in two distinct energy states, denoted by $m = +1/2$ and $m = -1/2$. The energy gap between them is given by

$$\Delta E_0 = \hbar\gamma B_0 = \hbar\omega_0, \tag{2.5}$$

with $\omega_0 = \gamma B_0$. This means that a nuclear spin system with the gyromagnetic ratio γ shows a resonant transition under irradiation with frequency ω_0 when it is in the magnetic field B_0. For ^{129}Xe, one observes $\omega_0 = 110.71$ MHz at a magnetic field strength of 9.4 T.

Time evolution of magnetic moments

The dynamics of a magnetic moment can by described by the Heisenberg equation where the states are time-independent and the operators are time-dependent:

$$\frac{d\hat{\mu}(t)}{dt} = \frac{1}{i\hbar}\left[\hat{\mu}(t), \hat{H}\right] + \frac{\partial\hat{\mu}(t)}{\partial t} \tag{2.6}$$

In general $\hat{\mu}(t)$ does not change explicitly over time and thus the partial derivative in equation 2.6 can be neglected. Because of the time-independence of the states, it can be written

$$\left\langle \frac{d\hat{\mu}(t)}{dt} \right\rangle = \langle\cdot|\frac{d\hat{\mu}(t)}{dt}|\cdot\rangle = \frac{d}{dt}\langle\cdot|\hat{\mu}(t)|\cdot\rangle = \frac{d}{dt}\langle\hat{\mu}(t)\rangle\,. \tag{2.7}$$

Thus,

$$\frac{d\langle\hat{\mu}(t)\rangle}{dt} = \frac{1}{i\hbar}\left\langle\left[\hat{\mu}(t), \hat{H}\right]\right\rangle. \tag{2.8}$$

Inserting the definition of $\hat{\mu}$ from equation 2.3 and the Hamiltonian from equation 2.4 we get

$$\frac{d\langle\hat{\mu}(t)\rangle}{dt} = \frac{-\gamma^2}{i\hbar}\left\langle\left[\hat{\vec{I}}(t), \hat{\vec{I}}\vec{B}_0\right]\right\rangle. \tag{2.9}$$

This commutator does only vanish if the components of $\hat{\vec{I}}$ and $\hat{\vec{I}}\vec{B}_0$ are the same, otherwise

$$\frac{d\langle\hat{\mu}(t)\rangle}{dt} = \frac{-\gamma^2}{i\hbar}\left\langle\left[\hat{I}_k(t), \hat{I}_l B_{0l}\right]\right\rangle, \text{with } k \neq l. \tag{2.10}$$

With equation 2.1 we obtain

$$\begin{aligned}\frac{d\langle\hat{\mu}(t)\rangle}{dt} &= \frac{-\gamma^2}{i\hbar}\left\langle i\hbar\,\epsilon_{klm}\hat{I}_k(t)B_{0l}\right\rangle \\ &= \gamma^2\,\epsilon_{kml}\langle\hat{I}_k(t)\rangle B_{0l} \\ &= \gamma^2\,\langle\hat{\vec{I}}(t)\rangle \times \vec{B}_0 \\ &= \gamma\,\langle\hat{\vec{\mu}}(t)\rangle \times \vec{B}_0.\end{aligned} \tag{2.11}$$

The magnetic moment of a spin cannot be measured with conventional NMR techniques. However, one can measure the macroscopic magnetization, which is the sum over the expectation values of all magnetic moments:

$$\vec{M} = \frac{1}{V}\sum_{i=1}^{N}\langle\vec{\mu}_i\rangle \tag{2.12}$$

Combining equations 2.12 and 2.11 with an arbitrary magnetic field $\vec{B}(t)$ yields the classical equation of motion of a gyroscope

$$\frac{d\vec{M}(t)}{dt} = \gamma\, \vec{M}(t) \times \vec{B}(t). \tag{2.13}$$

Hence, the magnetization precesses in a constant magnetic field exactly as a gyroscope that moves freely (without any friction) in a gravitational field. The Larmor frequency with which the magnetization precesses in the magnetic field equals the resonance frequency ω_0 that defines the energy gap in between the energy states of the spins.

2.2.3 Bloch equations

The equilibrium condition is characterized by

$$\frac{d\vec{M}(t)}{dt} = 0. \tag{2.14}$$

and thus $\vec{M}(t=0)$ is parallel to $\vec{B_0} = (0, 0, B_0)^T$. With a radio frequency (rf) pulse $\vec{B_1}$ that is (i) in resonance with the precession frequency ω_0 of the nuclear spins and (ii) has a component that is perpendicular to $\vec{B_0}$, the magnetization can be flipped into the transversal xy-plane where the magnetization starts to precess around the axis of $\vec{B_0}$.

The precession does not last forever, because of interactions affecting the spins. The strongest interactions are the spin-spin interaction and the spin-lattice interaction. Therefore, the time evolution of the magnetization, described through equation 2.13, has to be extended. The phenomenological extension was found by Felix Bloch in 1946 [39] and is known as the Bloch equations

$$\frac{dM_x(t)}{dt} = \gamma(\vec{M}(t) \times \vec{B}(t))_x - \frac{M_x(t)}{T_2} \tag{2.15}$$

$$\frac{dM_y(t)}{dt} = \gamma(\vec{M}(t) \times \vec{B}(t))_y - \frac{M_y(t)}{T_2} \tag{2.16}$$

$$\frac{dM_z(t)}{dt} = \gamma(\vec{M}(t) \times \vec{B}(t))_z - \frac{M_z(t) - M_0}{T_1}. \tag{2.17}$$

Where M_0 is the total magnetization along $\vec{B_0}$ for $t \to \infty$.

Using Faraday induction in the rf coil of a MR experiment, only the transversal components M_x and M_y can be measured. These two components can be summarized as $M_\perp = M_x + iM_y$. With the assumption of a constant magnetic field $\vec{B_0}$ one can simplify the Bloch equations to

$$\frac{dM_\perp(t)}{dt} = -(i\omega_0 + 1/T_2)M_\perp(t) \tag{2.18}$$

$$\frac{dM_z(t)}{dt} = \frac{M_0 - M_z(t)}{T_1}. \tag{2.19}$$

This system of differential equations can be solved by the exponential functions

$$M_\perp(t) = M_\perp(0)e^{-(i\omega_0+1/T_2)t} \tag{2.20}$$

$$M_z(t) = M_z(0)e^{-t/T_1} + M_0(1 - e^{-t/T_1}). \tag{2.21}$$

Where $M_\perp(0)$ and $M_z(0)$ are the transversal and the longitudinal magnetization at $t = 0$. In a frame that rotates with the frequency ω_0 around the z-axis, $M_z(t)$ does not change whereas $M_\perp(t)$ becomes

$$M'_\perp(t) = M'_\perp(0)e^{-t/T_2}. \tag{2.22}$$

Thus, the time constants T_1 and T_2 are the characteristic times with which $M_z(t)$ is re-established along $\vec{B_0}$ (governed by T_1) and $M_\perp(t)$ vanishes (governed by T_2). They differ for different nuclei in different environments and are important measurement parameters in NMR and MRI.

2.2.4 Chemical shift of ^{129}Xe

Maybe the most powerful property of NMR over other imaging methods is its spectral selectivity. Different magnetic environments caused by the presence of different atoms or molecules in the area around the nucleus of interest yield local perturbations of the external magnetic field strength B_0 experienced by the nucleus of interest. This yields to a change in the nuclear spin resonance frequency $\omega_0 = -\gamma B_0$ to

$$\tilde{\omega} = -\gamma\tilde{B_0} = -\gamma(1 - [\sigma])B_0. \tag{2.23}$$

The shielding or deshielding is represented by the chemical shift tensor $[\sigma]$. In gaseous and liquid phase the fast rotation of the molecules averages the tensor's anisotropic terms to zero and $[\sigma]$ can be reduced to the scalar σ.

The potential of NMR to distinguish nuclei via their signature resonance frequency through the linear dependency on the external magnetic field, seems to be perturbed by σ. However, by referencing the resonance frequency $\tilde{\omega}$ to another resonance frequency ω_0, the measured signal becomes independent of the external magnetic field B_0. It is defined as the dimensionless chemical shift δ:

$$\delta = \frac{\tilde{\omega} - \omega_0}{\omega_0} \tag{2.24}$$

The difference in the numerator usually is in the order of Hz, whereas the resonance frequencies are in the range of MHz. Therefore, the chemical shift is generally given in ppm.

In ^{129}Xe experiments the chemical shifts are usually referenced to the gaseous ^{129}Xe signal, which is set to 0 ppm [44]. Because of xenon's large polarizable electron cloud, the chemical shift tensor can vary strongly. This results into very large chemical shifts (up to ca. 7500 ppm for chemical compounds such as XeO_6^{4-}) compared to protons,

Table 2.2 – Chemical shifts of ^{129}Xe in selected molecular environments that are relevant for the field of xenon biosensors.

Molecular environment	δ / ppm	note[a]	Ref.
gaseous Xe	0	by definition	
Xe in H_2O	193.8	295 K, 0.04 ppm/K	[46]
Xe in lipids	194[b]	298 K, −0.3 ppm/K	[21]
Xe@CrA	62.7	295 K, 0.3 ppm/K	[21, 46]
Xe@CrA$_{\text{lipid}}$	73	297 K, 0.2 ppm/K	[21, 47]
Xe@CrA$_{\text{cells}}$	71	310 K	[16, 19, 20]
Xe@CrA on M13-phage	64.6	310 K	[48]
Xe@PFOB	111[c]	310 K	[49]
Xe@CB6	95[d]	293 K	
Xe@CB7	105[d]	293 K	

[a]: temperature and temperature dependence of δ, if available

[b]: depends on lipid concentration, overlaps with the resonance of Xe in H_2O, only resolvable at low temperatures or in presence of multilamellar vesicles

[c]: changes with nanoemulsion droplet size

[d]: see results in section 4.5

which have a typical chemical shift range of ca. 15 ppm. The large chemical shift range in ^{129}Xe NMR allows favorable spectral selectivity. For example the separation between the resonance of free Xe dissolved in H_2O and the resonances of Xe associated with different biosensors is in most cases larger than 100 ppm. Table 2.2 gives an overview of chemical shifts in selected molecular environments that are relevant for the field of xenon biosensors. Noteworthy is the downfield shift of the resonance in lipid environment compared to aqueous solutions. This counterintuitive behavior with respect to polarity is presumably a result of weak surface interactions between xenon atoms and the lipid molecules in solution, as suggested in [21]. The suggestion is based on a similar downfield shift of the Xe resonance in aqueous solution that occurs when adding denaturated proteins to the solution [45].

2.2.5 Polarization of a ensemble of nuclei

A spin system with an external defined temperature T represents a canonical ensemble. Therefore, the probability P for a spin being in the state $|I, m_z\rangle$ with the energy eigenvalue E_m is given by

$$P(E_m) = \frac{e^{-E_m/k_B T}}{Z} \tag{2.25}$$

with the canonical partition function

$$Z = \sum_m e^{-E_m/k_B T}. \tag{2.26}$$

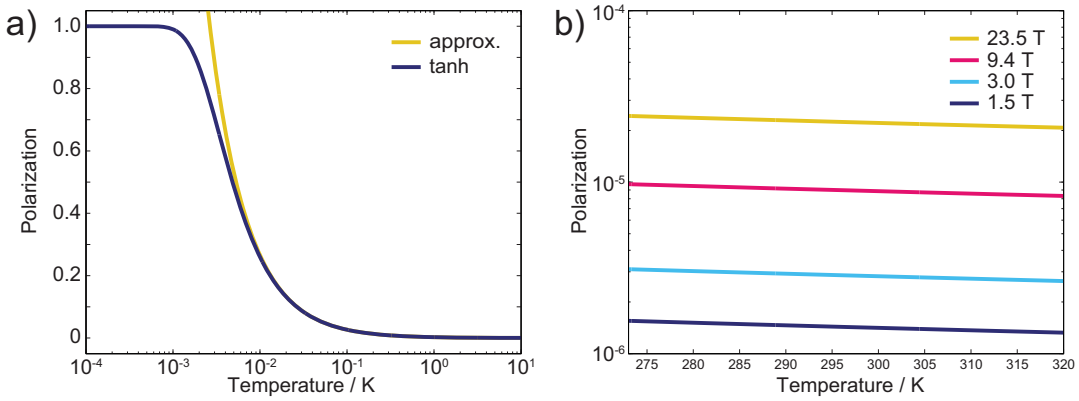

Figure 2.1 – Polarization of a ^{129}Xe spin ensemble in dependence of the temperature (equation 2.27). a) illustrates the validation of the approximation for $T \geq 0.01$ K at 9.4 T and b) compares the polarization for different B_0 field strengths around 300 K.

Hence, the polarization of a ensemble of spins that contains only nuclei with spin $\hbar/2$ is given by

$$P = \frac{e^{\frac{\mu B_0}{k_B T}} - e^{-\frac{\mu B_0}{k_B T}}}{e^{\frac{\mu B_0}{k_B T}} + e^{-\frac{\mu B_0}{k_B T}}} = \tanh\frac{\mu B_0}{k_B T} = \tanh\frac{\gamma\hbar B_0}{2k_B T} \xrightarrow{T\geq 1\,\mathrm{K}} \frac{\gamma\hbar B_0}{2k_B T}. \tag{2.27}$$

For ^{129}Xe nuclei in a magnetic field of $B_0 = 9.4$ T, as in the experiments of this thesis, the last approximation is already valid for $T \geq 0.01$ K as illustrated in Figure 2.1 a). For $T \leq 0.1$ K the polarization becomes significantly larger with decreasing temperature. However, at more practical temperatures and temperatures relevant for medical applications, around 300 K, the thermal polarization of the ^{129}Xe spin ensemble is only 10^{-5} and does not change significantly when changing B_0 in the range of today's available field strengths as illustrated in Figure 2.1 b). Thus the NMR detection of thermally polarized ^{129}Xe spins is very challenging or requires a lot of signal averaging.

3 Methodology

3.1 Boosting sensitivity in Xe NMR

A theoretical maximum polarization of 100 % can almost be achieved without requiring very low temperatures or very large magnetic field strengths by forcing the spin ensemble into a non-equilibrium state [50–55]. Polarizations that exceed the thermal polarization are termed hyperpolarization. In general a hyperpolarized ensemble can be produced through various methods, namely dynamic nuclear polarization (DNP) [56, 57], parahydrogen induced polarization (PHIP) [58, 59] or spin exchange optical pumping (SEOP) [60]. Table 3.1 gives an overview of the different methods and their maximum reported nuclear polarization. DNP can produce polarizations up to 64 % [61] by transferring the microwave induced free radical electron polarization to any NMR-detectable nuclei. With PHIP polarizations up to 30 % are reported [62]. It takes advantage of the very long T_1 relaxation time (up to one year) of the para-hydrogen hyperpolarization and transfers it via J-coupling to other NMR-detectable nuclei. The largest polarizations (up to 70 % [55]) can be obtained through SEOP. However, it is restricted to noble gases such as ^{3}He and ^{129}Xe. In this thesis SEOP was used for the production of hyperpolarized ^{129}Xe and is described in the following.

3.1.1 Sensitivity boost I: Spin exchange optical pumping (SEOP)

It is not possible to manipulate the two spin state system of ^{129}Xe nuclei directly to obtain a hyperpolarized spin ensemble, e.g. by irradiating a rf pulse. A third energy level is needed to efficiently pump the atoms and to obtain an overpopulation of one state. The overpopulation of one of the two nuclear states of ^{129}Xe can be achieved by

Table 3.1 – Overview of different methods to hyperpolarize different nuclei and their maximum reported polarization.

Method	Applicable nuclei	Reported polarization	Ref.
DNP	all	up to 64 %	[61]
PHIP	^{1}H $\rightarrow$ ^{13}C, ^{15}N, ^{19}F, ...[a]	up to 30 %	[62]
SEOP	noble gases; mainly ^{129}Xe and ^{3}He	60 – 70 %	[55]

[a]: polarization transfer through J-coupling

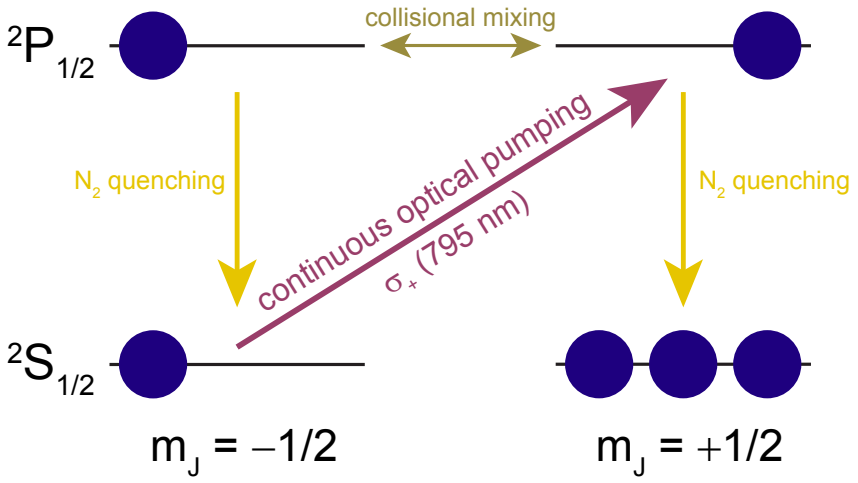

Figure 3.1 – Optical pumping of the electrons of rubidium atoms with right-handed circularly polarized light at 795 nm. The continuous pumping of the $m_J = -1/2$ sublevel of the $^2S_{1/2}$ ground state combined with non-radiative relaxation through N_2 quenching and collisions with other atoms yields an overpopulation of the $m_J = +1/2$ sublevel.

making a detour via other atoms which than interact through their pumped state with the ^{129}Xe nuclei. Spin exchange optical pumping (SEOP) is the method used in this thesis to produce hyperpolarized ^{129}Xe. Basically, SEOP is a two-step process. First an alkali metal vapor has to be pumped optically to generate an electron polarization. In the second step the obtained excited electron spin state is transferred to the nucleus of the noble gas yielding a hyperpolarized nuclear spin ensemble. Both steps are described in the following.

Optical pumping of alkali metals

In 1950 the base for spin exchange optical pumping, the optical pumping of alkali metals via circular polarized light, was for the first time experimentally studied by Alfred Kastler [63]. Later in 1966 he was honored with the Nobel Prize in physics for the discovery and development of optical methods for studying Hertzian resonances in atoms. Alkali metals can easily be excited by optically pumping the single valence electron in the most outer atomic orbital via laser light. The good availability of relatively cheap, high-quality and high-power laser sources that are suitable to pump the D1 transition at 795 nm is the main reason why Rb is the alkali metal of choice in most SEOP processes. Furthermore, a deliberate high vapor pressure with a high density can easily be obtained by heating Rb above its low melting point at 39.5 °C [64]. The pumping cell containing the Rb vapor is placed in a homogeneous external magnetic field which causes Zeeman splitting of the electronic states of the Rb atoms.

Figure 3.1 illustrates the continuous optical pumping of Rb's ground state $^2S_{1/2}$. In the setup used in this thesis a laser source with 150 W continuous wave total output power transitions the energy gap of ca. 1.56 eV between the ground state and the

first excited state $^2P_{1/2}$. Right-handed circularly polarized light is required to pump the transition between the sublevels $m_J = -1/2$ and $m_J = +1/2$ only, because of the quantum mechanical selection rule $\Delta m = 0, \pm 1$ and the conservation of the total spin number. The lifetime of the obtained excited state is reduced by collisions with other atoms and deliberate N_2 quenching. Latter causes a non-radiative decay of the excited Rb atoms, by transferring the energy into rotational and vibrational motion of the N_2 molecules[1]. The non-radiative manner of the decay is important because otherwise the photons emitted by natural decay could depolarize other excited Rb atoms. The continuous depletion of the $m_J = -1/2$ sublevel of the $^2S_{1/2}$ ground state combined with the forced decay of the excited $^2P_{1/2}$ states results into an overpopulation of the $m_J = +1/2$ sublevel of the $^2S_{1/2}$ ground state. The larger this overpopulation is, the larger is the Rb electron polarization. Under optimal SEOP conditions with optimized pumping parameters such as pumping time, pressure and temperature the Rb electron polarization can approach 100 % and is given by [60]

$$P_{\mathrm{Rb}} \approx \frac{s_z R}{\gamma_{\mathrm{SD}} + R}, \tag{3.1}$$

where $s_z = \hbar\sigma_z$ and σ_z is the z-component of the Pauli matrix of the photons of the laser light. R is the pumping rate with which the Rb electrons are pumped to the $m_J = +1/2$ sublevel of the excited $^2P_{1/2}$ state by the photons. The rate γ_{SD} describes the depolarization ("spin destruction") of the Rb atoms [60, 66]. To get an optimal Rb polarization high laser powers with an optimal pumping rate R are beneficial to obtain $R >> \gamma_{\mathrm{SD}}$, because the Rb polarization process is a competition between the optical pumping rate and the spin destruction rate γ_{SD}.

In general several factors contribute to γ_{SD}:

$$\gamma_{\mathrm{SD}} = \kappa_{\mathrm{Xe}}[Xe] + \kappa_{\mathrm{Rb}}[Rb] + \kappa_{\mathrm{N_2}}[N_2] + \kappa_{\mathrm{He}}[He] + \gamma_{\mathrm{trap}} + \gamma_{\mathrm{SE}} \tag{3.2}$$

In equation 3.2 γ_{SD} depends on the spin destruction coefficients κ_X and the partial pressure densities $[X]$, where X stands for the participating atoms Rb, Xe and He or the molecule N_2. The rate γ_{trap} represents the depolarization through radiation trapping due to naturally decaying Rb atoms. The last term γ_{SE}, termed spin exchange rate, is the rate by which the electron polarization is transferred to the ^{129}Xe nuclei. This represents the second major step in SEOP and is discussed below.

Spin exchange to the noble gas

The transfer of the Rb electron polarization to the ^{129}Xe nuclei is given by the spin exchange rate γ_{SE}. The spin can be exchanged via two ways: either in binary

[1] The natural linewidth of Rb's D1 transition is $2\pi \cdot 5.75$ MHz [64]. At high temperatures the Doppler effect increases the linewidth to ca 250 MHz [65]. Still, this is much narrower than the laser light bandwidth which is narrowed down to 0.5 nm (equiv. to 237 GHz) using volume Bragg grating. Pressure broadening aims to reduce this large difference.

collisions or via the formation of short-lived Rb-^{129}Xe-N_2 clusters due to van-der-Waals interactions. At high pressure, as used in the experiments, the lifetime of the van-der-Waals induced clusters is short (ca. 1 ns) and their contribution to the spin exchange is negligible [67]. The binary collisions which cause the spin exchange between the optically pumped Rb electrons and the ^{129}Xe nuclei can be described as isotropic, magnetic hyperfine interactions. The interaction arises from the Fermi-contact magnetic field produced by the two atoms which perturbs the wave function at the ^{129}Xe nucleus in the presence of the Rb atom compared to the absence of the Rb atom [60]. The absolute value of the perturbation factor η is largest for ^{129}Xe ($|\eta| = 50$) of all noble-gas atoms (for ^{3}He $|\eta| = 9.5$) [60]. Thus the isotropic hyperfine interaction is larger between Rb and Xe than between Rb and He. Furthermore, the spin-exchange cross section of Rb-Xe collisions is with approximately 18000 barn much larger than 2 barn for Rb-He collisions [60][2]. Thus, both, the larger perturbation factor and the much larger spin-exchange cross section for Rb-Xe pairs compared to Rb-He pairs, allow a much more efficient production of hyperpolarized ^{129}Xe than hyperpolarized ^{3}He using SEOP. A better way to obtain hyperpolarized ^{3}He is metastable exchange optical pumping [68].

Once the spins are exchanged to the ^{129}Xe nuclei, they can loose their polarization in collisions with other atoms or molecules or by interacting with the surface of the experimental setup, such as the glass wall of the pumping cell or the plastic tubes that guide the hyperpolarized gas to the NMR spectrometer or MR scanner. This depolarization rate is given by γ_w. Antirelaxation surface coatings on the glass wall of transport containers can reduce T_1 spin relaxation and enable to ship hyperpolarized noble gases for example from Germany to Australia. Often a high-purity aluminosilicate sol-gel film is used as surface coating [69]. The film reduces the probability of spin depolarization of the noble gas during collisions with the container surface because it shields possible paramagnetic impurities in the bare glass material.

Taking together γ_{SE} and γ_w and the fact that the ^{129}Xe polarization cannot exceed the Rb polarization, because one excited Rb atom can polarize only one ^{129}Xe nucleus due to the conservation of the total spin number, the ^{129}Xe polarization can be described mathematically as

$$\frac{d\,P_{Xe}}{dt} = \gamma_{SE}(P_{Rb} - P_{Xe}) - \gamma_w P_{Xe}. \tag{3.3}$$

Assuming that the system is in steady state and the rates γ_{SE} and γ_w and the Rb density are constant in time equation 3.3 can be solved by

$$P_{Xe} = \frac{\gamma_{SE}}{\gamma_{SE} + \gamma_w} P_{Rb}. \tag{3.4}$$

3.1.2 Sensitivity boost II: Hyper-CEST

Overcoming the low sensitivity remains the everlasting challenge in NMR. On top of the Xe hyperpolarization trough spin exchange optical pumping (see section 3.1.1) the

[2] 1 barn= 10^{-28} m^2

temporary and reversible encapsulation of Xe atoms in molecular hosts can yield a further boost in sensitivity by a factor of ca. 10^3 and is termed Hyper-CEST (chemical exchange saturation transfer of hyperpolarized nuclei) [70]. The term Hyper-CEST origins from the temporary trapping of dissolved hyperpolarized Xe atoms into a molecular host molecule which changes the Xe NMR resonance significantly. This change in resonance frequency is much more pronounced than the resonance frequency change that occurs upon proton chemical exchange processes, as for example of labile protons from a protein backbone that exchange with protons from water molecules [71]. When the polarization of such an exchanging spin ensemble is saturated by applying a selective rf pulse, the loss of polarization is transferred between the exchanging spin ensembles. This combination of chemical exchange and saturation transfer is termed CEST [72, 73]. Taking advantage of CEST in combination with hyperpolarized nuclei makes the exchange-driven signal amplification even more efficient.

Principle of Hyper-CEST

The amplification through Hyper-CEST requires at least two spin ensembles that can exchange Xe atoms and that resonate at different NMR frequencies, as illustrated in Figure 3.2. Generally these are one abundant spin ensemble, usually dissolved Xe, and one dilute spin ensemble to which the Xe atoms belong to for just a few milliseconds. Since the noble gas usually does not participate in bond formation, the second spin ensemble of different chemical shift are the Xe atoms that are temporarily encapsulated in molecular host systems. A selective rf saturation pulse that specifically depolarizes the small spin ensemble lasts for much longer, usually a few seconds, and thus allows to label a large number of spins that exceeds the number of molecular hosts by far. The number of spins that can be labeled by the saturation pulse depends on the concentration of the molecular hosts and the in and out exchange rates (k_{in} and k_{out}) of Xe. A high exchange rate k_{out} is desirable for Hyper-CEST as it allows labeling a large number of spins that transfer the depolarization out of the molecular hosts. However, k_{out} cannot be too high. The average time a Xe atom is encapsulated in a molecular host can be approximated by k_{out}^{-1}. After that time, the spin will exchange and belong to the other, abundant spin ensemble which is separated by a chemical shift difference $\Delta\delta$. If k_{out}^{-1} is much faster than $\Delta\delta^{-1}$ only a single resonance in the NMR spectrum is observed and thus Hyper-CEST is not applicable. The chemical shift difference $\Delta\delta$ of useful molecular hosts for Xe atoms can easily exceed 100 ppm (see Table 2.2). This corresponds to a resonance frequency difference of $\Delta\delta = 100\ \text{ppm} \times 11.777\ \text{MHz/T} \times 9.4\ \text{T} \approx 11\ \text{kHz}$ at 9.4 T. Thus, the large chemical shift difference at this magnetic field strength makes Hyper-CEST applicable to molecules that host Xe atoms for times as low as 0.1 ms, which corresponds to $k_{\text{out}} = 10$ kHz. The boost in sensitivity obtained through Hyper-CEST allows to detect molecular hosts down to femtomolar concentrations in NMR spectroscopy [74, 75] and at nanomolar concentrations in MRI applications [17, 76].

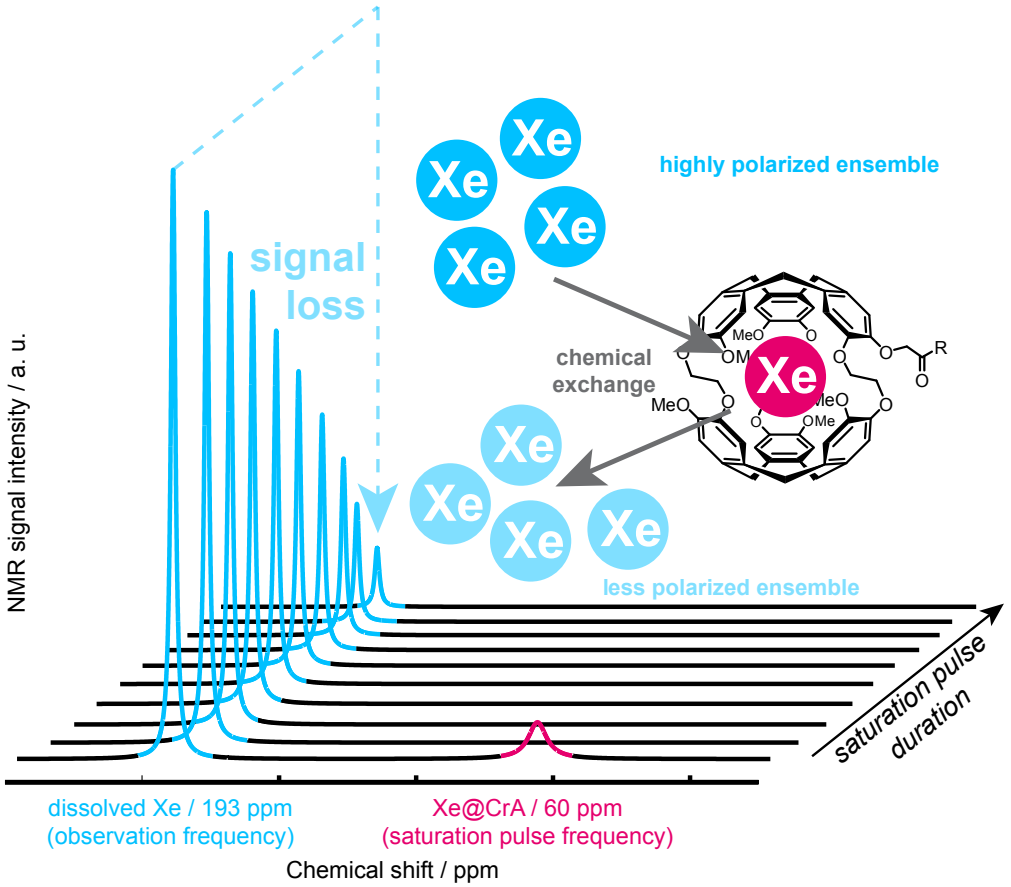

Figure 3.2 – Schematic of the Hyper-CEST principle. A saturation pulse applied to the Xe@CrA resonance at 60 ppm depolarizes the ensemble of ^{129}Xe atoms that are temporarily (ca. 30 ms) encapsulated in the molecular hosts during the saturation pulse (order of seconds). The chemical exchange of ^{129}Xe atoms into the surrounding aqueous solution transfers this loss of magnetization and the reduced net magnetization causes a signal depletion of the dissolved Xe resonance. Remaining polarized ^{129}Xe atoms can then be encapsulated in CrA and get affected by the saturation pulse subsequently. The overall remaining longitudinal net magnetization M_z that is normalized to the initial magnetization M_{z0} before applying the saturation pulse yields the Hyper-CEST effect.

Figure 3.3 shows the different parts of a Hyper-CEST experiment and their approximate duration that are required to detect the molecular hosts. A Hyper-CEST experiment basically consists of three parts. First, the freshly hyperpolarized Xe gas is dissolved in solution by bubbling the gas into solution. This is followed by a short wait time required to allow possible remaining bubbles to collapse. Immediately afterwards, the selective saturation pulse is applied. For in vitro experiments this is usually a continuous wave pulse as it provides the most efficient labeling. But also different shaped pulses have been tested [77] that depose less energy into the object of

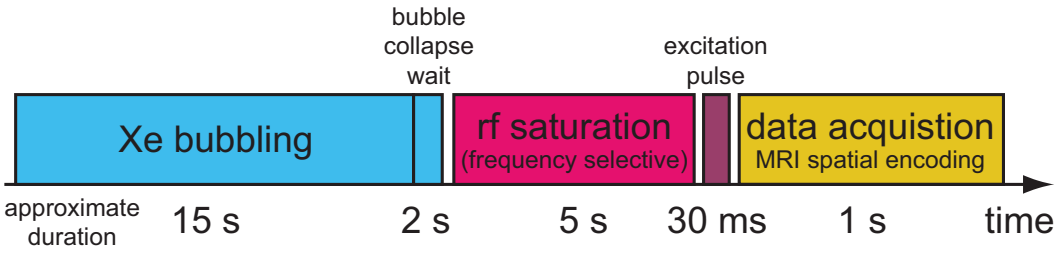

Figure 3.3 – Hyper-CEST sequence with approximate durations of the different parts (note: the length of the bars does not represent their actual duration). The duration of the Xe bubbling can be up to 20 s as for example in cell experiments. The bubble collapse wait time might have to be prolonged if for example no anti-foaming agent is used. The cw saturation pulse can be short (ca. 1 s) for fast exchanging Xe host structures, e.g. cucurbiturils, and might have to be longer if the Hyper-CEST effect has to be increased. The excitation pulse is usually a 90°-pulse to flip the complete z-magnetization into the transversal xy-plane. The duration of the data acquisition depends on the read-out method. For example an echo planar imaging read out takes ca. 1 s.

interest as they will become important for possible future in vivo applications. Finally, an excitation pulse is used to read out the remaining longitudinal magnetization. This can be either the recording of a normal free induction decay (FID) or in imaging applications the MRI pulse sequence.

As the saturation pulse is applied specifically with a certain resonance frequency and bandwidth, the described Hyper-CEST experiment for collecting an entire spectrum has to start over again with redelivery of hyperpolarized Xe into solution. After the bubbling the frequency of the saturation pulse is changed and a spectral range can be covered subsequently to obtain a whole spectrum. Such a spectrum is termed CEST- or z-spectrum, as the remaining magnetization along the z-axis is detected. Figure 3.4 shows such a simulated CEST-spectrum. When the saturation pulse frequency hits the resonance frequency of the abundant Xe in solution ensemble, the whole z-magnetization is destroyed almost instantaneously which results into complete saturation of M_z. Plotted is usually M_z normalized to the initial magnetization M_{z0}. When the saturation pulse hits the resonance frequency of a spin ensemble that interacts with a molecular host, which induces a distinct chemical shift, as for example Xe@CrA, the depletion of M_z/M_{z0} depends mainly on the concentration of the molecular host and the exchange dynamics [78, 79].

The shape of a resonance at the chemical shift δ_{res} in a Hyper-CEST spectrum can be modeled by an exponential Lorentzian function of the form [78]

$$f(\delta) = \exp\left[-\frac{2A}{\pi}\frac{w^2}{4(\delta_{\mathrm{res}}-\delta)^2+w^2}\right], \tag{3.5}$$

in which δ is the chemical shift that corresponds to the frequency of the saturation pulse, w is related to the width of the resonance in the CEST-spectrum and the depletion of the dip determined via parameter A.

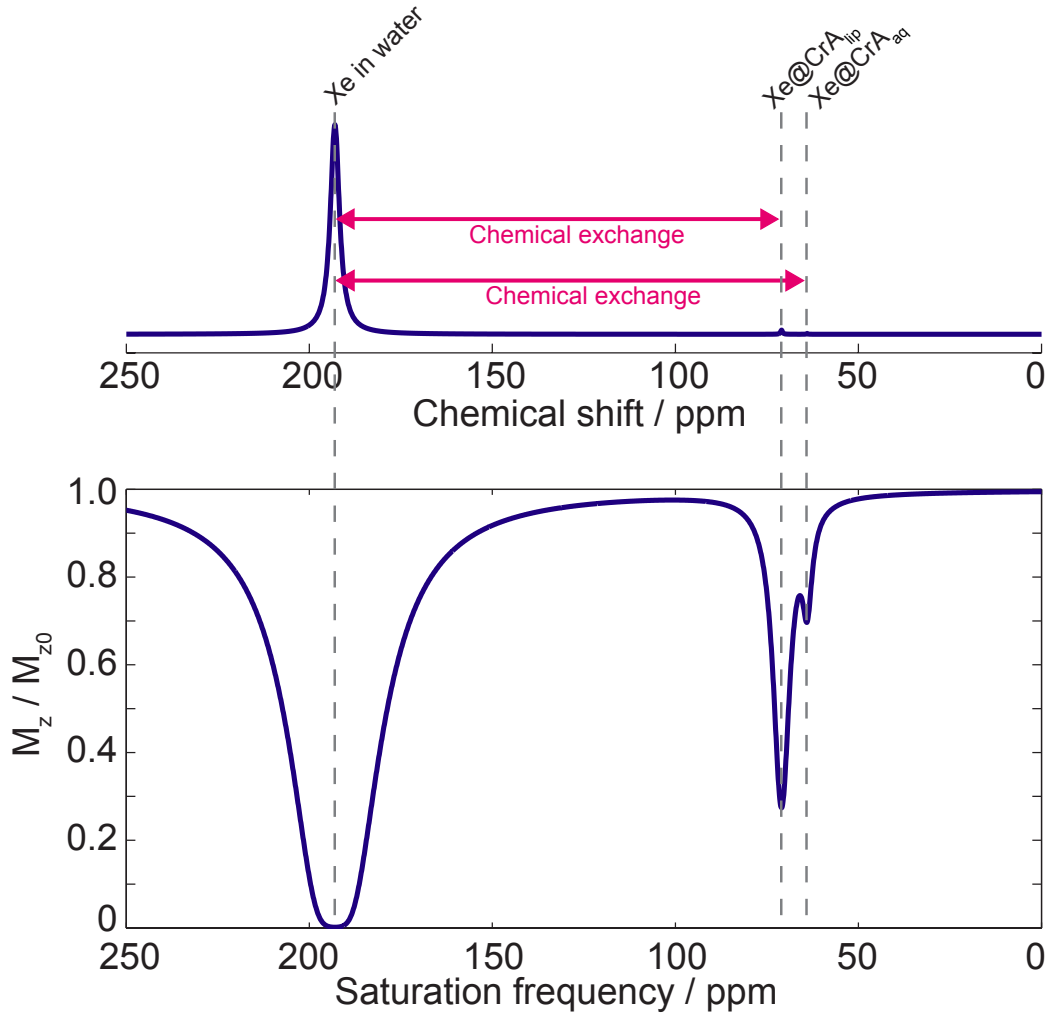

Figure 3.4 – Principle of a Hyper-CEST spectrum. The saturation pulse is swept over a frequency range and the remaining z-magnetization M_z of the signal of dissolved Xe atoms is detected subsequently and normalized to its initial signal intensity M_{z0}. The Xe exchange allows detecting spin ensembles that are masked by the noise in a conventional NMR spectrum.

Depolarization Laplace Transform Analysis

On-resonant saturation at δ_{res} with increasing saturation times t_{sat} yields a mono-exponential depolarization process [78]

$$f(\tau, t_{\text{sat}}) = e^{-t_{\text{sat}}/\tau(k_{\text{out}}, T_2, \phi)}, \tag{3.6}$$

where τ is the depolarization time. This parameter depends on the exchange rate k_{out}, the relaxation time T_2 of Xe@host and the local concentration ratio $\phi = [\text{Xe@host}]/[\text{Xe}$

in solution]. Such a mono-exponential process has also been observed experimentally when Xe was interacting with CrA as a molecular host [75].

Because of the fast Xe exchange Hyper-CEST resonances are often broad (up to several ppm) and thus multiple resonances can overlap when they resonate at the same or a similar frequency. In particular Hyper-CEST responses from different biomembranes are broad which hampers their separate detection. In such cases where Hyper-CEST resonances overlap, equation 3.6 becomes the superposition of multiple depolarization processes, each with a depolarization time τ that is weighted with its probability $F(s)ds$, such that

$$f(t_{\mathrm{sat}}) = \int_0^\infty F(s) e^{-s \cdot t_{\mathrm{sat}}} ds, \tag{3.7}$$

where $s = 1/\tau$, $F(s) \geq 0$ and $\int_0^\infty F(s)ds = 1$. Equation 3.7 is the Laplace transform (LT) of $F(s)$, called $\mathcal{L}\{F(s)\}$. Analyzing exponential decays by finding the inverse Laplace transform $\mathcal{L}^{-1}\{f(t_{\mathrm{sat}})\}$ is a common tool in different fields [80–84].

Here, the inverse LT $\mathcal{L}^{-1}\{f(t_{\mathrm{sat}})\}$ yields the corresponding depolarization time distribution. Hence, an inverse LT serves as the key element for depolarization LT analysis, DeLTA. In theory this is done by solving the Bromwich-Integral

$$F(s) = \mathfrak{L}^{-1}\{f(t_{\mathrm{sat}})\} = \frac{1}{2\pi i} \lim_{\gamma \to \infty} \int_{c-i\gamma}^{c+i\gamma} f(t_{\mathrm{sat}}) \cdot e^{s \cdot t_{\mathrm{sat}}} dt_{\mathrm{sat}} \tag{3.8}$$

by contour integrating over the complex plane of t_{sat}. To numerically solve the Bromwich-Integral, it has to be discretized and some noise $\epsilon_{\nu,t_{\mathrm{sat}}}$ has to be added:

$$f(t_{\mathrm{sat}}) = \frac{\sum_{\nu=1}^{n} F(s_\nu) \cdot e^{-s_\nu \cdot t_{\mathrm{sat}}} + \epsilon_{\nu,t_{\mathrm{sat}}}}{\sum_{\nu=1}^{n} F(s_\nu)}, \tag{3.9}$$

where n is the number of molecular environments, $F(s_\nu)$ is the probability density of the signal of environment ν and τ_ν is the corresponding depolarization time. Figure 3.5 illustrates the action of DeLTA on a simulated exponential decay of the form

$$f(t_{\mathrm{sat}}) = e^{-t_{\mathrm{sat}}/2\mathrm{s}} + \epsilon, \tag{3.10}$$

where 10 % Gaussian noise (ϵ) of the maximum value (= 1) was added.

It is known, that the analysis of a multi-exponential decay via the inverse LT approach is highly ill-conditioned [85]. Therefore, one requires an extra condition to ensure a unique solution. In this thesis a modified version of the MATLAB routine *rilt.m* [86], which is based on CONTIN [87], uses the Tikhonov regularization [88] as an extra condition to numerically obtain $\mathcal{L}^{-1}\{f(t_{\mathrm{sat}})\}$. The Tikhonov regularization ensures that $F(s)$ is as smooth as possible in s. In *rilt.m* this is done by minimizing

$$V(\alpha) = \sum_{i=1}^{m} \sum_{j=1}^{n} (f(t_i) - e^{-t_i \cdot s_j} \cdot F(s_j))^2 + \alpha^2 \cdot \sum_{j=1}^{n} (2 \cdot F(s_j) - F(s_{j+1}) - F(s_{j-1}))^2. \tag{3.11}$$

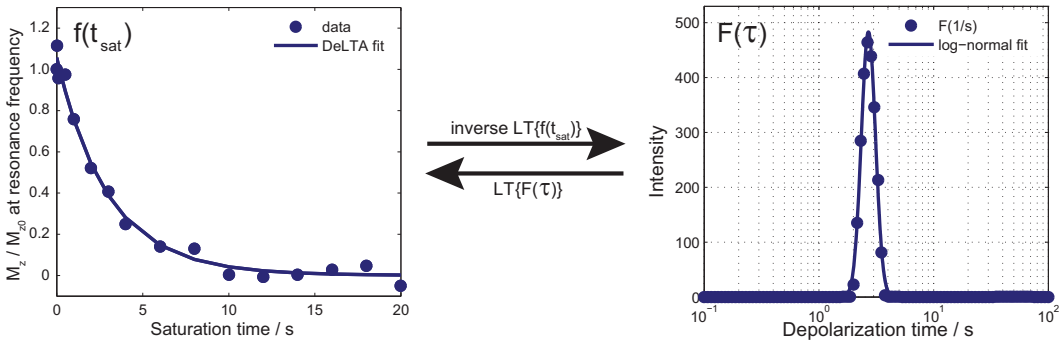

Figure 3.5 – Principle of DeLTA. The numerically determined inverse Laplace transform of the simulated data yields the depolarization time distribution.

The first term includes the difference of the m experimental data points $f(t_i)$ and the (discrete) LT of the guessed $F(s_j)$. This term equals a conventional fit residual χ^2. A least squared minimization of the second term, which represents the curvature of $F(s)$, is performed, weighted with the smoothing parameter α^2. For large alpha values, the depolarization time distribution $F(s)$ will be smooth and one might miss small peaks. For $\alpha = 0$, $F(s)$ will be totally free and not at all continuously differentiable. Therefore the data has to have as less noise as possible to be able to choose α as small as possible. For the analyses in this thesis α was set between 0.05 and 0.1. The minimum of $V(\alpha)$ is obtained when $F(s)$ has the least degree of curvature and its LT represents the experimental data well, i. e. χ^2 is minimized as well. The code of the modified MATLAB routine *rilt.m* can be found in the appendix (section B).

The figures 3.6 and 3.7 demonstrate the robustness of the MATLAB routine DeLTA. In Figure 3.6 a tri-exponential decay

$$f(t_{\mathrm{sat}}) = \sum_{j=1}^{3} e^{-t_{\mathrm{sat}}/\tau_j} + \epsilon \tag{3.12}$$

consisting of 16 data points, similarly distributed as in the experiments, was simulated. The tri-exponential decay contained three depolarization times ($\tau_j = 0.1$, 1 and 10 s with $j = 1, 2$ and 3) with the same amplitude. To check the influence of noise on the outcome of DeLTA different levels of Gaussian noise ϵ (0, 1, 3, 6 and 10 %) were included in the simulations. DeLTA yielded the correct logarithmically spaced depolarization time distribution and amplitudes up to a noise level of 3 %. At a noise level of 6 % the fastest depolarization time of 0.1 s was not found correctly by DeLTA. Also the amplitudes were off. At a noise level of 10 % all three depolarization times that were fitted by DeLTA were off. A similar result was obtained when simulating a mono-exponential decay and analyzing it with a linearly spaced depolarization time distribution with DeLTA (Figure 3.7). Also in that case, only noise levels larger than 6 % produced incorrect results for the simulated depolarization process with $\tau = 10$ s. The hyperpolarizer setup that was used for the experiments produces a polarization

with a shot-to-shot noise of ca. 1 %. Thus, DeLTA should be applicable for the analysis of the recorded depolarization processes.

In summary, DeLTA can determine the contributing τ's and the number n of different molecular environments without any prior knowledge. Yet, one important requirement for the detection of caged Xe in different molecular environments with similar chemical shifts is a difference in k, T_2 or ϕ. This difference has to be large enough to yield medium differences in τ. Too pronounced differences in τ might make slow depolarization invisible when a process with much shorter τ happens at the same time in the same micro-environment. The same holds for depolarization processes with a small probability, for example due to a small Xe ensemble in a certain molecular environment. Those depolarization processes might be masked be much larger spin ensembles.

Molecular xenon hosts

The molecular host that can encapsulate Xe atoms has two functions. First it produces a chemical shift that separates the encapsulated Xe ensemble from the dissolved Xe ensemble and second it can functionalize the inert noble gas atoms through chemical modifications of the molecular hosts. The molecular hosts are either macro-molecules that can host a single Xe atom at a time, such as cryptophanes or cucurbiturils, or larger structures that can host more than one Xe atom at a time, such as perfluorooctylbromide (PFOB) nanoparticles [30, 49] or gas vesicles [18]. In this thesis only molecules that can host one Xe atom at a time were used and are introduced in the following.

Cryptophane-A: The most prominent molecule that can host a single Xe atom is cryptophane-A-monoacid (CrA[3]). Its chemical structure is shown in Figure 3.8. CrA represents one type of cryptophanes that were originally developed in 1981 with the purpose to temporarily encapsulate small uncharged guest molecules to facilitate subsequent chemical reactions [89]. The first use of Xe as a guest in cryptophanes, in particular in CrA, was demonstrated in 1998 [90].

The common structure of all cryptophanes consists of two cyclotriveratrylene "caps", each containing three aromatic rings connected by methylene bridges, and a series of linkers holding these two caps together. CrA is characterized by three methoxy groups on one cyclotriveratrylene cap and two methoxy and one acid group on the other cyclotriveratrylene cap. The two caps are connected via three ethyl linkers. The three ethyl linkers give CrA an internal cavity volume of 88 Å^3 [91] which provides enough space to fit one Xe atom in, that has an average van der Waals volume of ca. 42 Å^3. With the fact that the strongest host-guest interaction happens, when the guest occupies ca. 55 % of the host volume [92], CrA suites very well as a

[3]Cryptophane-A-monoacid is usually denoted as CrA_{ma}; for reasons of simplicity and as only CrA_{ma} and not cryptophane-A-diacid was used in this thesis I will use the abbreviation CrA throughout this thesis.

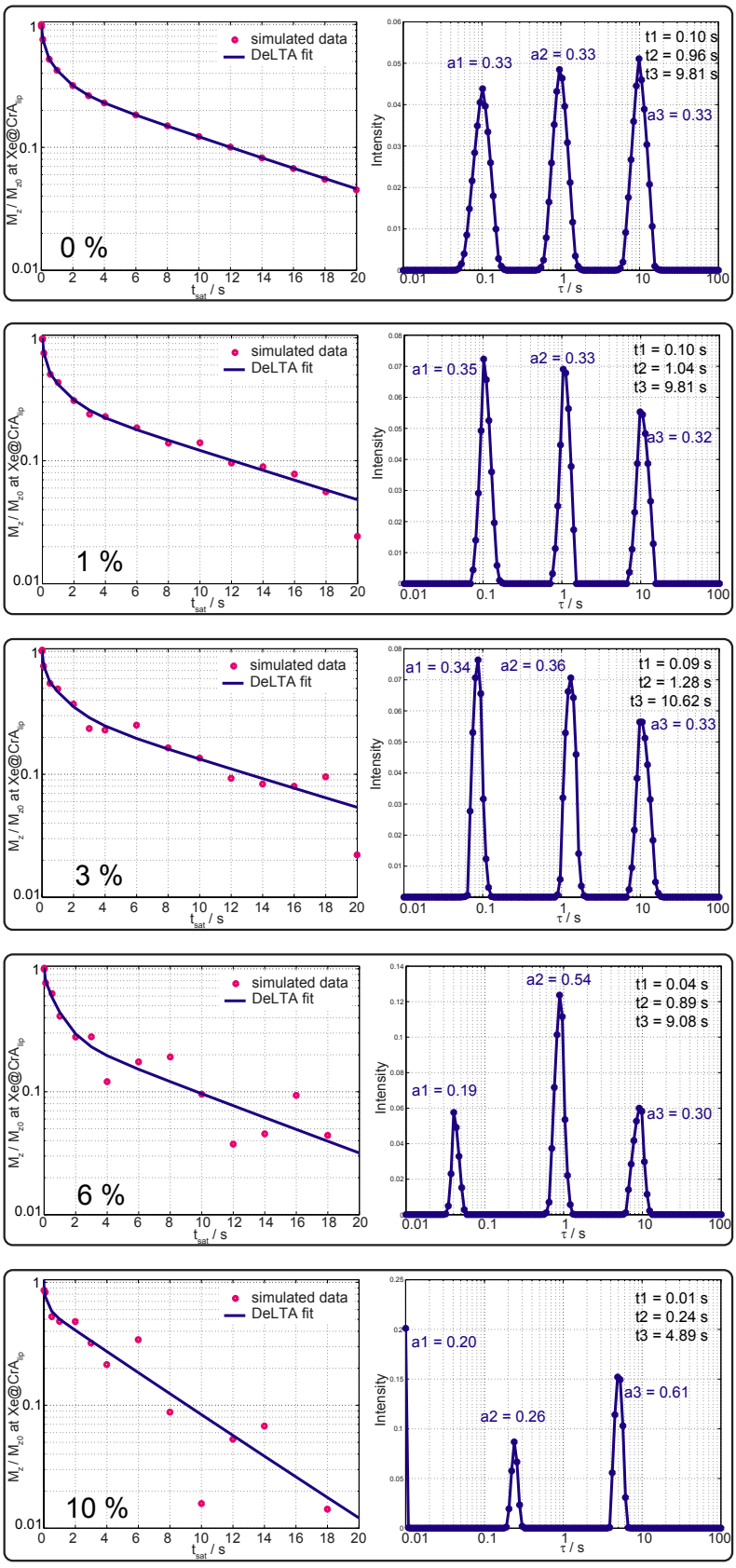

Figure 3.6 – DeLTA of a simulated tri-exponential depolarization process (equation 3.12) with the depolarization times $\tau_j = 0.1$, 1 and 10 s with $j = 1, 2$ and 3 with noise levels of $\epsilon = 0$, 1, 3, 6 and 10 %. The obtained depolarization times and the corresponding amplitudes are denoted in the different plots.

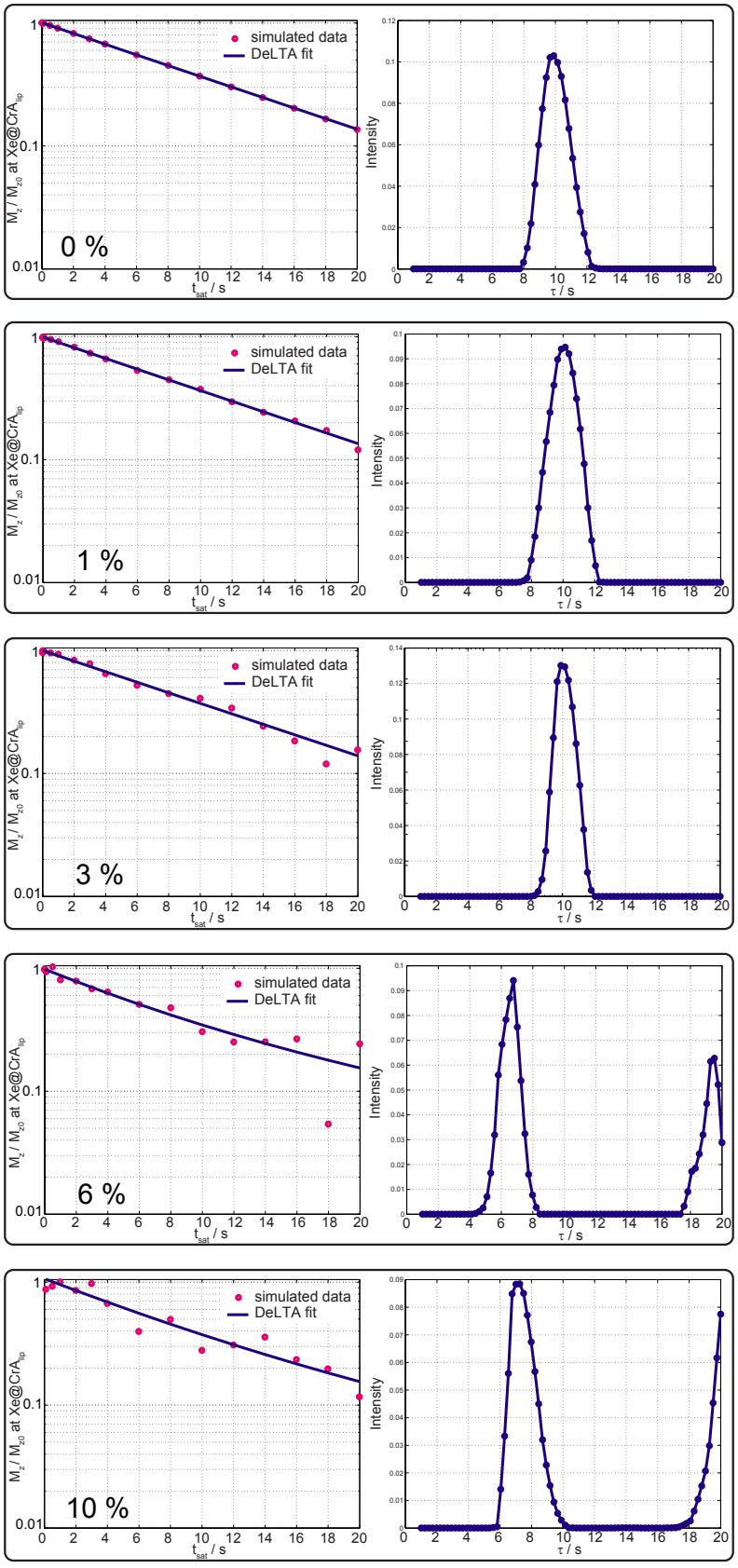

Figure 3.7 – DeLTA of a simulated mono-exponential depolarization process with the depolarization time $\tau_j = 10$ s with a linearly spaced depolarization time distribution with noise levels of $\epsilon = 0$, 1, 3, 6 and 10 %.

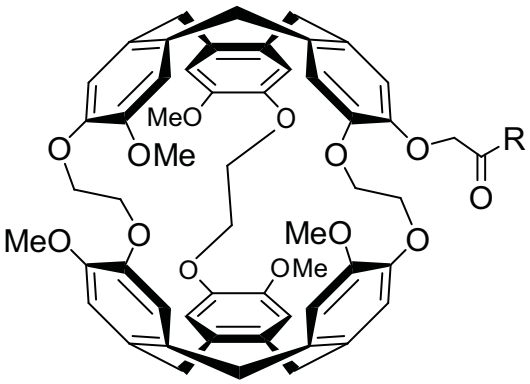

Figure 3.8 – Chemical structure of the monoacid version of cryptophane-A (CrA). The acid group can be used for chemical coupling reactions with other molecules, e.g. targeting cell moieties, denoted by R.

Xe host. When the distance in between the two cyclotriveratrylene caps is changed, the chemical shift of Xe@host can change up to 40 ppm [93].

Measurements of the resident time of Xe in CrA revealed that Xe stays between 30 and 300 ms in CrA in water, dependent on the temperature and salt concentrations [94, 95]. The Xe exchange rate can change drastically when CrA is in a different molecular environment. For example 100 µM CrA dissolved in DMSO provide a Xe residence time of ca. 3 ms at 295 K [79] and it is assumed that it gets shorter the more lipophilic the environment is.

The groups that are attached to the cyclotriveratrylene caps and the linkers can be also changed in different ways allowing great possibilities for chemical modifications, for example to obtain cryptophanes with increased water solubility compared to CrA's poor solubility of only a few micromolar [74, 94, 96, 97].

Yet, not only the cryptophane molecule itself can be modified, also other molecular structures can be attached to the host molecule. For example, for better or even specific cell detection receptor-binding transferrin can be coupled to the CrA molecule [98], an antibody can be linked via a biotin-avidin bridge that is coupled to CrA [17] or several CrA can be attached to a M13 bacteriophage [48] or a bacteriophage against an epidermal growth factor receptor [19].

Cucurbiturils: Cucurbiturils (CBs) are macrocyclic molecules made of glycoluril monomers linked by methylene bridges. The oxygen atoms of the glycolurils are located along the edges of the linked molecules and are tilted inwards, forming a partly enclosed cavity. CBs got their name due to their structure with a shape similar to that of a pumpkin of the family Cucurbitaceae.

CBs were first discovered in 1981 [99]. The first type was CB6, a CB that is composed of 6 glycoluril monomers. Until today CBs composed of 5, 6, 7, 8, and 10 glycoluril monomers can be produced synthetically and are stable [100]. They have a

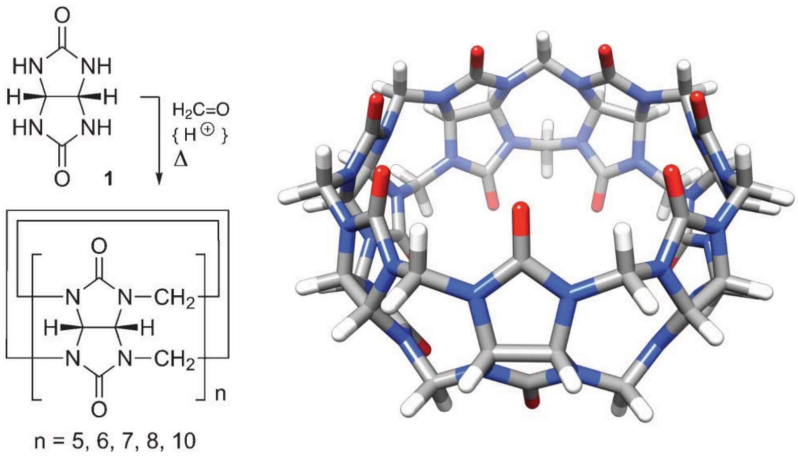

Figure 3.9 – Chemical structures of a glycoluril monomer and CBs. A CB structure is obtained when glycoluril monomers are coupled together via methylene bridges in the presence of formaldehyde under acidic conditions. As an example the 3D structure of CB7 is shown as well. Reproduced from reference [101]. Copyright © 2012 The Royal Society of Chemistry.

common depth of 9.1 Å and provide an internal cavity size of 82, 164, 279, 479, and 870 $Å^3$, respectively. The structure of a glycoluril monomer that is conjugated via the methylene bridges to form a CB and an example 3D model of CB7 are shown in Figure 3.9.

The solubility in water of CB5 and CB7 is with 20 – 30 mM much higher than the solubility of CrA. Interestingly, changing the number of glycoluril monomers can change the water solubility drastically. The water solubility of CB6 and CB8 is only 18 µM and less than 10 µM, respectively. However, chemical modifications of CB6 improved its water solubility to 0.2 M [102, 103]. The water solubility for CB10 is not determined so far [100].

The small cavity size of CB5 provides a strong binding constant for Xe atoms (1300 M^{-1} [104]) in contrast to the larger CBs (200 M^{-1} for CB6 [103]) that must have quite fast Xe exchange rates on the NMR timescale due to their cavity size. Due to the fast Xe exchange the Xe resonance in a conventional NMR spectrum is broadened which makes the direct detection of Xe@CBx with $x > 5$ difficult.

Not only Xe, also other atoms and small molecules can be encapsulated temporarily in the CB derivatives. For example small fluorescent molecules or small molecules that are produced when for example the enzyme lysine decarboxylase (LDC) processes the amino acid lysine, show binding affinity for CB6 or CB7 [105–108]. The use of dyes that change their fluorescence behavior upon binding to CB can therefore be used to study enzyme activity in case the product shows a higher binding affinity to CB than the fluorescent dye.

3.2 Magnetic resonance imaging

Information about the spatial distribution of MR detectable nuclei can be obtained via Magnetic Resonance Imaging (MRI). First MRI data was acquired in the 1970's by Paul C. Lauterbur [41] and Sir Peter Mansfield [42]. Since then a lot of MR imaging techniques have been developed.

3.2.1 MR image encoding

The principle of MRI relies on magnetic field gradients $\vec{G}$ that are applied along the three spatial dimensions x, y and z. The applied magnetic field gradients $\vec{G}$ change the resonance frequency of the nuclei to

$$\omega(\vec{x}) = \gamma(B_0 + \vec{G} \cdot \vec{x}). \tag{3.13}$$

The frequencies from different spatial origins are encoded in the (three dimensional) frequency space, known as "k-space". The spatial origins can be obtained by Fourier transformations of the recorded signals in k-space via slice encoding along the z-axis and frequency and phase encoding in the xy-plane. The different encodings have to be applied before and during data acquisition as described in the following.

Slice selection

A slice of a three-dimensional object can be selected by adding a gradient along the z-axis[4] G_z to the static magnetic field B_0, which changes the precession frequency to

$$\omega(z) = \gamma(B_0 + G_z\, z). \tag{3.14}$$

Technically, the selected slice cannot be infinitesimal narrow as it depends on the bandwidth $\Delta\omega$ of the applied rf pulse and the gradient G_z. For small flip angles its width can be approximated by

$$\Delta z = \frac{\Delta\omega}{\gamma G_z} = \frac{2\pi}{\gamma G_z \tau_z}, \tag{3.15}$$

where τ_z is the duration of the rf pulse. For larger flip angles usually iterative methods have to be used to determine the slice profile and its width [109]. A confined interval Δz with relative sharp edges can be obtained by modulating the rf-pulse with a *sinc*-envelope

$$B_1^{sinc}(t) = B_1(t) \cdot \frac{\sin(\Delta\omega(t - \tau_z/2))}{\Delta\omega(t - \tau_z/2)}, \tag{3.16}$$

as its Fourier transform is a block function. In reality such block functions have wiggles at the edges, as the rf pulse has a finite length which causes dephasing between the precessing spin packages. Such dephasing can be reversed by applying a refocusing gradient along the z-axis of the duration $\tau_z/2$ (see also Figure 3.10).

[4] w.l.o.g. we have chosen the z-direction

Phase encoding

The signal S after applying slice encoding origins from the magnetization that precesses in the two dimensional xy-plane

$$S \propto \int\int M_{\perp}(x,y)\, dx\, dy. \tag{3.17}$$

Adding a gradient G_x with the duration τ_x before data acquisition allows phase encoding along the x-axis. Phase encoding causes the spin packages to precess with the same ω_0 but with different phase angles $\varphi(x) = \gamma G_x \tau_x x = k_x x$, with $k_x = \gamma G_x \tau_x$, which yields

$$S(k_x) \propto \int\int |M_{\perp}(x,y)|\, e^{ik_x x}\, dx\, dy. \tag{3.18}$$

Inverse Fourier transformation of equation 3.18 yields a projection of the three dimensional object onto the x-axis. Hence, to obtain a fully reconstructed three dimensional MR image a further encoding along the y-axis is required.

Frequency encoding

In contrast to phase encoding, where the gradient was switched on *before* data acquisition, for frequency encoding a gradient G_y is added *during* data acquisition. This causes the spin packages to precess with different frequencies $\omega(y) = \gamma(B_0 + G_y y)$ and together with the phase encoding the signal from the selected slice along the z-axis is given by

$$S(k_x,k_y) \propto \int\int |M_{\perp}(x,y)|\, e^{i(k_x x + k_y y)}\, dx\, dy. \tag{3.19}$$

Thus, an inverse two dimensional Fourier transformation of equation 3.19 into the spatial domain provides the spatial distribution of the magnetization $M_{\perp}(x,y)$:

$$M_{\perp}(x,y) \propto \frac{1}{2\pi} \int\int S(k_x,k_y) e^{-i(k_x x + k_y y)}\, dk_x\, dk_y \tag{3.20}$$

To detect the signal in equation 3.20, the frequency encoded signal along the y-direction has to be discretized into N_y points, with respecting the Nyquist theorem, which yields N_y data points along one line in k-space. Repeating the frequency encoding M_x times, each time with a changed phase encoding gradient G_x, yields $M_x \times N_y$ data points in k-space. Discrete Fourier transformation over n and m, where $-\frac{N_y}{2} < n < \frac{N_y}{2} - 1$ and $-\frac{M_x}{2} < m < \frac{M_x}{2}$

$$M_{\perp}(x_m,y_n) \propto \frac{1}{2\pi} \sum_m \sum_n S(k_{x_m},k_{y_n}) e^{-i(m\Delta k_x x_m + n\Delta k_y y_n)} \tag{3.21}$$

yields the real space MR image matrix, where x_m and y_n are the discrete points in real space.

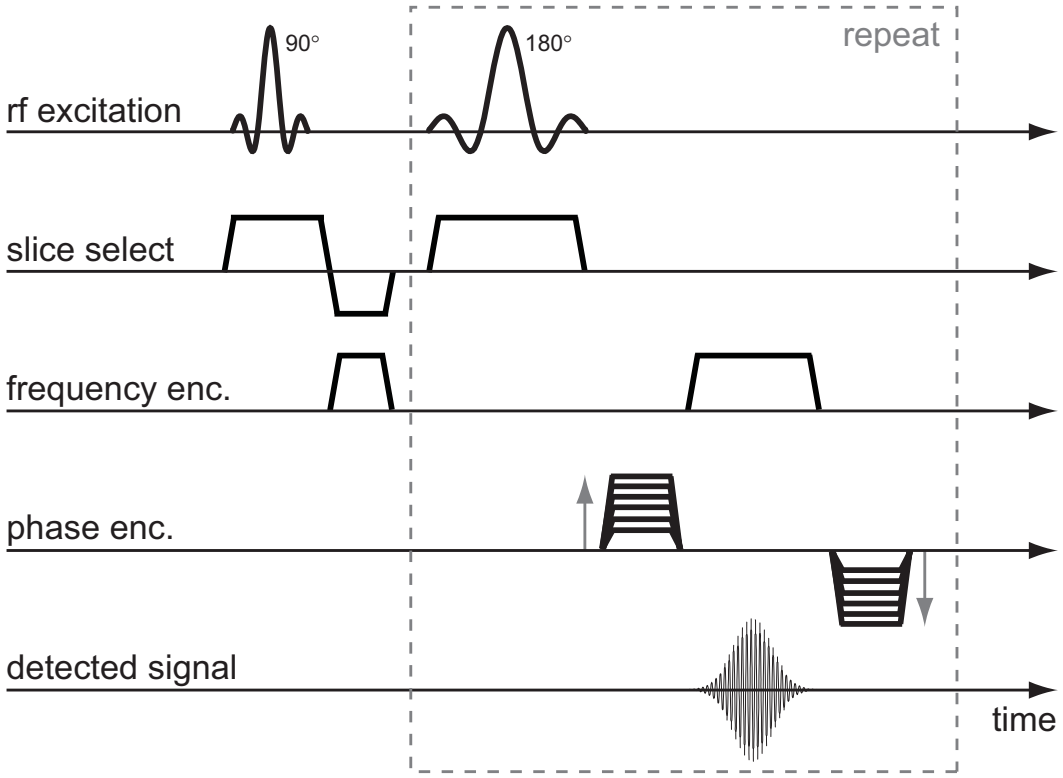

Figure 3.10 – RARE pulse sequence. After the 90° excitation pulse several 180° pulses followed by the frequency encoding and phase encoding (changed after every repetition) gradients are repeated to yield a full MR image.

3.2.2 RARE fast spin echo pulse sequence

The above described basic principle of three dimensional MR image acquisition requires a lot of time, as for each line in k-space the magnetization has to be excited. Modified pulse sequences can be used to record the data of an MR image much faster, e.g. by sharing the excited magnetization between different lines in k-space.

An imaging sequence consists basically of the excitation of the nuclear spins, the application of the spatial encoding gradients and the data acquisition of a spin echo. In this thesis a RARE (rapid acquisition with relaxation enhancement) fast spin echo sequence [110, 111] was used for MRI experiments as it favors long T_1 relaxation times as it is the case for ^{129}Xe nuclei. The pulse sequence is shown in Figure 3.10 and its components are explained briefly in the following.

After an initial slice-selective 90° excitation pulse the sequence uses a repetition of 180° pulses to evoke a train of multiple individually phase encoded echoes. The slice-selective gradient that lasts during the 90° excitation pulse gets inverted after the end of the excitation pulse for spin rephasing. This is followed by a short dephasing frequency encoding gradient pulse is applied to reach the edge of k-space. Next, a

180° pulse is irradiated accompanied by a slice-selective gradient. A phase encoding gradient pulse follows, after which the read-out frequency encoding gradient is applied and the sampling of the first spin echo occurs. The spin echo acquisition is immediately followed by a rephasing phase encoding gradient.

The last part of the sequence, starting with the 180° pulse, gets repeated several times whereas in each repetition the phase encoding gradient is changed to record another line in k-space.

The advantages of all fast spin echo methods such as the RARE sequence are that with a single excitation pulse several echoes can be acquired to encode the entire k-space or a large fraction thereof. This provides a highly efficient method for obtaining strongly T_2-weighted images or for dynamic imaging where fast data acquisition is fundamental. The SNR of a RARE sequence is near that of standard spin echo imaging, yet it is much faster. Its SNR generally surpasses that of images acquired using gradient-recalled echo methods [112] such as the echo planar imaging (EPI) pulse sequence [113, 114]. Furthermore, the RARE pulse sequence is much more robust against magnetic field inhomogeneities than an EPI sequence. One whole MR image using the RARE sequence can be acquired with a single 90° excitation pulse if the T_2 relaxation time of the detected nuclei is long enough. With the RARE sequence several MR images of decent resolution can be obtained in a multi-slice acquisition in approximately less than a minute.

Disadvantages of the RARE sequence are first the presence of T_2-dependent effects along the phase encoding dimension of the k-space and an increased rf power deposition due to the multiple 180° pulses. The last issue can be overcome by a method developed in 1991 that takes advantage of pulses with a smaller flip angle than 180° [115].

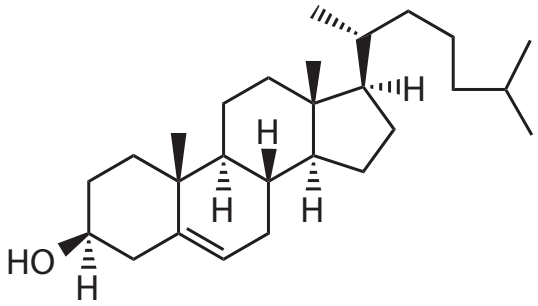

Figure 3.11 – Chemical structure of cholesterol.

3.3 The lipid environment

Xe hosts are usually hydrophobic and therefore tend to partition into biological membranes that are composed of lipids. NMR signatures of CrA molecules that interact with lipids were first reported in 2010 by Meldrum et al. [21]. Lipids constitute a broad group of naturally occurring molecules that include fats, waxes, sterols, fat-soluble vitamins (such as vitamins A, D, E, and K), monoglycerides, diglycerides, triglycerides, phospholipids, and others. They are not classified together because of a structural similarity but because of their common physical property: they do not dissolve in water, but they do dissolve in organic solvents [116]. Lipids can act as important signaling molecules, or energy storage and they are the main building material for membranes and cellular organelles [5]. More than 600 lipid species can be found in most biological membranes [117]. The formation of such biological membranes is based on the hydrophobic or amphiphilic character of most of the lipids that allows them to form structures such as vesicles or lipid bilayers. Cellular membranes of different cell types can vary a lot in lipid composition. For example nerve cells need a high level of cholesterol (Figure 3.11) which provides a very rigid cellular membrane whereas others contain almost no cholesterol [5]. The highly dynamic lipid bilayer not only gives cells a structure, it also allows proteins that are involved in important cellular functions to anchor into it. Additionally the lipid bilayer acts as a barrier for molecules that should not cross passively the membrane. The inner and outer side of a cellular lipid bilayer usually contains a different mixture of components. For example, the brain gets protected from unwanted substances through the blood by brain endothelial cells. They possess a highly negative charged glycocalix on the outer side that is produced by a large amount of glycolipids to which negatively charged cell surface heparan sulfate proteoglycans are coupled [118, 119]. However, the main component of lipid membranes are phospholipids [5] which are introduced in the following. Their influence on membrane dynamics is discussed after that.

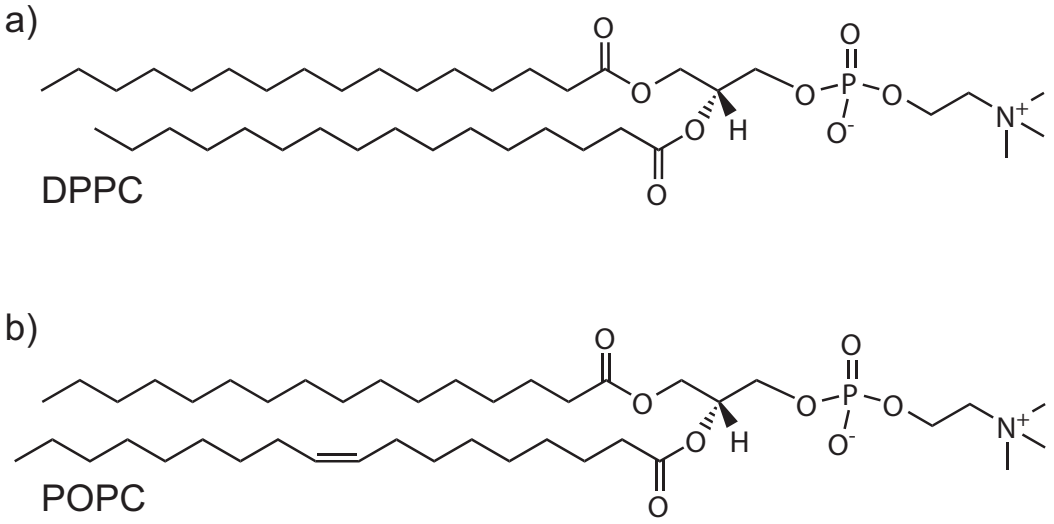

Figure 3.12 – Chemical structure of DPPC (a) and POPC (b). DPPC contains two fully saturated fatty acid chains, POPC has only one.

3.3.1 Phospholipids

In biological membranes, phospholipids have both a structural and a functional role. The structure is mainly determined by the amount of cholesterol and the four major classes of phospholipids, namely phosphatidylcholine (PC), phosphatidylethanolamine (PE), phosphatidylserine (PS) and sphingomyelin. The functional role of phospholipids is mainly given by the net charge of the head group and the backbone. The functional group consists of phosphatidylglycerol (PG), phosphatidylinositol (PI), phosphatic acid and several types of gangliosides. The classes of phospholipids are distinguished by (i) the head group, (ii) the backbone and (iii) the number of C-atoms and double bonds in the fatty acid chains.

The overall most dominant species in mammalian cells are PCs [5]. For example with 32.7 and 32.0 mole-% 1,2-dipalmitoyl-*sn*-glycero-3-phosphocholine (16:0 PC, DPPC) and 1-palmitoyl-2-oleoyl-*sn*-glycero-3-phosphocholine (16:0-18:1 PC, POPC) are the most abundant PCs in egg yolk [5]. Figure 3.12 shows their chemical structures. DPPC has two fully saturated fatty acid chains made up of 16 carbon atoms, named palmitoyl. POPC consists of one palmitoyl fatty acid chain next to one unsaturated oleoyl fatty acid chain that consists of 18 carbon atoms with one unsaturated bond. Both have the same glycerol backbone and phosphocholine headgroup. Because of their abundance in mammalian cells and their distinct properties, e.g. the different lipid phases (as discussed below), these two lipids together with cholesterol were mainly used as components for model membranes used in the experiments of this thesis.

3.3.2 Membrane fluidity and lipid phases

The membranes of cells have to be flexible enough to allow cell movement, cell division and reorganization of for example membrane proteins. On the other hand it has to be tight enough to function as a barrier and provide a base for proteins. The flexibility of the lipid bilayers is termed fluidity. As it is not a physical parameter in the classical sense fluidity cannot be quantified. It comprises the viscosity, lateral diffusion and rotational mobility of a lipid bilayer and the anchored components. Hence, the intra-lipid diffusion of molecules and atom that are embedded into a membrane, such as CrA and Xe, is strongly influenced by its fluidity. This influence, combined with the fact that membrane fluidity also affects the molecules' and atoms' permeation into a membrane, can be detected using ^{129}Xe Hyper-CEST, as demonstrated in chapter 4.

Basically three different phases of membrane fluidity are known [120, 121]. They are defined as the liquid-disordered (L_d) phase (sometimes in the literature also termed fluid phase or L_α phase), a solid-ordered (S_o) phase (sometimes termed crystalline, gel or L_β phase) and a liquid-ordered (L_o) phase.

L_d and S_o phase: The L_d phase is characterized by a disordered fluid state, in which the lipids are loosely packed and have a high lateral mobility. A membrane that contains only one type of phospholipids is in the L_d phase at a temperature above the phospholipid's characteristic transition temperature T_c. Phospholipids with unsaturated acyl chains usually have a low T_c compared to fully saturated phospholipids, e.g. $T_{c,\,\mathrm{POPC}} = 271$ K and $T_{c,\,\mathrm{DPPC}} = 314$ K [122]. Below T_c a biomembrane that consists of one type of phospholipids is in the S_o phase. In the S_o phase the phospholipids are tightly packed, ordered and have less lateral motion.

L_o phase: The L_o phase can exist in lipid bilayers when for example cholesterol is incorporated in a POPC bilayer [123]. The addition of cholesterol increases the ordering of the acyl chains [124] and reduces the passive permeability of lipid bilayers [125]. However, this ordered phase still possesses a high lateral mobility, as the L_d phase, and is therefore called the L_o phase [126, 127]. Although, different studies yielded slightly different results [120], which can be attributed to the different indirect methods used to establish the phase boundaries, basically at 310 K a cholesterol concentration of less than 15% produces a L_d phase (Figure 3.13). At cholesterol concentrations larger than ca. 45 % only the L_o phase is present.

3.3.3 Lipid rafts

In POPC bilayers that contain cholesterol at a concentration between 15 and 45 %, the L_d and L_o phases coexist at 310 K as shown in Figure 3.13. When both phases are present simultaneously lipid rafts of the L_o phase are formed [128, 129]. Lipid rafts are spatially separated in-plane fluid domains in cellular membranes and are thought to act as platforms for proteins that cause for example cell signaling.

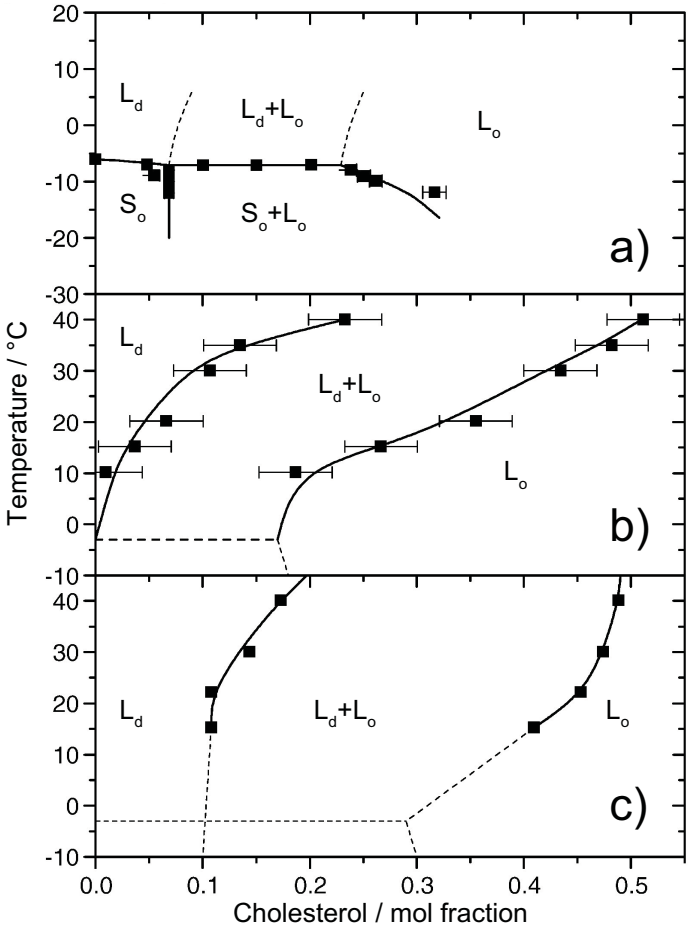

Figure 3.13 – Binary phase diagram for mixtures of POPC and cholesterol in water. a) POPC with a deuterated palmitoyl chain. Data points from reference [130]. Phase boundaries (symbols) determined from ^{2}H-NMR spectra, in the ordered phase only. b) Data points from reference [126] obtained with normal POPC. Phase boundaries (symbols; liquid phase only) deduced from distribution of fluorescence lifetimes of trans-parinaric acid. c) Data points from reference [131] obtained with normal POPC. Phase boundaries (symbols; liquid phase only) are determined from fluorescence polarization of diphenylhexatriene (DPH) and lifetime-weighted quantum yield of trans-parinaric acid. Reproduced from reference [120].

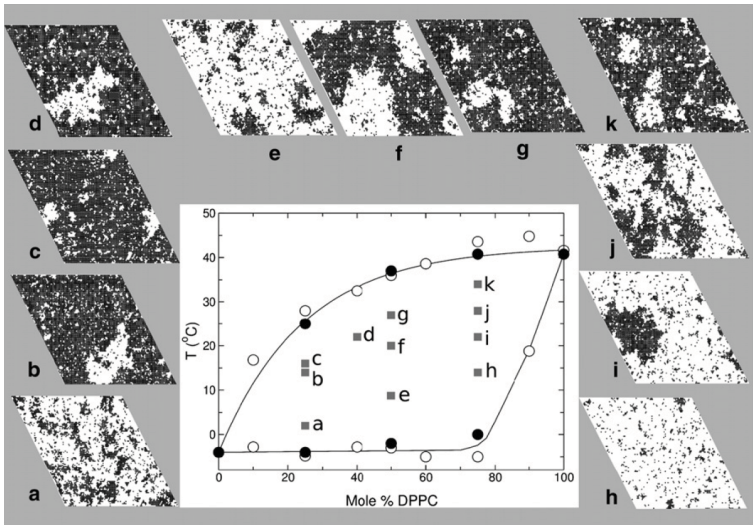

Figure 3.14 – Binary DPPC:POPC phase diagram obtained via differential scanning calorimetry measurements. Open circles are data points from reference [134] and solid circles are data points from [135]. In the inner part of the phase diagram, the L_d and S_o phase coexist. On the periphery corresponding snapshots from Monte Carlo simulations are shown (their positions in the phase diagram are indicated by the letters). White represents the S_o phase and black represents the L_d phase. Reproduced from reference [135]. Copyright © 2012 Elsevier Inc.

Along with the spatial separation of lipid rafts they are also different in lipid composition compared to the membrane from which they are derived. They generally contain up to 5-fold the amount of cholesterol than the surrounding bilayer [132]. The immiscibility of lipid rafts with the surrounding membrane is thought to minimize the free energy between the different phases [133]. A difference in membrane thickness of the lipid rafts and the surrounding membrane results in a hydrophobic mismatch at the boundary between the regions. This mismatch might increase the local surface tension which may lead to the formation of larger and more circular lipid rafts to minimize the surface tension and thus the free energy.

Lipid rafts are not only found in bilayers that contain cholesterol, they can also for example be present in binary DPPC:POPC mixtures. In that case the S_o phase, produced by DPPC, and the L_d phase, produced by POPC can coexist as a function of the concentration ratio and the temperature [127, 134]. Figure 3.14 shows a phase diagram of a binary DPPC:POPC mixture. The phase diagram was obtained via differential scanning calorimetry measurements and is supported by Monte Carlo simulations. The experiments revealed that at a high DPPC to POPC ratio, the lipid raft formation in DPPC:POPC mixtures can be accompanied with remarkable fluctuations in domain size [135]. For example Figure 3.14 j) shows a snapshot of a Monte Carlo simulation in which the solid domains, represented in white, are not compact and do not have a well defined size.

3.3.4 Model Biomembranes

The complexity of biological membranes makes their direct investigation difficult. Artificially prepared model biomembranes present a good alternative. They are much easier to examine yet are still excellent models of biomembranes [136], which lead to their extensive use. Such model biomembranes have the advantage that they are for example more robust, better manageable and can be consistently prepared.

In aqueous solutions phospholipids self-assemble and usually tend to form vesicles made up of lipid bilayers, if they possess two acyl chains. With only a single acyl chain it is most likely that they form micellar structures. The vesicles can have different sizes. The smallest possible vesicles (because of curvature tension) can easily be obtained by sonication of a solution that contains lipids. They have a diameter of 10 – 50 nm and are called small unilamellar vesicles (SUVs). Their high surface tension facilitates the fusion of several SUVs to larger vesicles to reduce the free energy, which complicates in particular their long term storage. The largest vesicles can be several micrometers in diameter and are called giant unilamellar vesicles (GUVs). They are large enough that optical microscopy methods can be used to study them. However, to obtain stable GUVs a special preparation method, which is described below, is required. In contrast to the SUVs, GUVs tend to break apart to form smaller (also multilamellar vesicles). The intermediate sized vesicles that are termed large unilamellar vesicles (LUVs) or liposomes have usually a size around 100 nm. Mainly because of their stability liposomes are the most used vesicles to mimic cellular membranes. Liposomes cannot only be used to model biomembranes, due to their stability they are also used as nanocarriers to deliver drugs to a site of interest [137]. The vesicle preparation and their physical characterization are described in the following.

Preparation of lipid vesicles

Independent of the final application and the desired properties of the lipid formulation the preparation of lipid vesicles involves basically three steps. The three elements are first the preparation of the lipids for hydration, second the hydration with agitation, and third the sizing to a homogeneous distribution of vesicles with either sonication or extrusion. The single steps to produce homogeneously sized liposomes are explained in in the following. This is followed by a brief description how to prepare of GUVs that were used for fluorescence microscopy studies.

Liposome preparation

1. Preparation of the lipids for hydration
   When preparing liposomes, the lipids must be first dissolved in organic solvents in the desired ratio to mix completely. Usually pure chloroform or a chloroform:methanol mixture (1:1, vol/vol) is used. The use of methanol ensures the dissolution of lipids with charged headgroups. Typically 20 mg lipid should dissolve well in 1 mL organic solvent. If a hydrophobic substance should be

loaded into the liposomes' bilayer, it should be mixed with the lipids in the organic solvents. Any hydrophilic substance that should be encapsulated in the liposomes, can be added later along with the hydration solution (see below).

Once the components are mixed, the solvents are removed by either using a dry argon or nitrogen stream or rotary evaporation. Latter is particularly useful when dealing with large amounts (> 1 mL) of organic solvents. Once the solvents are removed, a thin lipid film has formed on the surface of the round bottom flask. The lipid film should be dried thoroughly by placing the flask in a vacuum overnight, to ensure the complete evaporation of possible remaining solvents.

2. Hydration and vesicle formation
   Hydration of the dried lipid film is accomplished by simply adding an aqueous solution into the flask. Usually a buffer, e.g. Hepes or PBS, is used as aqueous solution to ensure a stable pH as a change in pH can cause osmotic pressure onto the final vesicles which forces them to shrink or bloat. For the hydration process it is important that the temperature of the lipid film and the aqueous solution is above the characteristic transition temperature T_c of the lipid component with the highest T_c. The temperature above T_c allows the lipids to hydrate in its liquid phase, which guarantees an easier vesicle formation. The hydration process should occur slowly and it can take up to one hour until the whole lipid film is removed from the flask wall. The obtained lipid suspension contains multilamellar vesicles of a heterogeneous size distribution.

3. Sizing of vesicles
   To obtain a homogenous size distribution of unilamellar vesicles, energy is required, as the entropy of the suspension is decreased. Usually the applied energy is either applied through sonication or extrusion.

   Sonication disrupts the multilamellar vesicles into SUVs, with sizes that depend on lipid composition and concentration, temperature, power and duration of sonication. Since it is nearly impossible to reproduce exactly the same conditions from batch to batch, differences in size distribution are not uncommon. Due to the small diameters of the vesicles and hence a very high degree of curvature, the small unilamellar vesicles that are produced via sonication are inherently unstable and will fuse to form lager vesicles.

   Extrusion is a technique in which the lipid suspension is mechanically pushed several times (> 15 times) through a polycarbonate filter with a defined pore size [138]. An odd number of pushes ensures that the syringe of the extruder that contains the final suspension is not the syringe that contained the starting suspension. Prior to the extrusion the multilamellar vesicles have to be disrupted in several freeze-thaw-cycles. Up to 5 cycles from liquid nitrogen temperature to a temperature above the highest T_c should be sufficient. This procedure facilitates the mechanical extrusion and improves the homogeneity of the final

size distribution. The extrusion process is facilitated a lot when being performed at a temperature above T_c. Otherwise the S_o phase of the vesicles might not pass through and hence block the polycarbonate filter, which makes an extrusion almost impossible. Usually a filter size of 100 nm is used to yield vesicles with a similar diameter that provides good stability, even for several months [20].

Giant unilamellar vesicle preparation Liposomes with a diameter of approximately 100 nm are not suitable for optical microscopy. Only the larger GUVs, with a diameter in the micro-meter range can be used for optical imaging methods. The challenge in GUV preparation is their unilamellarity and stability, whereas latter depends mainly on the lipid composition. The rapid preparation method [139] produces GUVs with a heterogeneous size distribution that are stable for at least some hours. In the following the method which was used in this thesis to prepare GUVs is described briefly.

The preparation of GUVs works similar to the preparation of liposomes. However, in this case the lipids have to be dissolved in chloroform at a concentration of ca. 100 mM. 20 µM of that stock solution are then added to a chloroform:methanol solution (ratio 10:2, 1000 and 200 µL) in a large round bottom flask (ca. 50 mL). Before the organic solvents get evaporated in a rotary evaporator, ca. 7 mL Hepes buffer (10 mM HEPES, 100 mM NaCl, pH 7.5) have to be added carefully along the flask walls to the solution. Next, the volatile organic solvents have to be removed by rotary evaporation down to 100 mbar. This should yield approximately 6 mL of a turbid solution containing HEPES buffer and the GUVs with a concentration of ca. 300 µM.

3.3.5 Physical characterization of lipid vesicles

Concentration determination: Stewart assay

After liposome preparation the concentration of the prepared stock solution was determined via the spectrophotometric Stewart assay [140]. The Stewart assay is based on the ability of phospholipids to form a one-to-one complex with ammonium ferrothiocyanate which absorbs light at 485 nm. Another method to determine the phospholipid concentration is the Bartlett assay [141], which is based on the destruction of the phospholipids to inorganic phosphate and its complex formation when adding ammonium molybdate and the following reduction to a blue colored complex by 4-amino-2-naphthyl-4-sulfonic acid during heating. The advantage of the Stewart assay over the Bartlett assay is that the presence of inorganic phosphate does not interfere and therefore PBS buffer or other phosphate based buffers can be used. However, one drawback of the Stewart assay is its inability to quantify phosphatidylglycerol (PG) because its headgroup does not form a complex with ammonium ferrothiocyanate.

Table 3.2 – Sample compositions for the Stewart assay absorbance calibration curve.

Sample	SFS / mL	Chloroform / mL	AFS / mL
0	0.0	2.0	2
1	0.1	1.9	2
2	0.2	1.8	2
3	0.4	1.6	2
4	0.6	1.4	2
5	0.8	1.2	2
6	1.0	1.0	2

The Stewart assay workflow is as follows:

- Prepare an ammonium ferrothiocyanate solution (AFS) that is stable for more than 12 months at room temperature by dissolving 27.0 g of ferric chloride hexahydrate and 30.4 g of ammonium thiocyanate in 1 L distilled water.
- Prepare a 10 mL standard phospholipid solution (SFS) by dissolving 0.1 mg/mL phospholipids in chloroform.
- Mix and vortex chloroform, AFS and SFS for 20 s as listed in table 3.2 in centrifuge tubes.
- Centrifuge the samples for 10 minutes at 1000 rpm.
- Remove the upper layer using a pipette.
- Measure the optical density of the remaining solutions at 485 nm. The absorbance calibration curve of POPC, representing a PC headgroup, is plotted in figure 3.15.
- Calculate the concentration of a phospholipid sample with unknown concentration from the fit of the absorbance calibration curve.

Size verification: Dynamic light scattering

Dynamic light scattering (DLS) is a common method to determine the size distribution of a suspension containing small particles such as lipid vesicles [142]. It is based on the detection of intensity fluctuations over time of Rayleigh scattered linearly polarized laser light that arise from the Brownian motion of the particles of interest in the suspension. Constructive or destructive interference of scattered laser light from different particles yield the fluctuating intensities. The intensity fluctuation contains information about the translational diffusion of the scattering particles which depends on their hydrodynamic radius. The dependence is given by the Stokes-Einstein

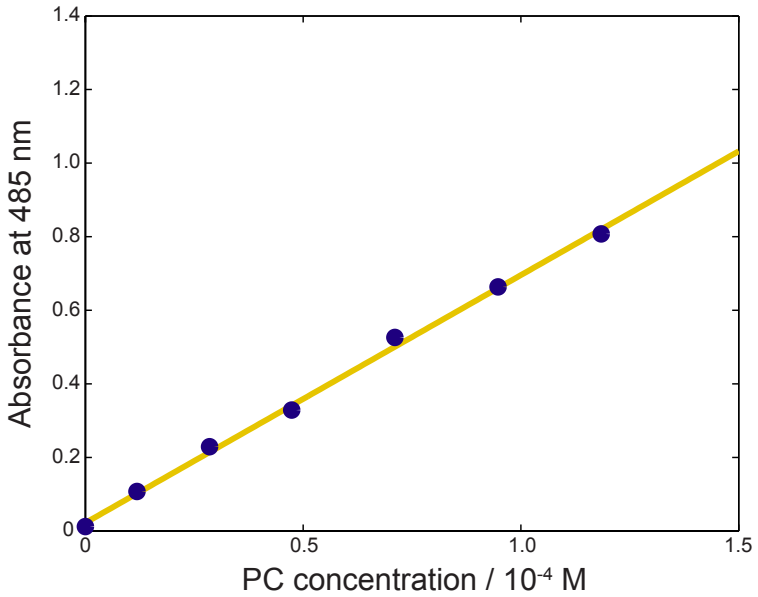

Figure 3.15 – Stewart assay absorbance calibration curve for phosphocholine (PC) headgroup lipids. The linear fit is $f(x) = 0.02218 + 6734x$.

equation, that relates the translational diffusion coefficient D, i.e. the "velocity" of the Brownian motion, of a spherical particle with radius r in a solvent with known temperature T and viscosity η via

$$r(\eta, T, D) = \frac{k_B T}{6\pi\eta D}. \tag{3.22}$$

It is important to note that the measured radius is the hydrodynamic radius, i.e. the size of for example a polymer can only be measured by its rotational averaged radius. Furthermore the obtained size will include any other molecules or solvent molecules that move close to the particle's surface.

Figure 3.16 demonstrates the stability of liposomes for a period of 83 days that was measured via DLS. The liposomes were prepared via extrusion with a filter size of 100 nm and loaded with CrA into their lipid bilayer. The sizes are listed in Table 3.3. The liposomes showed a slight swelling but did not break apart or formed larger vesicles up to 83 days. For the experiments usually liposomes were freshly prepared and used within 24 h after preparation.

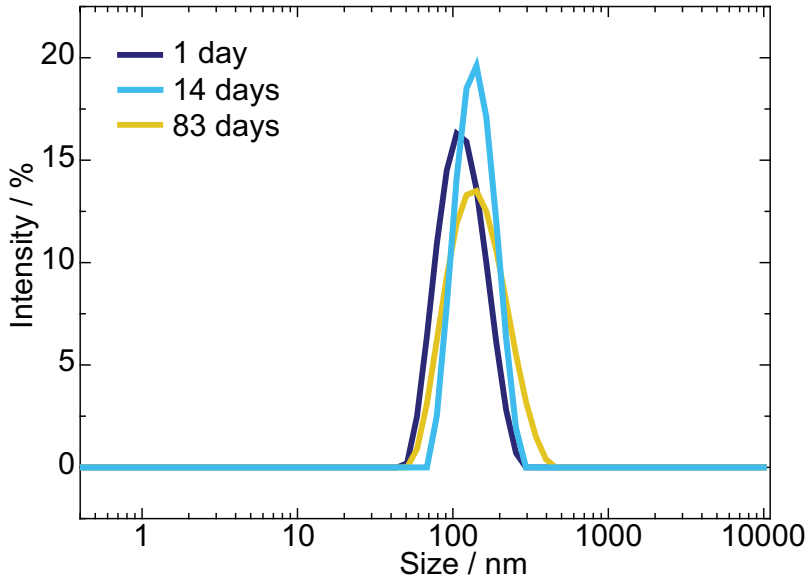

Figure 3.16 – Stability of liposomes loaded with CrA measured by DLS after one day, 14 days and 83 days.

Table 3.3 – Size distributions of liposomes loaded with CrA at different time points after preparation measured by DLS.

Day	size / nm
1	120 ± 20
14	144 ± 20
83	153 ± 32

3.4 Förster Resonance Energy Transfer

Förster Resonance Energy Transfer [143] between a membrane-associated dye Nile red [144] and fluorescently-labeled CrA molecules is used to determine the partitioning coefficients K_P of CrA molecules into the lipid bilayers of model biomembranes in section 4.1.1. For the determination of the partitioning coefficients some pre-knowledge about the studied FRET system is required, which is given in the following.

The FRET efficiency E depends on the distance R between the FRET pair and their FRET radius R_0, which is defined by the distance between the FRET pair at which the radiation-free energy transfer efficiency is 50 %:

$$E = \frac{R_0^6}{R_0^6 + R^6} \tag{3.23}$$

The FRET radius depends on the FRET pair and can be calculated via [145]

$$R_0 = \sqrt[6]{8.79 \times 10^{-5} \kappa^2 n^{-4} J Q_D}, \tag{3.24}$$

where κ^2 is the orientation factor of the dipole moments of the FRET pair, n is the refractive index of the surrounding medium, Q_D is the fluorescence quantum yield of the donor in absence of the acceptor and J is the integral of the spectral overlap of the donor emission and the acceptor absorption.

Usually the orientation factor κ^2 is assumed to be 2/3, when both, donor and acceptor, can freely rotate and diffuse in all three dimensions. In our case, the donor is embedded into the lipid bilayer which yields anisotropic conditions. Therefore, we chose $\kappa^2 = 5/4$, which has been used for similar FRET conditions [146, 147].

The refractive index n was taken as an average of the refractive index of water ($n = 1.33$) and lipid bilayers ($n = 1.42 - 1.49$) [148–151] and therefore was $n = 1.40$ for liposomes in the L_d phase and $n = 1.45$ for liposomes in the S_o phase.

The normalized overlap integral J can be calculated by

$$J = \frac{\int F_D(\lambda)\epsilon(\lambda)\lambda^4 \mathrm{d}\lambda}{\int F_D(\lambda)\mathrm{d}\lambda}, \tag{3.25}$$

where $F_D(\lambda)$ is the donor fluorescence intensity at the wavelength λ and $\epsilon(\lambda)$ is the acceptor molar extinction coefficient.

The fluorescence quantum yield of the lipid-bilayer embedded donor nile red Q_D was obtained by comparing its fluorescence intensity $F_D(\lambda)$ with the fluorescence intensity of a standard $F_S(\lambda)$ with a known quantum yield Q_S in solutions with known refractive indices n_D and n_S and absorbance factors f_D and f_S at the excitation wavelength λ_{ex} via [152]

$$Q_D = Q_S \frac{f_S(\lambda_{\mathrm{ex}}) n_D^2 \int F_D(\lambda)\mathrm{d}\lambda}{f_D(\lambda_{\mathrm{ex}}) n_S^2 \int F_S(\lambda)\mathrm{d}\lambda}. \tag{3.26}$$

The dyes rhodamine 101 ($Q_S = 0.90$) and cresyl violet ($Q_S = 0.55$) were chosen as standards as they are well established dyes with known quantum yields [153, 154]. Their quantum yields were mutually checked and yielded 0.92 and 0.53 for rhodamine 101 and cresyl violet, respectively. The determined quantum yields of nile red for the different liposomes are listed in table 3.4.

Table 3.4 – FRET parameters to calculate the partitioning coefficients in different liposomes.

Lipid	phase	Q_D[a]	V_{mol} / l/mol[b]	A_{L} / Å^2[c]	R_0 / Å
EYPC	L_d	0.67	0.76	69.4	73.7 ± 1.4
POPC	L_d	0.67	0.74	68.3	73.9 ± 1.4
DPPC	L_d	0.54	0.74	64.2	71.3 ± 1.3
DPPC	S_o	0.74	0.69	47.9	70.3 ± 1.5

[a]: Error 10 %.

[b]: According to references [155–157].

[c]: Average interfacial area per lipid molecule, assuming a 2D-sphere.

FRET measurements were performed at different lipid concentrations and different CrA-dye conjugate concentrations. The partitioning coefficients K_P were derived by performing a global fit analysis using the following equation that is known from two dimensional FRET experiments in phospholipid vesicles using other FRET pairs [158, 159], with the parameters listed in table 3.4

$$\begin{aligned} FI = f \cdot \{ & A_1 \exp\left[-k_1 C_{\mathrm{CrA,\ tot}} \frac{2R_0^2 K_P V_{\mathrm{mol}}}{A_{\mathrm{L}} + A_{\mathrm{L}} K_P V_{\mathrm{mol}} C_{\mathrm{L}}} \right] \\ & + A_2 \exp\left[-k_2 C_{\mathrm{CrA,\ tot}} \frac{2R_0^2 K_P V_{\mathrm{mol}}}{A_{\mathrm{L}} + A_{\mathrm{L}} K_P V_{\mathrm{mol}} C_{\mathrm{L}}} \right] \}. \end{aligned} \tag{3.27}$$

Therein FI is the detected donor fluorescence intensity, f corrects for the quantum yields of the dyes, A_1, A_2, k_1 and k_2 are dimensionless parameters that depend on the closest approach a of the FRET pair and the Förster radius R_0 (Table 3.5). The remaining parameters in equation 3.27 are the total concentration of the CrA-conjugate in the suspension $C_{\mathrm{CrA,\ tot}}$, the molar concentration of lipid molecules C_{L}, the lipid molar volume V_{mol}, the average interfacial area per lipid molecule A_{L} (see table 3.4).

Table 3.5 – Numerical parameters for the determination of partitioning coefficients by FRET via equation 3.27. Data is taken from reference [159].

a/R_0	A_1	A_2	k_1	k_2
0.0	0.6463	0.3537	4.7497	2.0618
0.25	0.6290	0.3710	4.5752	1.9955
0.5	0.6162	0.3838	4.0026	1.4430
0.7	0.6322	0.3678	3.1871	0.7515
0.8	0.6344	0.3656	2.7239	0.4706
0.9	0.6336	0.3664	2.2144	0.2909
1.0	0.6414	0.3586	1.7400	0.1285
1.1	0.6327	0.3673	1.3686	0.4654
1.3	0.6461	0.3539	0.4899	0.5633

Considering half the thickness of a POPC or DPPC lipid bilayer (ca. 18 Å) and a Förster radius of 70 Å the ratio a/R_0 of the closest possible approach and the Förster radius must be $0 < a/R_0 \leq 0.25$. Fitting sets of values of A_1, A_2, k_1 and k_2 for $a/R_0 = 0$ and 0.25 gave identical partitioning coefficients within error bars and an average thereof was used for the determination of the partitioning coefficients in section 4.1.1.

4

Results and Discussion

4.1 NMR signatures of CrA partitioning into pure model biomembranes

The first indications of an interaction between the xenon host CrA and phospholipids were discovered in 2010 by Meldrum *et al.* [21]. Xe in lipid-associated CrA produced a resonance (Xe@CrA_{lip}) around 70 ppm in the Xe NMR spectrum, with respect to the Xe gas phase signal as a chemical shift reference at 0 ppm. Thus, the lipid environment shifts the resonance of Xe encapsulated in CrA in aqueous solution (Xe@CrA_{aq}, at ca. 60 ppm) downfield by ca. 10 ppm. Figure 4.1 shows a Xe NMR spectrum where the Xe in H_2O, Xe@CrA_{aq} and Xe@CrA_{lip} resonances are visible. The observed large chemical shift difference of ca. 10 ppm is remarkable because the chemical shift difference of Xe in H_2O and Xe in lipids is significantly smaller (ca. 2 ppm, dependent on the lipid type; see also table 2.2). This small chemical shift difference might be caused by a Xe exchange in and out of the lipid environment that is fast on the NMR timescale and is only resolvable at temperatures close to 273 K. At room or body temperature the Xe in lipids resonance only appears as a shoulder on the Xe in H_2O resonance and only if the lipid concentration is high enough. Hence, the encapsulation of Xe into CrA paradoxically makes it more sensitive to its chemical environment than being free.

Very similar chemical shifts of the resonances are observed when Xe and CrA interact with cells such as macrophages [16], endothelial cells [20] or breast cancer cells [19]. An exception are red blood cells which produce a Xe resonance that is shifted downfield by ca. 24 ppm due to the presence of the iron-containing heme groups [160]. The similarities between the NMR signatures in model membranes and real cells motivated many of the studies in this thesis to systematically understand the Xe exchange in model membranes under well defined conditions.

Xenon's large sensitivity to its chemical environment combined with the paradoxically large chemical shift difference of ca. 10 ppm allows selective MRI using Hyper-CEST of either Xe@CrA_{aq} or Xe@CrA_{lip}. In 2010 the NMR pulse sequences and the Xe polarization were good enough to obtain selective MR images of Xe@CrA_{lip}

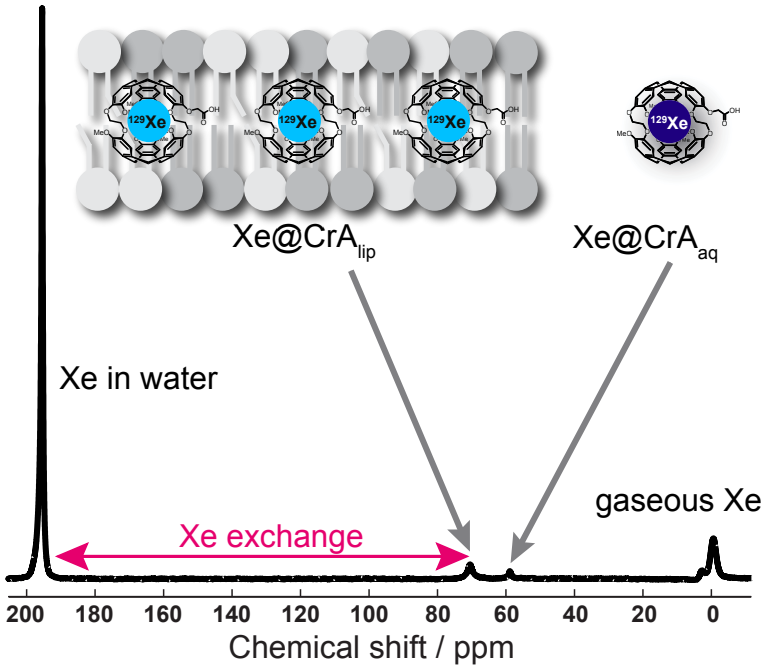

Figure 4.1 – ^{129}Xe-NMR-spectrum of 1.5 mM POPC and 50 µM CrA at 277 K (number of averages $N = 32$). Four of the five Xe pools are detected: Xe in gas phase (0 ppm), Xe@CrA$_{aq}$ ($\sim$ 60 ppm), Xe@CrA$_{lip}$ ($\sim$ 70 ppm) and Xe in H_2O ($\sim$ 195 ppm). Xe in lipid usually overlaps with Xe in H_2O and is not separable. Reproduced from reference [47]. Copyright © 2014 Elsevier Inc.

in the presence of 100 µM CrA at a Intralipid®[1] to water ratio of ca. 0.1 by volume [21]. The obtained image resolution of 14 mm^2 was obtained in ca. 14 min per data set using chemical shift imaging. Today, improved Xe polarization and optimized acquisition pulse sequences [76] enables us to effortless detect 20 µM CrA that interact with 500 µM egg yolk phosphatidylcholine (EYPC) in a single Hyper-CEST image acquisition that takes only ca. 15 s in total to yield an in-plane resolution of 0.2 mm^2. Figure 4.2 demonstrates this improved frequency-selective Hyper-CEST MR imaging.

The capability of Hyper-CEST to detect such a lipid environment-associated CrA ensemble at low concentrations enables for example to reduce cell density in solution in cell experiments. This should facilitate screening of novel Xe biosensors that are designed to specifically target a certain cell type, which might be difficult to culture. Furthermore a reduced cell density becomes important with regard to the relaxation of the hyperpolarized Xe atoms which can cause unwanted signal loss through a shortened T_2 relaxation time beyond certain cell concentrations.

[1] Intralipid® is a 20 % (by volume) sterile fat emulsion that is mainly used for intravenous administration to deliver calories and essential fatty acids. It contains 20 % soy bean oil, 1.2 % egg yolk PC, 2.25 % glycerin and H_2O.

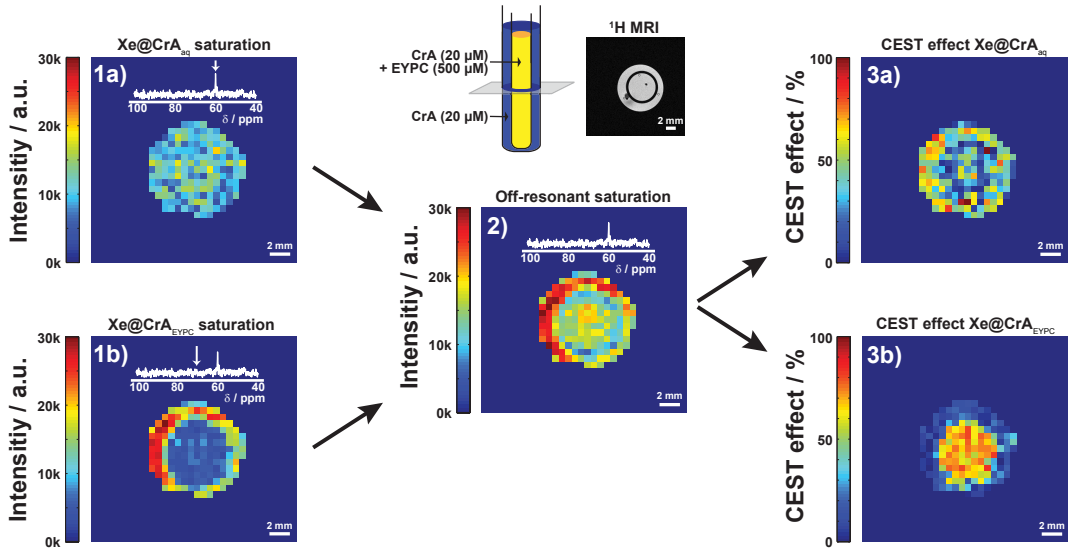

Figure 4.2 – Hyper-CEST MR Imaging of 20 µM CrA interacting with 500 µM EYPC at 296 K. Applying a saturation pulse to the Xe@CrA$_{aq}$ resonance at 60 ppm (1 a) and dividing by the intensity after off-resonant saturation at 303 ppm (2) yields signal for both compartments (a 5 mm NMR tube inside a 10 mm NMR tube) (3 a). When applying a saturation pulse to the invisible Xe@CrA$_{lip}$ resonance at 71.5 ppm (1 b) and dividing by the intensity after off-resonant saturation (2), only the inner compartment containing EYPC shows up (3 b). Saturation pulse parameters: $B_1 = 8$ µT, $t_{sat} = 8$ s.

4.1.1 Partitioning of CrA and Xe into lipid environment

Both Xe and hydrophobic CrA are taken up into lipid environments very efficiently and yield high local concentrations: The Xe solubility in phosphocholine lipids is ca. 14 times higher compared to that in water [4] and CrA concentrations of $10^{-5} - 10^{-4}$ M can partition completely into the lipid environment once the lipid fraction in aqueous solution is larger than 0.1 [21]. Latter was observed through the disappearance of the Xe@CrA$_{aq}$ resonance in a direct NMR spectrum once the lipid to water ratio was larger than 0.1. The high solubility of Xe and CrA in lipid environment provides favorable conditions for Hyper-CEST high-sensitivity detection, which allowed us to study the CrA-lipid interaction in more detail as demonstrated in this section.

This subsection is based on the collaborative publication [161] (Sloniec and Schnurr *et al.*, Biomembrane Interactions of Functionalized Cryptophane-A: Combined Fluorescence and ^{129}Xe NMR Studies of a Bimodal Contrast Agent, *Chem. Eur. J.* 19 (9), 3110 – 3118, 2013), which was published by Jagoda Sloniec and me within a shared first authorship .

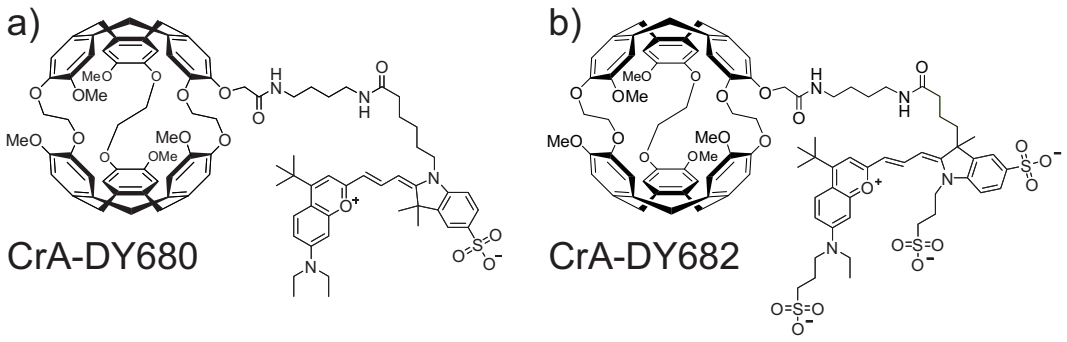

Figure 4.3 – Chemical structures of the two fluorescent CrA-dye conjugates CrA-DY680 (a) and CrA-DY682 (b).

Partitioning coefficients of fluorescent CrA-conjugates

The complementary use of fluorescence and NMR spectroscopy was chosen for a more detailed interpretation of NMR data. Hence, to prove and further investigate the partitioning of CrA into lipid bilayers we coupled chemically fluorescent dyes to CrA and performed fluorescent studies. The fluorescent dyes were hydrophobic DY680 and hydrophilic DY682 (Dyomics GmbH, Jena, Germany). We chose two different dyes to check whether the coupling of such relatively large molecules has big influence on the hydrophobicity-driven partition of CrA into the lipid environment. Figure 4.3 shows the chemical structure of CrA-DY680 and CrA-DY682. The chemical coupling was done in a collaboration with Andreas Hennig from the Bundesanstalt für Materialforschung (BAM). The two fluorescent dyes were selected according to their absorption and emission in the near infrared (NIR) range. Hence, the two CrA conjugates may also serve as potential future in vivo bimodal contrast agents and provide capabilities for MRI and fluorescence imaging of small animal models.

The partitioning of the CrA-dye conjugates into the lipid environment was first investigated by fluorescence microscopy. Therefore, 4 µM of either CrA-DY680 or CrA-DY682 were added to a suspension (10 mM Hepes, 100 mM NaCl, pH 7.5) that contained giant unilamellar vesicles of POPC. Figure 4.4 shows the obtained fluorescence microscopy images that feature a bright fluorescence in the lipid bilayer of the GUVs. In the medium surrounding the GUVs no fluorescence was observed for the hydrophobic compound CrA-DY680 and only a weak fluorescence was found for the more hydrophilic CrA-DY682, as depicted in Figure 4.5. The vesicle's cavity showed some minor fluorescence only in the case of CrA-DY680. Qualitatively this indicates a preferential association of the two CrA-dye conjugates with the lipid environment, as assumed by Meldrum et al. [21]. However, as to be expected, CrA-DY680 showed a stronger tendency to partition into the lipid environment than CrA-DY682, because of the difference in hydrophobicity.

The stronger tendency of CrA-DY680 to embed into lipid environment was also found via Förster Resonance Energy Transfer (FRET) [143]. For the FRET exper-

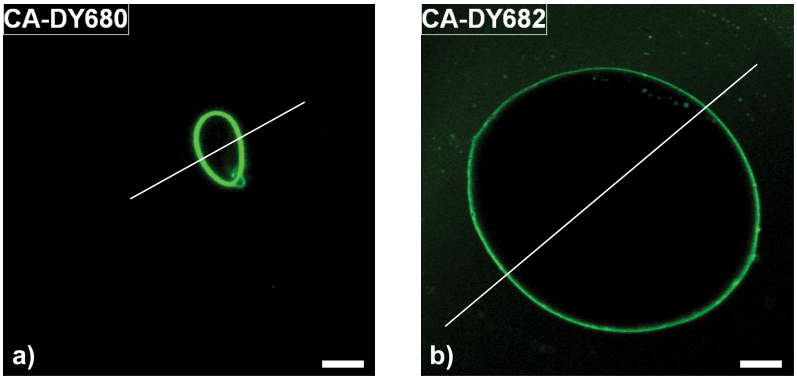

Figure 4.4 – Fluorescence microscopy of giant unilamellar POPC vesicles after addition of 4 µM CrA-DY680 (a) and CA-DY682 in 10 mM Hepes, 100 mM NaCl, pH 7.5 (b). Images were recorded with identical acquisition parameters. The final DMSO concentration in (a) was 1 vol-%. The length of the scale bar is 10 µm. The respective intensity profiles of the white diagonal lines are shown in Figure 4.5. Reproduced from reference [161]. Copyright © 2012 John Wiley & Sons, Inc.

iments we inserted the highly hydrophobic fluorescent dye nile red into the lipid bilayers and used it as the FRET donor. Figure 4.6 shows its absorption and emission spectra, as well as the absorption spectrum of CrA-DY680 in the Hepes buffer that was used for the experiments (10 mM HEPES, 100 mM NaCl, pH 7.3). Nile red was excited at 519 nm and the corresponding emission spectrum provided a large overlap with the absorption spectrum of CrA-DY680. This should yield an efficient energy transfer between the FRET pair.

To quantify the partitioning coefficients K_P (here defined as the ratio of the volume specific CrA-conjugate$_{lip}$ concentration (n_{lip}/V_{lip}) and CrA$_{aq}$ concentration (n_{aq}/V_{aq})) of CrA-DY680 and CrA-DY682 into the lipid bilayer via FRET, we observed the

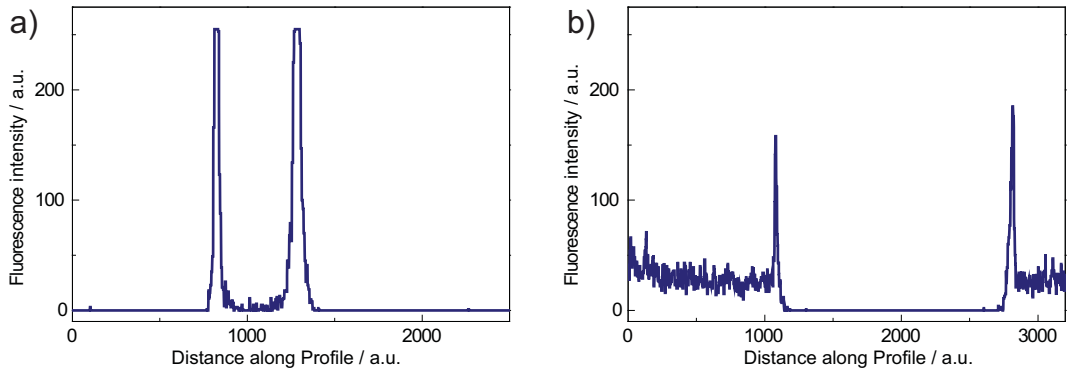

Figure 4.5 – Fluorescence intensity profiles of the straight lines through the fluorescence microscopy images shown in Figure 4.4 of CrA-DY680 (a) and CrA-DY682 (b). Reproduced from reference [161]. Copyright © 2012 John Wiley and Sons, Inc.

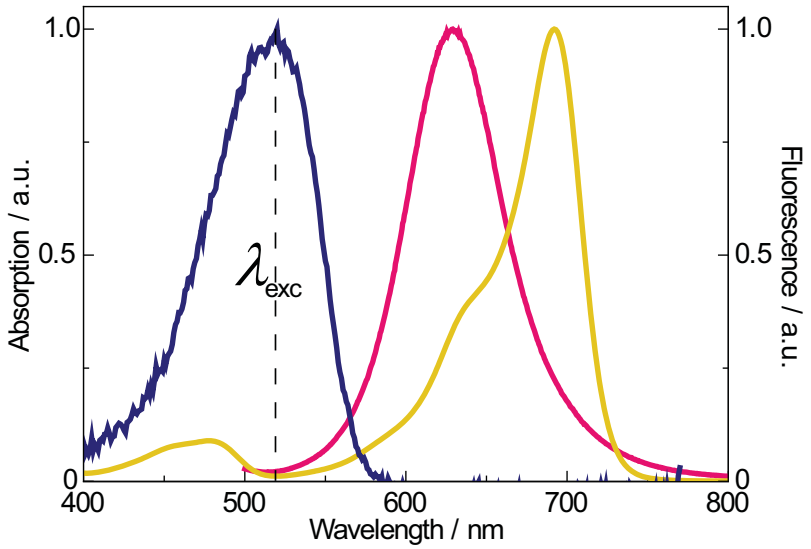

Figure 4.6 – Absorption (blue) and fluorescence spectrum (pink) of the FRET donor nile red and absorption spectrum of the FRET acceptor CrA-DY680 (yellow). Nile red was excited at 519 nm. Reproduced from reference [161]. Copyright © 2012 John Wiley and Sons, Inc.

change in fluorescence intensity of nile red at 625 nm upon adding CrA-DY680 or CrA-DY682. Because of the energy transfer the fluorescence intensity at 625 nm decreased with increasing CrA-conjugate concentration, whereas the fluorescence intensity for $\lambda > 700$ nm increased (Figure 4.7). We excluded a potential fluorescence quenching by the CrA molecule itself by an unchanged nile red fluorescence intensity upon addition of CrA without any conjugated dye. Furthermore, direct excitation of the CrA-conjugates was ruled out by the absence of fluorescence emission in the spectral region of the acceptor when nile red was omitted under otherwise identical conditions.

The determined partitioning coefficients, determined via equation 3.27 in a global fit analysis of different lipid concentrations, are listed in table 4.1, which was the average of an analysis with $a/R_0 = 0$ and 0.25. The overall higher K_P values for CrA-DY680 agree with its stronger tendency to partition into the lipid bilayer than CrA-DY682 as seen using fluorescence microscopy (Figure 4.4 and 4.5). However, the partitioning coefficients of both CrA-DY680 and CrA-DY682 were in the same order of magnitude in all the model biomembranes, even when the lipid phase was different. However, the Hyper-CEST approach revealed a larger difference as discussed next.

Hyper-CEST signatures of different phospholipids

As demonstrated with the fluorescence experiments (see above) both CrA-conjugates showed strong interaction with the lipid environment. Although the partitioning

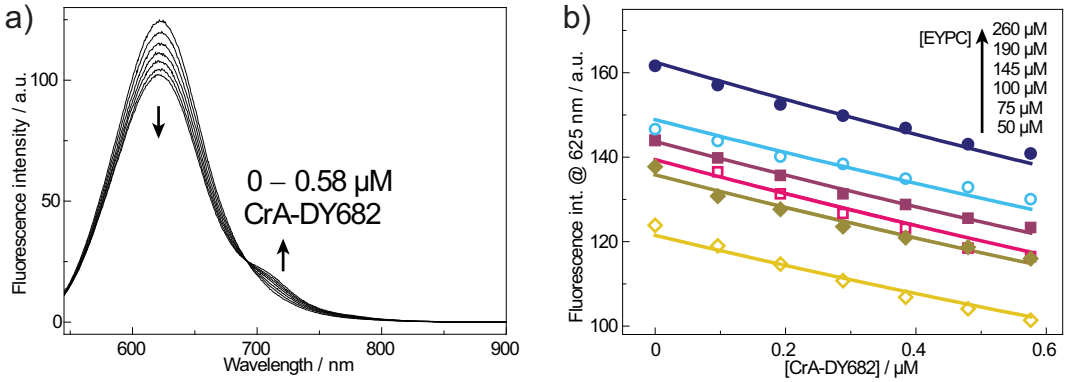

Figure 4.7 – (a) Example of fluorescence spectral changes of a solution containing 0.2 µM Nile Red and 50 µM EYPC upon addition of increasing amounts of CrA-DY682 ($0 - 0.58$ µM) ($\lambda_{exc} = 519$ nm). (b) Changes in donor fluorescence intensity ($\lambda_{em} = 625$ nm) with increasing amounts of CrA-DY682 at varying EYPC concentrations ($50 - 260$ µM). Fitted lines were obtained by global analysis of the titration data according to equation 3.27. Reproduced from reference [161]. Copyright © 2012 John Wiley and Sons, Inc.

Table 4.1 – Partitioning coefficients of CrA-DY680 and CrA-DY682 in liposomes of DPPC, POPC and EYPC at 298 K obtained by FRET measurements and equation 3.27.

Phospholipid	Lipid phase	K_P of CrA-DY680	K_P of CrA-DY682
DPPC	S_o	3500 ± 200	480 ± 40
POPC	L_d	1130 ± 120	620 ± 40
EYPC	L_d	1380 ± 70	700 ± 30

Errors are from global fitting analysis with different lipid concentrations ($N = 6$).

coefficients of CrA-DY682 were slightly lower than the ones of CrA-DY680, the NMR experiments focused on CrA-DY682, which comes along with better water solubility and therefore should have greater potential in future biological applications. In general, NMR and fluorescence measurements are challenging to compare as it is a known fact that fluorescence and NMR approaches commonly require different concentration ranges because of the much lower sensitivity of NMR [162]. Also in our case, conventional hyperpolarized ^{129}Xe NMR spectroscopy yielded no signal from only 4 µM CrA-DY682 after 16 acquisitions. However, with the high sensitivity provided by Hyper-CEST it was possible to sense the CrA-DY682 interaction at a concentration of 4 µM using NMR.

Figure 4.8 shows the Hyper-CEST-spectrum of 4 µM dissolved CrA-DY682 in Hepes buffer. Two peaks at ca. 63.5 ppm and 67.5 ppm were detected, which we ascribe to monomeric CA-DY682 and an aggregated form, respectively.

When model biomembranes of POPC, DPPC or EYPC were present in the solution a third larger peak appeared (Figure 4.9). It had the characteristic ca. 10 ppm downfield shift for CrA that interacts with lipid environments. Compared to

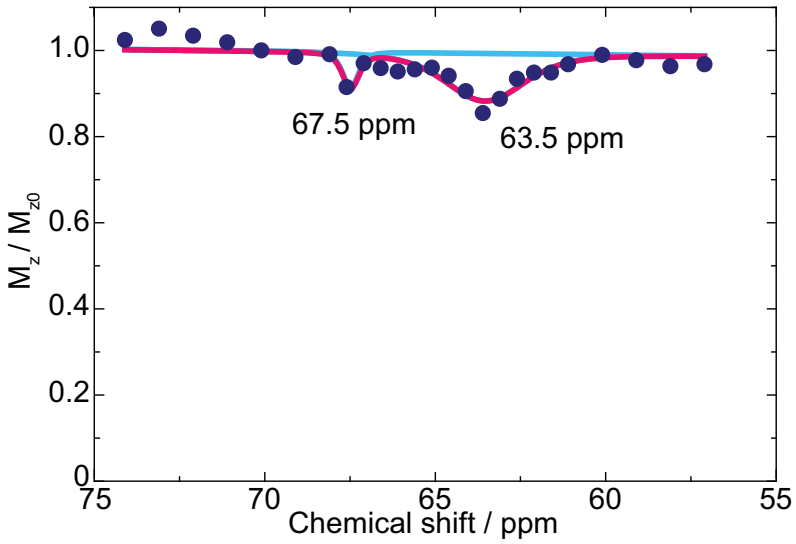

Figure 4.8 – Hyper-CEST spectrum of 4 µM CrA-DY682 in Hepes buffer at 298 K. The signal at 63.5 ppm corresponds to monomeric CrA-DY682 and the signal at 67.5 ppm to an aggregated form. Reproduced from reference [161]. Copyright © 2012 John Wiley and Sons, Inc.

the two resonances of monomeric and aggregated CrA-DY682, the CrA-DY682$_{\text{lip}}$ resonance was much broader and had similar chemical shifts for different phospholipids. Interestingly, the Hyper-CEST effects of the CrA-DY682$_{\text{lip}}$ resonances for different phospholipids did not reflect what would have been expected from the partitioning coefficients obtained from the fluorescence measurements, where CrA-DY682 had similar K_P values for all three phospholipids (Table 4.1). Here, Hyper-CEST revealed large differences in signal intensities as shown in Figure 4.9a – c. In particular, a much stronger Hyper-CEST effect was observed in the presence of POPC vesicles compared to EYPC and DPPC.

The stronger Hyper-CEST effect in POPC compared to DPPC and EYPC at 298 K could have different origins:

- a shorter T_2 relaxation time of Xe@CrA-DY682$_{\text{lip}}$
- an increased concentration of CrA-DY682
- an increased concentration of Xe@CrA-DY682$_{\text{lip}}$
- a higher Xe exchange rate in and out of CrA-DY682$_{\text{lip}}$
- a higher Xe exchange rate in and out of the lipid environment

A shorter T_2 relaxation time would lead to significant signal broadening in POPC. However, as depicted in Table 4.2 that is not the case, where the Hyper-CEST

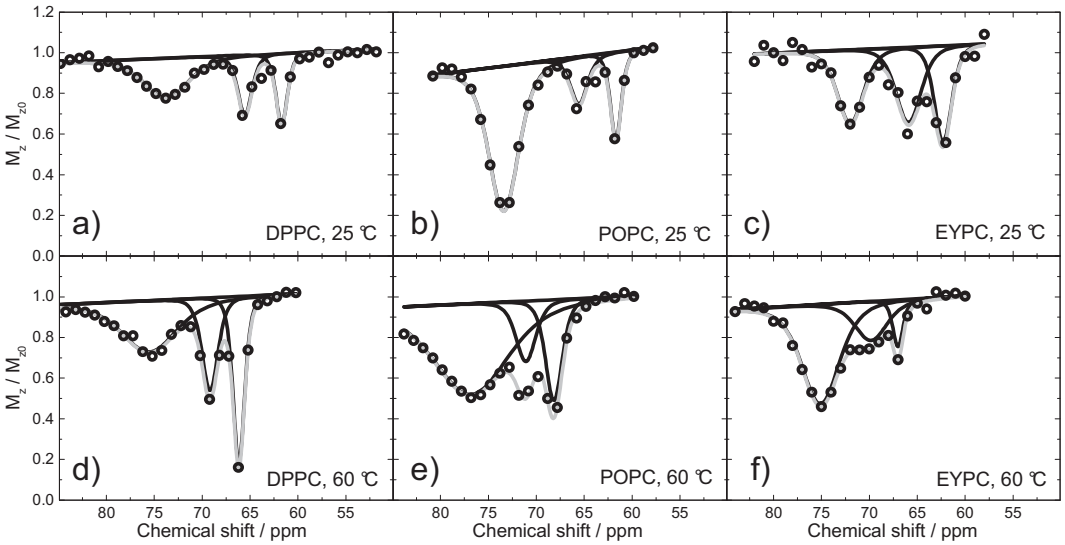

Figure 4.9 – Hyper-CEST spectra of 4 µM CrA-DY682 dissolved in Hepes buffer containing 200 µM DPPC (a, d), POPC (b, e) and EYPC (c, f) at 298 K (a – c) and 333 K (d – e). The black circles show the experimental data, the exponential Lorentzian fits (3.5) are shown as black lines and the corresponding sums as grey lines. Saturation parameters: $B_1 = 1.6$ µT, $t_{\mathrm{sat}} = 8$ s. Reproduced from reference [161]. Copyright © 2012 John Wiley and Sons, Inc.

response is the broadest for DPPC (by a factor of 1.5 to 1.7 compared to POPC and EYPC). An increased concentration of CrA-DY682 in POPC than DPPC contradicts the smaller partitioning coefficient for POPC compared to DPPC and can therefore also not be the origin of the stronger Hyper-CEST effect in POPC. An increased concentration of the Xe@CrA-DY682$_{\mathrm{lip}}$ can only be the result of a higher binding constant of Xe to CrA-DY682 in POPC. A higher Xe concentration in POPC, which would yield the same result, can also be ruled out by the similar Osswald solubilities of Xe in all phosphocholine based phospholipids [4]. A higher Xe exchange rate in and out of either CrA-DY682$_{\mathrm{lip}}$ or the lipid environment (or both) are the remaining possibilities that can cause the stronger Hyper-CEST effect in POPC compared to DPPC and EYPC.

Xe that participates in the Hyper-CEST labeling procedure has to penetrate into the membrane, travel to host sites and escape back into the aqueous solution to transport the information from induced depolarization. Hence, differences in membrane fluidity are expected (amongst other effects) to influence the efficiency of this process reflected in the intensity and build-up of the Hyper-CEST response. The effect of membrane composition has also been found to influence the MR signal in the context of MRI DIACEST agents [163].

The L_d phase in POPC at 298 K, that is characterized by the loose packing of the lipids that have a high lateral mobility, may facilitate permeation of Xe into the POPC bilayer as well as the intra-lipid diffusion of both CrA-DY682 and Xe compared

Table 4.2 – Chemical shifts and FWHM from the fits of the Xe@CrA-DY682$_{lip}$ resonances in POPC, DPPC and EYPC shown in Figure 4.9.

Phospholipid and temperature	Chemical shift /ppm	FWHM / ppm
DPPC, 298 K	73.7 ± 0.2	5.5 ± 0.5
DPPC, 333 K	75.5 ± 0.1	6.9 ± 0.4
POPC, 298 K	73.4 ± 0.1	3.7 ± 0.2
POPC, 333 K	76.8 ± 0.2	9.3 ± 0.5
EYPC, 298 K	72.0 ± 0.2	3.2 ± 0.5
EYPC, 333 K	75.1 ± 0.2	4.0 ± 0.3

to the S_o phase in DPPC. The presence of cholesterol, proteins and other molecules in the lipid-bilayer in natural EYPC can also have negative impact on the Hyper-CEST effect efficiency.

Indications that the lipid phase properties caused the different Hyper-CEST effects were obtained with Hyper-CEST experiments at 333 K, where both POPC and DPPC membranes are in the L_d phase. The Hyper-CEST spectra at the higher temperature are shown in Figure 4.9 d – f and the resonances details are listed in Table 4.2. The most apparent changes include a downfield shift of all resonances by approximately 2–3 ppm. However, the chemical shift difference between the monomer and the Xe@CrA-DY682$_{lip}$ resonance decreased for all three phospholipids. This is consistent with the initial experiments by Meldrum *et al.* [21] where a less pronounced temperature dependence was found for the Xe@CrA$_{lip}$ resonance compared to the Xe@CrA$_{aq}$ resonance. Furthermore, the FWHM of the Xe@CrA-DY682$_{lip}$ resonances consistently increased among all phospholipids, which was most apparent for POPC and thus the FWHM assimilated. This assimilation might be caused by the same lipid phase of DPPC and POPC at 333 K. The overall broadening of the resonances is most likely caused by thermodynamical effects that cause a higher exchange rate of Xe and a higher mobility of CrA-DY682.

More evidence that the Xe exchange rates are influenced by the lipid phase or the presence of cholesterol require more experimental data, which will be given in the following sections of this thesis. First, another detection technique is introduced that allows to extract more information from the broad Xe@CrA$_{lip}$ resonance.

4.1.2 Hyper-CEST with spatially separated biomembrane environments

Even though the large electron cloud of a Xe atom provides high molecular specificity and yields usually large chemical shifts in a NMR spectrum, conventional Xe NMR and Hyper-CEST are not applicable to distinguish resonances from Xe@CrA$_{lip}$ only by chemical shift as shown in section 4.1.1. Hence, an individual spectrum is not suitable for meaningful characterization of model biomembranes in terms of fluidity because the detected Xe@CrA$_{lip}$ resonance might be a superposition of different

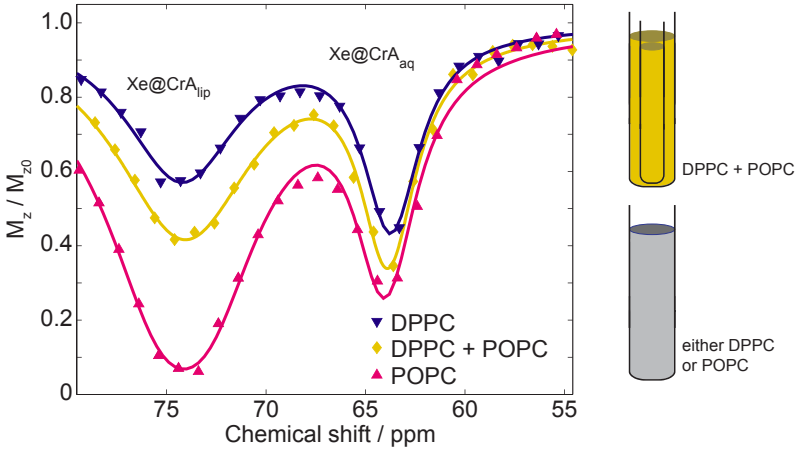

Figure 4.10 – Hyper-CEST-spectra of 5 µM CrA in 200 µM DPPC (blue triangles (down)), 200 µM POPC (pink triangles (up)) (each measured in a 10 mm NMR tube (b)) and two nested NMR tubes containing both solutions (yellow diamonds, a 5 mm NMR tube in a 10 mm NMR tube (c)) at 303 K. Saturation parameters $B_1 = 10$ µT, $t_{sat} = 5$ s. Reproduced from reference [164]. Copyright © 2013 Royal Society of Chemistry.

biomembrane environments that differ in fluidity. In this section the Depolarization Laplace Transform Analysis (DeLTA) is introduced as a useful measure to study and dissect the Xe@CrA_{lip} resonance and to allow to detect phospholipid environments which differ in membrane fluidity. This section is mainly based on publication [164] (Schnurr *et al.*, Functionalized ^{129}Xe as a Potential Biosensor for Membrane Fluidity, *Phys. Chem. Chem. Phys.* 15 (34), 14178 – 14181, 2013).

Hyper-CEST resonance superposition

Figure 4.10 demonstrates again how the Xe@CrA_{lip} resonances at ca. 74 ppm from 5 µM CrA interacting with 200 µM of either POPC or DPPC at 303 K have the same chemical shift and that it is not possible to resolve them according to their resonance frequency. In accordance with the experiments in section 4.1.1 that were performed with fluorescent CrA-conjugates the Hyper-CEST effect of CrA alone is again much less intense for DPPC than for POPC.

When we analyzed a Hyper-CEST spectrum of both, POPC and DPPC, simultaneously in neighboring compartments (yellow diamonds in Figure 4.10), also only a single resonance with an intermediate Hyper-CEST efficiency at 74.0 ppm was detected. This resonance should be made up of a superposition of the two resonances of POPC in the inner and DPPC in the outer compartment. Hence, all three resonances were similar in terms of chemical shift but different in depletion and width. Thus, the information about differences in depolarization build-up in different compartments that can origin from differences in membrane fluidity is lost when acquiring a global signal from the two nested NMR tubes simultaneously.

Resolving the superposition through DeLTA

Spatial information of the signal origin in NMR can be obtained by the use of MRI. We acquired Xe MR images of the two nested NMR tubes after applying saturation pulses of variable length ($t_{sat} = 10^{-3} - 20$ s) at 74 ppm (Figure 4.11). The MRI signal of the outer compartment, that contained DPPC, decreased slower compared to the MRI signal in the inner compartment that contained POPC. Thus, the difference in dynamic signal depletion of the two compartments was already visible when acquiring a stack of Hyper-CEST MR images with different saturation times. For example choosing $t_{sat} \sim 6$ s yielded sufficient contrast which allowed to distinguish the two compartments due to a larger signal in the outer compartment than in the inner compartment. Thus, we know that two compartments with different Hyper-CEST effects contributed to the intermediate (blue) resonance in Figure 4.10. However, still the signal of the inner and the outer compartment might be a superposition of multiple Hyper-CEST responses. To clarify, if the signals of the inner and outer compartment are superpositions of more signals we analyzed the MRI data further via DeLTA, as this approach can provide information about the number of decays.

Figure 4.11b shows the signal decays of both NMR tubes together and its the two individual compartments. The fits were obtained via DeLTA and the depolarization times are summarized in Figure 4.11c. They are the maxima of the corresponding depolarization time distributions which are inset into Figure 4.11c. The MR signal of the inner compartment showed a depolarization time $\tau_{POPC} = 3.00^{+0.77}_{-0.61}$ s and disappeared faster than the signal of the outer compartment which had a depolarization time $\tau_{DPPC} = 22.15^{+5.19}_{-4.16}$ s.

We ascribe the ca. 7-fold difference of the depolarization times to differences in membrane fluidity of the POPC and DPPC model biomembranes, as the lipid concentration, temperature, Xe concentration [4] and, as we know from section 4.1.1, the CrA concentration were the same in both compartments. The 7-times faster depolarization time in POPC than in DPPC is most likely caused by a higher turnover of Xe atoms that were depolarized during the saturation pulse. The same arguments as in section 4.1.1 hold for this.

In the discussed case we did not obtain more information by using DeLTA, except for the quantitative depolarization time. However, one big advantages of DeLTA over acquiring a Hyper-CEST spectrum is the much faster acquisition time. Acquiring a data set that contains sufficient enough data points so that DeLTA is applicable takes around 5 min whereas recording a Hyper-CEST spectrum takes around 10 min. The difference is because DeLTA takes also advantage of saturation pulses with short saturation times and requires only a few data points with long lasting saturation pulses. Additionally, DeLTA usually requires only around 10 data points to yield reliable results. Therefore, using DeLTA can allow to save some measurement time once the resonance frequency of interest is known. The real advantage of DeLTA becomes obvious next.

Interestingly, when analyzing the two nested NMR tubes together the depolarization time distribution yielded two different depolarization times, $\tau_{POPC^*} = 2.23^{+1.12}_{-0.73}$ s

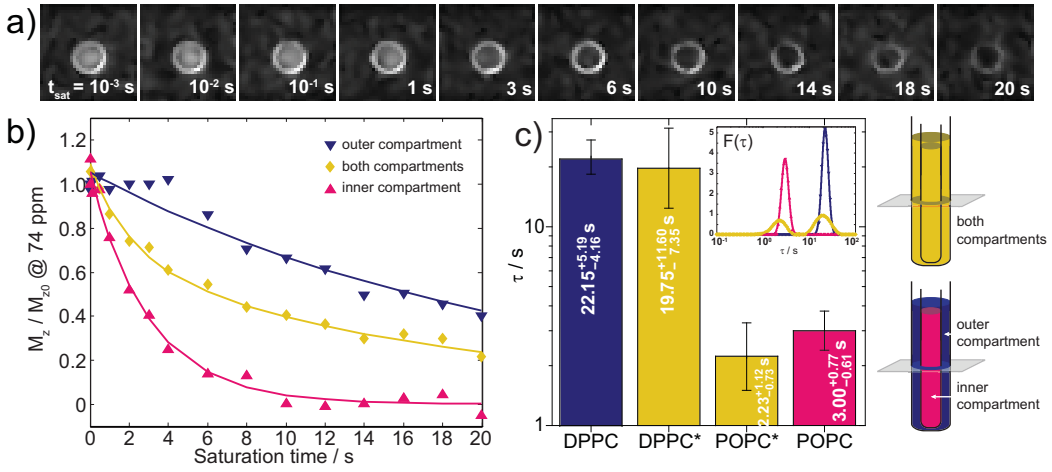

Figure 4.11 – Axial Hyper-CEST imaging (4 averages) of the two nested NMR tubes (a) with on-resonant saturation at 74.0 ppm with $B_1 = 10$ µT and variable t_{sat}. Images were smoothed using an adaptive weights filter with a local quadratic model [165]. (b) shows the decreasing Hyper-CEST signal $f(t_{sat})$ of both NMR tubes (yellow diamonds), only the outer compartment (blue triangles (down)) and only the inner compartment (pink triangles (up)). The solid lines are the fit results from the DeLTA. The outer compartment's noisy data might be the result of remaining gas bubbles in between the two glass walls during data acquisition. The depolarization times at the maxima of the probability density functions $F(\tau)$ (see inset) are shown in (c). Reproduced from reference [164]. Copyright © 2013 Royal Society of Chemistry.

and $\tau_{\mathrm{DPPC}^*} = 19.75^{+11.60}_{-7.35}$ s. τ_{POPC^*} can be assigned to τ_{POPC} and τ_{DPPC^*} to τ_{DPPC} because they are pairwise the same within errors. Thus the yellow signal in Figure 4.11b decays bi-exponentially. The information that the signal consists of two components can not be obtained from a Hyper-CEST resonance. It could only be obtained by introducing a further dimension that can be varied, the saturation time. However, it has to be mentioned, that DeLTA works only, if the amplitudes of the two components are similar. Otherwise one component dominates the other one.

MRI contrast based on membrane fluidity

The MR image series in figure 4.11 has a resolution of 32 × 32 pixels. With a field of view of 15 × 15 mm^2 this yields a 625 × 625 µm^2 in-plane resolution. Instead of taking the averaged signal from either the inner or the outer compartment one can further increase the resolution by analyzing every single pixel using DeLTA. This analysis, which took ca. 12 s per pixel, yielded a depolarization time distribution for every single pixel, as shown in the appendix in Figure A.1 and A.2. The pixels of the inner and the outer compartment clearly showed a single depolarization time in the distribution. Only a few pixels showed more maxima in the depolarization time

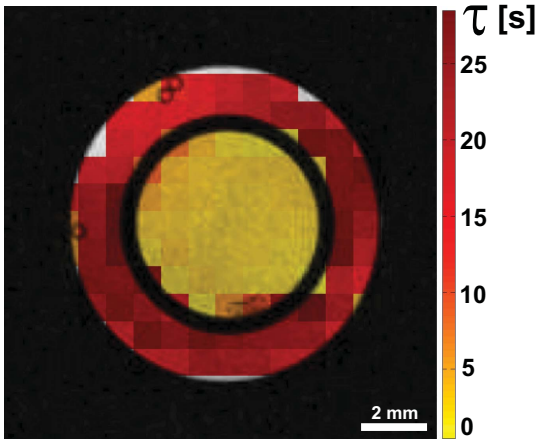

Figure 4.12 – Depolarization-time map of the two nested NMR tubes. A ^{1}H image is superimposed. For each pixel (625 x 625 µm^2 in plane resolution) the depolarization time is obtained via DeLTA that yields the corresponding depolarization time distribution that is shown in the appendix in Figure A.1 and A.2. Reproduced from reference [164]. Copyright © 2013 Royal Society of Chemistry.

distribution. Those pixels were mainly pixels with partial volume effects, mainly at the edge of a compartment, or in data sets with very low SNR.

Figure 4.12 shows the corresponding false-color encoded spatial distribution of the depolarization times of the two nested NMR tubes. The spatial distribution is in very good agreement with the results when analyzing the signal averaged compartments (Figure 4.11). If the number n of maxima in $F(s)$ for a certain pixel was found to be > 1 the dominant τ was assigned as that very pixel value. Furthermore, Figure 4.12 illustrates the applicability of generating MR-contrast based on different depolarization times in different molecular environments. The need for high resolution is obvious. Otherwise one might end up with multiple depolarization time maxima in a single pixel (think of a pixel as large as the two nested NMR tubes together).

4.1.3 Hyper-CEST dependence on host and lipid concentration

So far all, the results showed were obtained with a fixed CrA and lipid concentration. The experiments in this section demonstrate how the Hyper-CEST effect depends on the concentration of the host, the concentration of phospholipids and the type of phospholipid. Again, artificially prepared model membranes of either DPPC or POPC were used for the experiments.

Hyper-CEST spectra

First we acquired Hyper-CEST spectra at different lipid and CrA concentrations of both POPC and DPPC to get qualitative information about how the Hyper-CEST effect is built up at different concentrations of both CrA and lipids. Figure 4.13

shows the spectra. Almost throughout all Hyper-CEST spectra the two characteristic resonances were visible. The one at ca. 60 ppm can be assigned to Xe that interacts with dissolved CrA ($Xe@CrA_{aq}$), whereas the left one at ca. 72 ppm is assigned to Xe that interacts with lipid bilayer-embedded CrA ($Xe@CrA_{lip}$). As expected, in all spectra the Hyper-CEST effect of both resonances became more intense when the CrA concentration was increased, simply because more Xe atoms could become depolarized when more CrA was present.

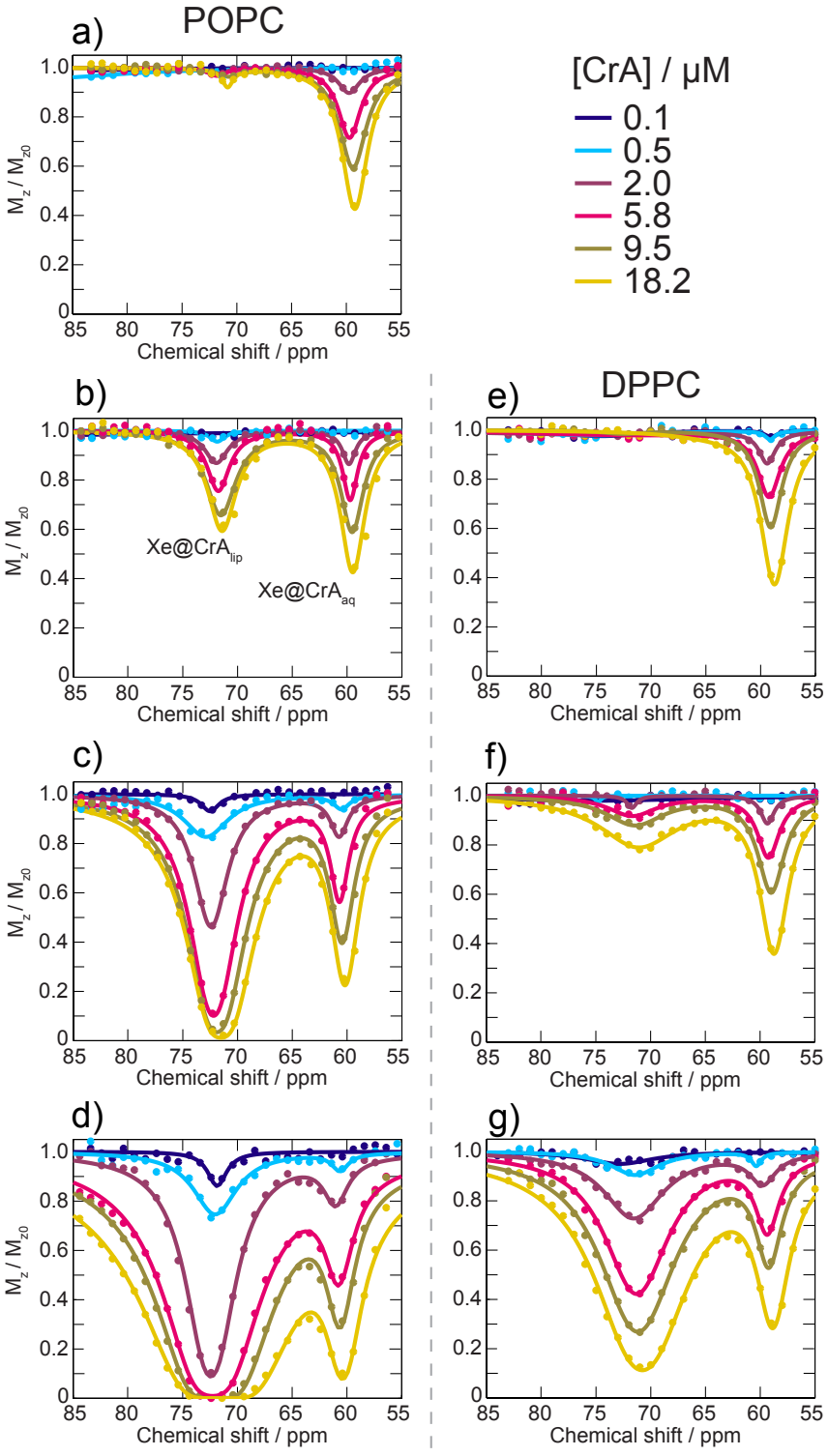

Figure 4.13 – Hyper-CEST spectra with varied POPC concentration (1 µM (a), 10 µM (b), 100 µM (c) and 1000 µM (d)) and DPPC concentration (10 µM (e), 100 µM (f) and 1000 µM (g)) at 293 K. The CrA concentrations were 0.1 – 18.2 µM. Saturation parameters: $B_1 = 10$ µT, $t_{sat} = 5$ s.

The Xe@CrA$_{aq}$ resonance: The Xe@CrA$_{aq}$ resonance was not affected when changing the lipid concentration, except for spillover effects from the Xe@CrA$_{lip}$ resonance. Figure 4.14 supports this when plotting only the fit functions of the Xe@CrA$_{aq}$ resonance, extracted from the fits in Figure 4.13. That the Xe@CrA$_{aq}$ resonance is not affected by changing the lipid concentration is particularly visible when comparing spectra where the two resonances do not overlap which was the case for POPC concentrations of 1 and 10 µM and for DPPC concentrations of 10 and 100 µM. From this we learn that although CrA is highly hydrophobic, the additional lipid volume (ca. 6.3×10^{17} (nm)^3 at a concentration of 1 mM)[2] provided by increasing the lipid concentration from 1 to 1000 µM does not change the Xe@CrA in H_2O resonance significantly. The larger amount of CrA in solution might explain this. The amount of CrA in solution should still be by a factor 10 larger than in lipid environment, assuming a partitioning coefficient of CrA without a dye of ca. 1000.

It is worth to note, that for both lipids, POPC as well as DPPC, the Xe@CrA$_{aq}$ resonance behaved very similar upon changing the CrA concentration. This can also be explained with the tendency of CrA to embed into the lipid bilayer which should be similar for both phospholipids, as they provide a similar hydrophobic environment with similar dimensions and as it is demonstrated in section 4.1.1 by the similar partitioning coefficients for the CrA-dye conjugates. Thus, for the Xe@CrA$_{aq}$ resonance we can summarize that it did neither depend on the lipid concentration nor on the lipid type.

[2] 1 mM of phospholipids in a total volume of 1.5 mL equal 1 mM×1.5 mL= 1.5×10^{-6} mol= 9×10^{17} phospholipids. With a diameter of 100 nm one liposome contains ca. 86000 phospholipids [166] and its hydrophobic lipid bilayer core has a volume of ca. 60352 (nm)^3. Thus the overall volume of the lipid environment is ca. 6.3×10^{17} (nm)^3. The overall volume of the aqueous solution is 1.5 mL = 1.5×10^{21} (nm)^3.

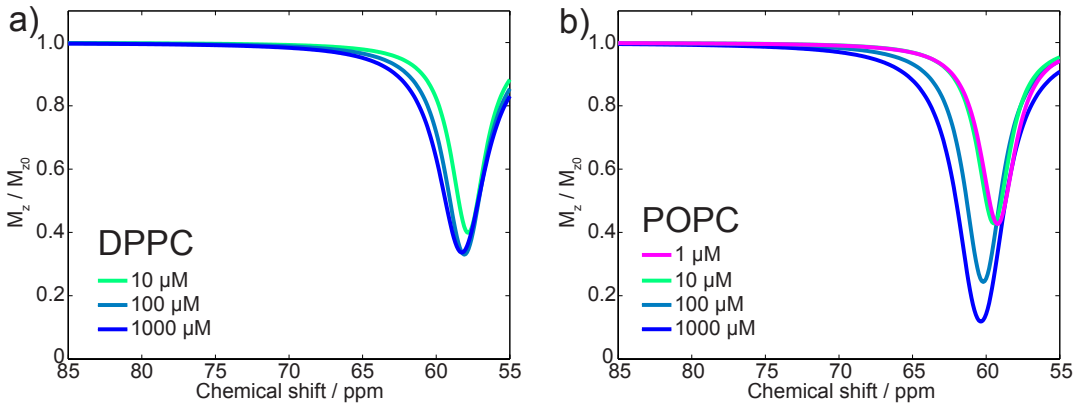

Figure 4.14 – Comparison of the Xe@CrA$_{aq}$ resonance fits in the presence of different concentrations of DPPC (a) and POPC (b), extracted from the fits in Figure 4.13.

The Xe@CrA$_{lip}$ resonance: The results are completely different for the Xe@CrA$_{lip}$ resonance. It depends strongly on the lipid concentration and the lipid type. At a POPC concentration of 1 µM almost no resonance was visible at any measured CrA concentration (Figure 4.13). However, already at a POPC concentration of 10 µM the Xe@CrA$_{lip}$ and the Xe@CrA$_{aq}$ resonances were similar in terms of depth and width (Figure 4.13b), whereas at higher POPC concentrations the Xe@CrA$_{lip}$ resonance was even more pronounced than the Xe@CrA$_{aq}$ resonance for all CrA concentrations (Figure 4.13c and d). This can be explained with the fact that hydrophobic CrA prefers to embed into lipid environment and that Xe reveals a 14-fold higher solubility in phosphocholine-based lipids than in water [4]. Hence, the local higher concentrations of the hosts and guests can produce a more efficient Hyper-CEST effect. This also means that the NMR detection limit of CrA can be pushed further down by taking advantage of the interaction with phospholipids. This can for example be helpful, if one aims to detect very low concentrations of a novel synthesized CrA-conjugate. Furthermore, this is promising for in vivo experiments in the future, as long as a big part of the tissue is made up of lipids.

Such a strongly pronounced Hyper-CEST response as in POPC liposomes was not found in DPPC liposomes (Figure 4.13e – g). A DPPC concentration of 10 µM was not sufficient to generate a Xe@CrA$_{lip}$ resonance – with the used saturation pulse power and time (Figure 4.13e). Therefore data was not acquired at DPPC concentration lower than 10 µM. At 100 µM the resonance was visible for CrA concentrations larger than 2 µM (Figure 4.13f). Compared to the resonances at 100 µM POPC the corresponding DPPC resonances were much less pronounced, yet broadened but did not surpass the intensity of the Xe@CrA$_{aq}$ resonances. Not before using a DPPC concentration of 1000 µM (Figure 4.13g), the Xe@CrA$_{lip}$ resonances were deeper than the Xe@CrA$_{aq}$ resonances at any measured CrA concentration. The observation that the Xe@CrA$_{lip}$ resonances of DPPC were less pronounced compared to the ones of POPC is consistent with results from section 4.1.1. Again, this can be explained with the different membrane phases of the lipid bilayers. At 293 K, the temperature used in the experiments, DPPC membranes are in the S_o phase whereas POPC membranes are in the L_d phase. The characteristic high lateral mobility and tumbling of the phospholipids in the L_d phase should facilitate the permeation of Xe in and out of the membrane. This should also influence the exchange dynamics of Xe in and out of CrA$_{lip}$ providing a more efficient Hyper-CEST effect in a biomembrane that possesses a high fluidity, such as POPC.

Depolarization times

The non-linearity of the Hyper-CEST effect, its dependence on several parameters and in particular the presence of four spin pools complicate a quantitative comparison of the Hyper-CEST effects spectra via fitting routines [79]. Recording the depolarization processes by fixing the frequency of the saturation pulse to the Xe@CrA$_{lip}$ resonance and varying its length from 10^{-4} to 20 s facilitates the situation. This allows to

quantify and thus to compare the efficiency of the Hyper-CEST effects in between different data sets with a single number, the depolarization time τ.

The recorded depolarization processes in presence of POPC and DPPC are shown in Figure 4.15. The fits were obtained via DeLTA. The mono-exponential depolarization process got faster with increasing CrA concentration and increasing lipid concentration. Hence, qualitatively the same can be said as in the discussion of the Xe@CrA_{lip} resonances in the Hyper-CEST spectra. However, the dependence of the depolarization time on the CrA and lipid concentration (Figure 4.16) can yield more information, as discussed next.

For DPPC the maximum depolarization time ((180 ± 34) s) was found for 0.5 µM CrA and 10 µM lipids. Its fastest depolarization time ((2.4 ± 0.3) s) was found for 18.2 µM CrA and 1000 µM lipids. At the same conditions, but with POPC instead of DPPC, the fastest depolarization time was (0.35 ± 0.03) s. For POPC the slowest depolarization time was found for 0.1 µM CrA and 10 µM lipids. At any measured concentrations of CrA and lipids the depolarization was more efficient in the presence of POPC than of DPPC.

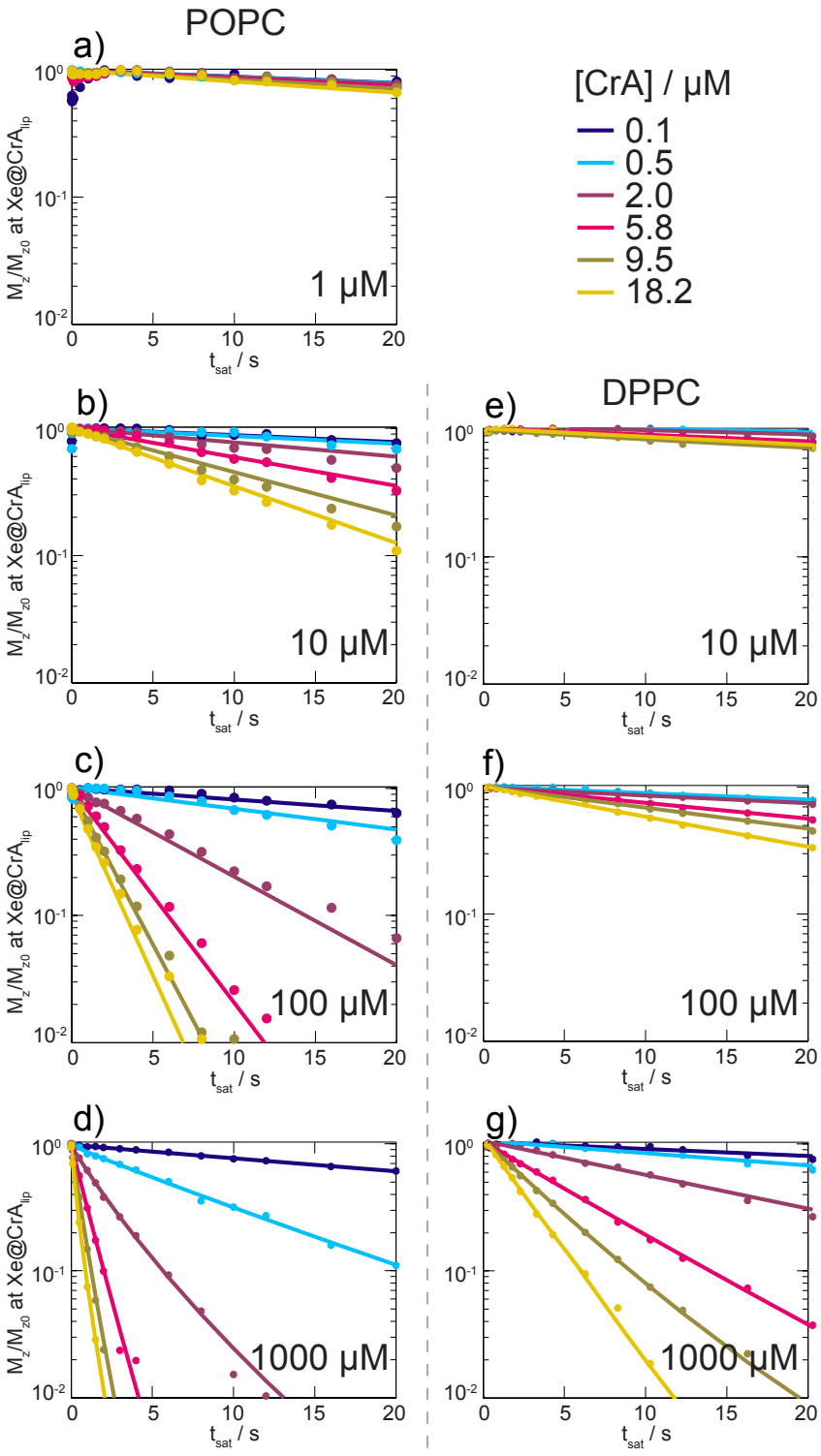

Figure 4.15 – Depolarization processes by varying the saturation time of varied POPC concentration (1 µM (a), 10 µM (b), 100 µM (c) and 1000 µM (d)) and DPPC concentration (10 µM (e), 100 µM (f) and 1000 µM (g)) at 293 K. The CrA concentrations were 0.1 – 18.2 µM. Saturation parameter B_1 = 10 µT. The fits were obtained via DeLTA and the obtained depolarization times are plotted in Figure 4.16.

Dependence of τ on the lipid concentration: When the CrA concentration was kept constant and the lipid concentration was varied (Figure 4.16a – f) the decrease of τ_{POPC} as well as of τ_{DPPC} with increasing lipid concentration could be modeled very well with a power law of the type

$$\tau(x) = \alpha x^{-\beta}, \tag{4.1}$$

where x represents the lipid concentration. The constant factor α determines the overall depolarization efficiency, whereas the β-exponent determines the slope in a log-log plot and thus, in this case, the dependence on the lipid concentration.

The β-exponents obtained from the fits are listed in Table 4.3. In general, the exponents for POPC are larger than for DPPC. We hypothesize, that changing the concentration of unsaturated phospholipids (POPC) had a bigger impact on the Hyper-CEST effect than changing the concentration of saturated phospholipids. However, starting out with nearly a 5-fold difference in β (0.14 ± 0.07 s for POPC vs. 0.03 ± 0.01 s for DPPC), with increasing CrA concentration the β-exponents became more similar and were the same within the error for [CrA] $\geq$ 5.8 µM. The large difference at low CrA concentrations might be due to a hindered Xe exchange in and out of $\mathrm{CrA_{lip}}$ in the lipid bilayer. This should result into a less efficient Hyper-CEST effect in DPPC. Once enough CrA was available inside the lipid bilayer to depolarize the initially available lipid embedded Xe atoms during the saturation pulse, the difference might only be given by the difference of Xe permeation into the lipid bilayer. As already mentioned above, the permeation of Xe atoms into DPPC should be much more difficult because of the much more densely packed and ordered phospholipids, which should have produced the overall slower depolarization times in DPPC.

Table 4.3 – β-exponents of the power function fits shown in Figure 4.16. In the first part the lipid concentration was varied and the CrA concentration was kept constant and vice versa in the second part.

fixed parameter	β-exponent		Figure 4.16
[CrA] / µM	POPC	DPPC	
0.1	0.14 ± 0.07	0.03 ± 0.01	a
0.5	0.44 ± 0.01	0.30 ± 0.01	b
2.0	0.52 ± 0.03	0.47 ± 0.07	c
5.8	0.59 ± 0.07	0.60 ± 0.09	d
9.5	0.72 ± 0.10	0.60 ± 0.20	e
18.2	0.74 ± 0.05	0.74 ± 0.08	f
[lipid] / µM	POPC	DPPC	
10	0.50 ± 0.08[a]	0.33 ± 0.10[a]	g
100	0.79 ± 0.10[a]	0.45 ± 0.05[a]	h
1000	0.92 ± 0.03	0.70 ± 0.05	i)

[a]: data at [CrA] = 0.1 µM was not considered for the fit

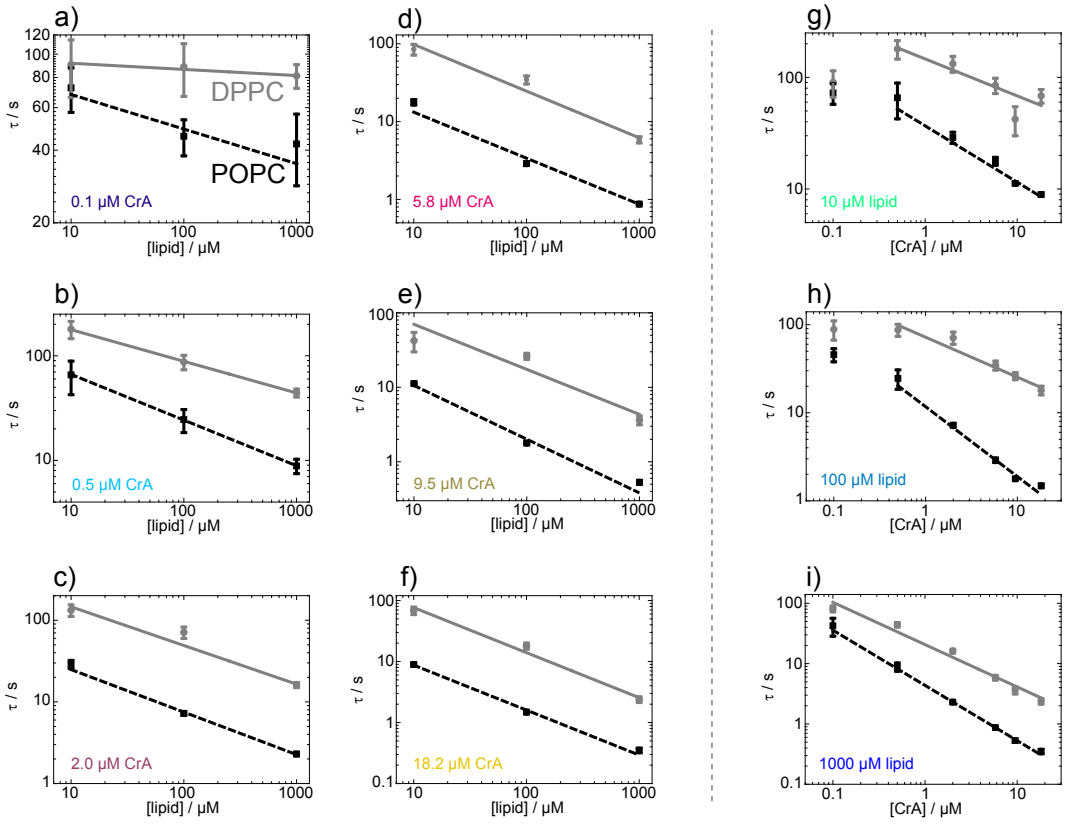

Figure 4.16 – Depolarization times of Xe@CrA_{lip} in presence of POPC (black squares, dashed line) and DPPC (grey circles, solid line) at different lipid concentrations (a) – f)) and at different CrA concentrations (g) – i)). The fits are a power function $\alpha x^{-\beta}$, in which x stands for the concentration either of the lipids or CrA. The β-exponents are listed in table 4.3.

Dependence of τ on the CrA concentration: Next we checked the influence of different CrA concentrations with fixed lipid concentrations on the Hyper-CEST effect (Figure 4.16g – i). Interestingly, for a lipid concentration of 10 and 100 µM the data with [CrA] $\geq$ 0.5 µM could also be modeled with the power law from equation 4.1, this time with x representing the CrA concentration. Yet, towards small CrA concentrations (0.1 µM) the depolarization time did level off and could not be fitted with the power law. The kink seems to be more pronounced for DPPC compared to POPC. Furthermore, at 10 µM DPPC the depolarization times for 0.1 and 18.2 µM CrA were not significantly different ((90 ± 24) s and (68 ± 10) s, respectively, Figure 4.16g). This indicates, that at such low lipid concentrations the amount of Xe atoms, that were present in the lipid environment was very small and all lipid-associated Xe atoms were depolarized completely after a short time when applying the saturation pulse. To depolarize more Xe atoms during the saturation pulse, more atoms had to permeate from the surrounding solution into the lipid bilayer. As mentioned above

this should be more difficult in DPPC. Such an effect was not observed at high lipid concentrations, where enough capacity for the Xe atoms should be provided by the lipid environment. Thus, at high lipid content the difference in depolarization time should mainly be determined by the Hyper-CEST dynamics inside the lipid bilayer and the permeation of Xe into the lipid bilayer should be less important.

Comparison of $\tau_{\mathbf{DPPC}}$ and $\tau_{\mathbf{POPC}}$: The depolarization times in POPC and DPPC are summarized in Figure 4.17, where the ratio $\tau_{\mathrm{DPPC}}/\tau_{\mathrm{POPC}}$ is plotted for every CrA (a) and lipid (b) concentration. At a CrA concentration of 0.1 µM the ratio is close to one over the whole range of lipid concentration. The ratio increases only slightly over the whole lipid concentration when a CrA concentration of 0.5 µM was used. Hence, in that case the determining factor of the depolarization process was the small amount of CrA. Providing more lipid environment did neither result into a more efficient depolarization process for POPC over DPPC nor vice versa.

When more CrA was used, the effect of different lipids became more significant and the ratio was 14.7 ± 1.5 at maximum with a lipid concentration of 100 µM and a CrA concentration of 9.5 µM. In general the ratio was the largest for a lipid concentration of 100 µM (for [CrA] $\geq$ 2 µM). We believe that the provided volume by 100 µM of lipids was not saturated with CrA as it should be the case with the 10 times smaller volume provided by 10 µM lipids, in which enough $\mathrm{CrA_{lip}}$ was present to depolarize all the lipid associated Xe atoms during the saturation pulse. Therefore, more Xe that permeated into the lipid bilayer could be depolarized additionally. Thus, the hindered permeation of Xe atoms into the DPPC bilayer produced the large ratio $\tau_{\mathrm{DPPC}}/\tau_{\mathrm{POPC}}$. At a lipid concentration of 1000 µM the ratio $\tau_{\mathrm{DPPC}}/\tau_{\mathrm{POPC}}$ decreased to ca. 7. We believe that this lipid concentration was large enough to host more Xe atoms than the number of atoms that could be depolarized during one saturation pulse. Thus, the contribution to the Hyper-CEST effect of the additional Xe atoms that permeated into the lipid bilayer was negligible. Hence, the ratio $\tau_{\mathrm{DPPC}}/\tau_{\mathrm{POPC}}$ is only determined by the difference in exchange rate of Xe in and out of CrA that is embedded in the lipid bilayer.

4.1.4 Summary

The improved sensitivity compared to 2010 [21], due to higher Xe polarization combined with the stable Xe redelivery that produced a shot-to-shot noise in the range of ca. 1 %, enabled us to study the interaction of Xe and CrA with lipid environments in a detailed manner as it has not been done before. The fluorescence experiments with novel synthesized CrA-dye conjugates verified the assumption by Meldrum *et al.* [21] and Boutin *et al.* [98] that the resonance at ca. 70 ppm is caused by CrA-lipid interaction. The Hyper-CEST resonances at ca. 70 ppm behaved clearly different for different model biomembranes, yet they were not separable by chemical shift. This could be bypassed by introducing DeLTA, which allowed us to dissect the $\mathrm{Xe@CrA_{lip}}$ resonances and to generate a novel type of MRI contrast that depends on

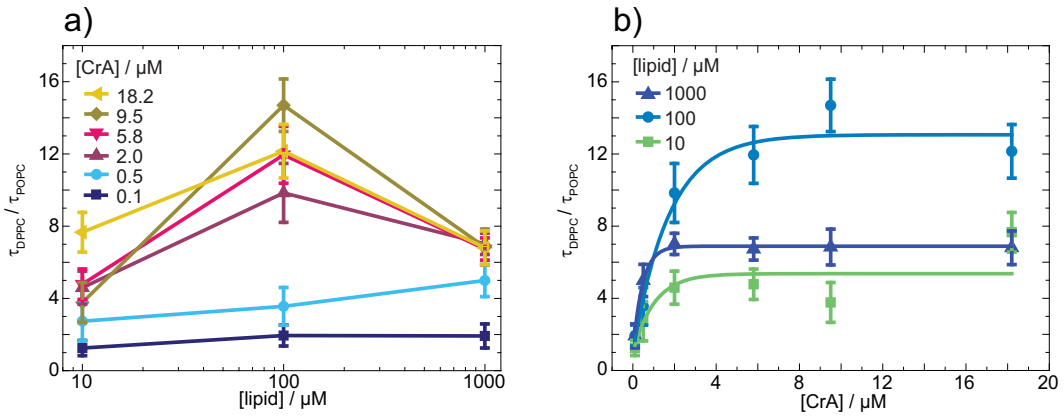

Figure 4.17 – Ratio of the depolarization times τ_{DPPC} and τ_{POPC} in dependence of the lipid concentration at different CrA concentrations (a) and in dependence of the CrA concentration at different lipid concentrations (b).

membrane fluidity. However, it is important that the same concentration of CrA, Xe and lipids is used when comparing the depolarization times caused by different model biomembranes. This is because the depolarization time depended strongly (power laws) on the CrA and lipid concentrations and it seemed that different regimes exist, where the build-up of the depolarization process is dominated by different exchange processes. As the field of Hyper-CEST NMR spectroscopy and MRI is moving towards the first in vivo experiments and hence quantification is becoming more important, it is inevitable to consider the biophysical properties of membranes that can yield significantly different Hyper-CEST effects.

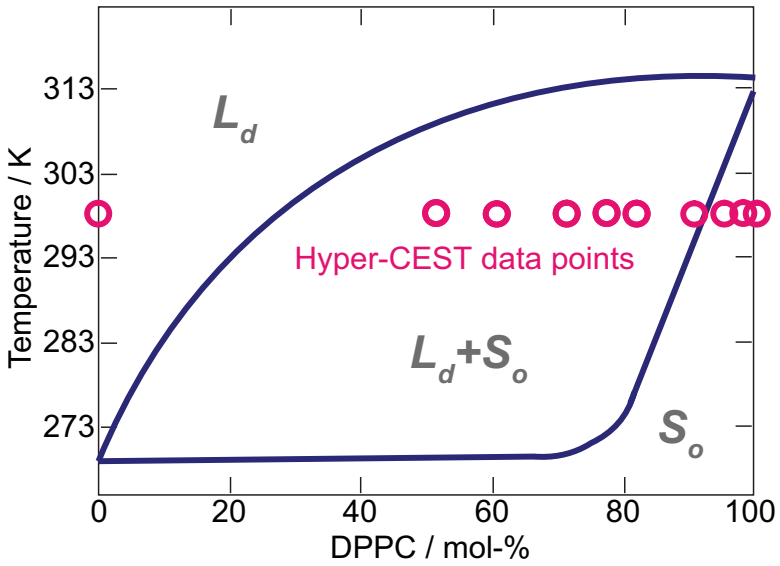

Figure 4.18 – Schematic binary DPPC:POPC phase diagram. The pink open circles indicate the parameters that were used for the Hyper-CEST experiments. Reproduced from reference [47]. Copyright © 2014 Elsevier Inc.

4.2 Sensing Lipid rafts and cholesterol content using Hyper-CEST

Biomembranes that consist of either DPPC or POPC are in the S_o or L_d phase, respectively, as introduced in section 3.3.2. As demonstrated in section 4.1 the Hyper-CEST approach is able to distinguish the different lipid phases. However, in the previous experiments the biomembranes consisting of DPPC or POPC were separated in different NMR test tubes. This may be at best a simplified representation for the spatial separation of for example tumor tissue surrounded by healthy tissue if both tissues differ in membrane fluidity, yet the composition of real cell membranes is much more diverse. For example, when already only two different types of phospholipids, e.g. DPPC and POPC, are mixed in a single biomembrane, lipid rafts can be formed and their domain size can fluctuate at certain concentration and temperature regimes [135].

Figure 4.18 shows the conditions that were used in the Hyper-CEST experiments on top of a schematic phase diagram of DPPC:POPC mixtures based on differential scanning calorimetry measurements [134, 135] (see also Figure 3.14). The work presented in this section is mainly based on the publication [47] (Schnurr *et al.*, Depolarization Laplace Transform Analysis of Exchangeable Hyperpolarized ^{129}Xe for Detecting Ordering Phases and Cholesterol Content of Biomembrane Models, *Biophys. J.* 106 (6), 1301 – 1308, 2014).

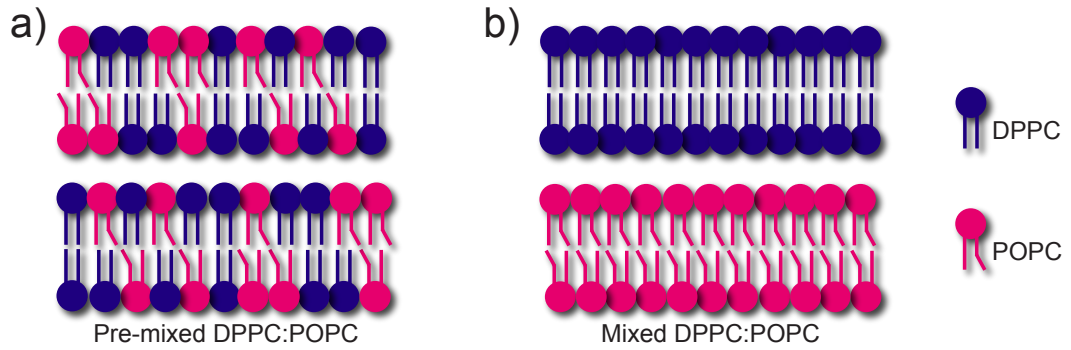

Figure 4.19 – Schematic representation of pre-mixed (a) and mixed (b) DPPC:POPC lipid bilayers.

The first part of this section demonstrates the ability of Hyper-CEST and DeLTA to sense lipid raft formation and their domain size fluctuations in biomembranes of lipid mixtures. Therefore we prepared different mixtures of DPPC and POPC containing vesicles. First, we studied binary DPPC:POPC liposomes at different molar ratios which were mixed before preparing the liposomes (in the following called pre-mixed liposomes, see Figure 4.19a). Second, we mixed pure POPC liposomes with pure DPPC liposomes (in the following called mixed liposomes, see Figure 4.19b) at different DPPC:POPC ratios and measured the corresponding Hyper-CEST effect and the depolarization times. All the experiments presented in this section were performed with a concentration of 5 µM CrA and 200 µM lipids.

In the second part of this section POPC:cholesterol mixtures were studied. The measurements revealed that the depolarization time depends linearly on the cholesterol content in POPC:cholesterol model biomembranes and therefore allows its quantification.

4.2.1 Lipid rafts

Binary DPPC:POPC liposomes

Hyper-CEST spectra: Figure 4.20a shows the Hyper-CEST response of CrA when interacting with pre-mixed DPPC:POPC model biomembranes, with different DPPC:POPC ratios at 297 K. As in the previous sections, the two characteristic resonances of Xe@CrA_{aq} (at 62 ppm) and Xe@CrA_{lip} (at 73 ppm) are visible. The slightly different chemical shifts compared to the ones in Figure 4.13 can be explained by the slightly elevated temperature (by 4 K). The Xe@CrA_{aq} resonance remains unchanged when changing the lipid composition, similar to the spectra that were performed with different lipid concentrations (see also Figure 4.13). The slightly lower M_z/M_{z0} at a low DPPC content arises from the spillover of the Xe@CrA_{lip} resonance.

In contrast to the Xe@CrA_{aq} resonance, the Xe@CrA_{lip} resonance at 73 ppm was affected when changing the DPPC:POPC ratio. When the biomembrane was in the

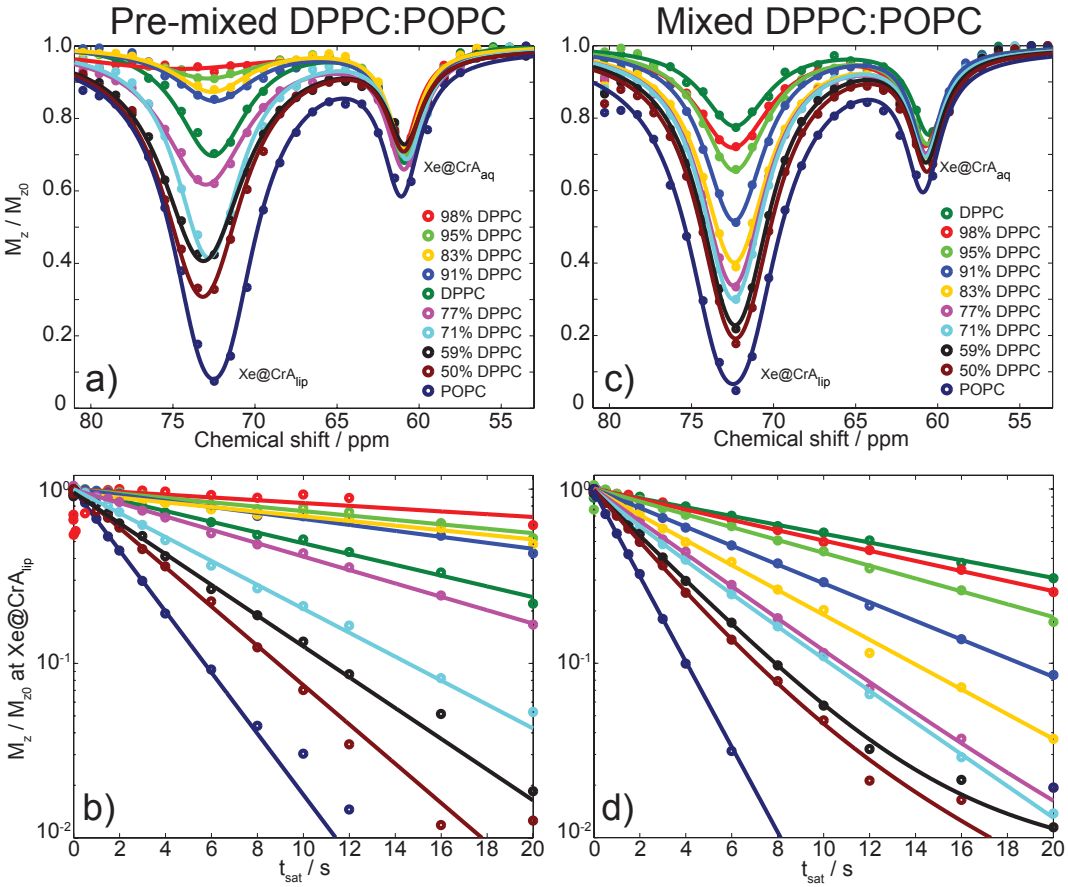

Figure 4.20 – Hyper-CEST spectra of 5 µM CrA in the presence of 200 µM pre-mixed (a) and pure mixed (c) DPPC:POPC model biomembranes with variable DPPC:POPC concentration ratios at 297 K. The fits were performed using equation 3.5. The corresponding depolarization processes of the $Xe@CrA_{lip}$ resonance at 73 ppm are shown in (b) and (d). The fits were obtained using DeLTA. The first five data points of the 98 % DPPC data set in (b) were not used in the DeLTA. Reproduced from reference [47]. Copyright © 2014 Elsevier Inc.

S_o phase, at 100 % DPPC, the Hyper-CEST effect M_z/M_{z0} was more efficient than for a DPPC concentration of 98, 95, 91 and 83 %, which yielded the weakest Hyper-CEST responses. Decreasing the DPPC concentrations below 77 % resulted into a monotonically improving Hyper-CEST effect. The remarkably weak Hyper-CEST effects for DPPC concentrations between 83 – 98 % might origin from the coexistence of the S_o and L_d phase that possessed fluctuating domain size as observed in the same model biomembranes by Svetlovics *et al.* [135]. We hypothesize that these fluctuations disturb Xe exchange in and out of CrA compared to conditions in pure DPPC liposomes.

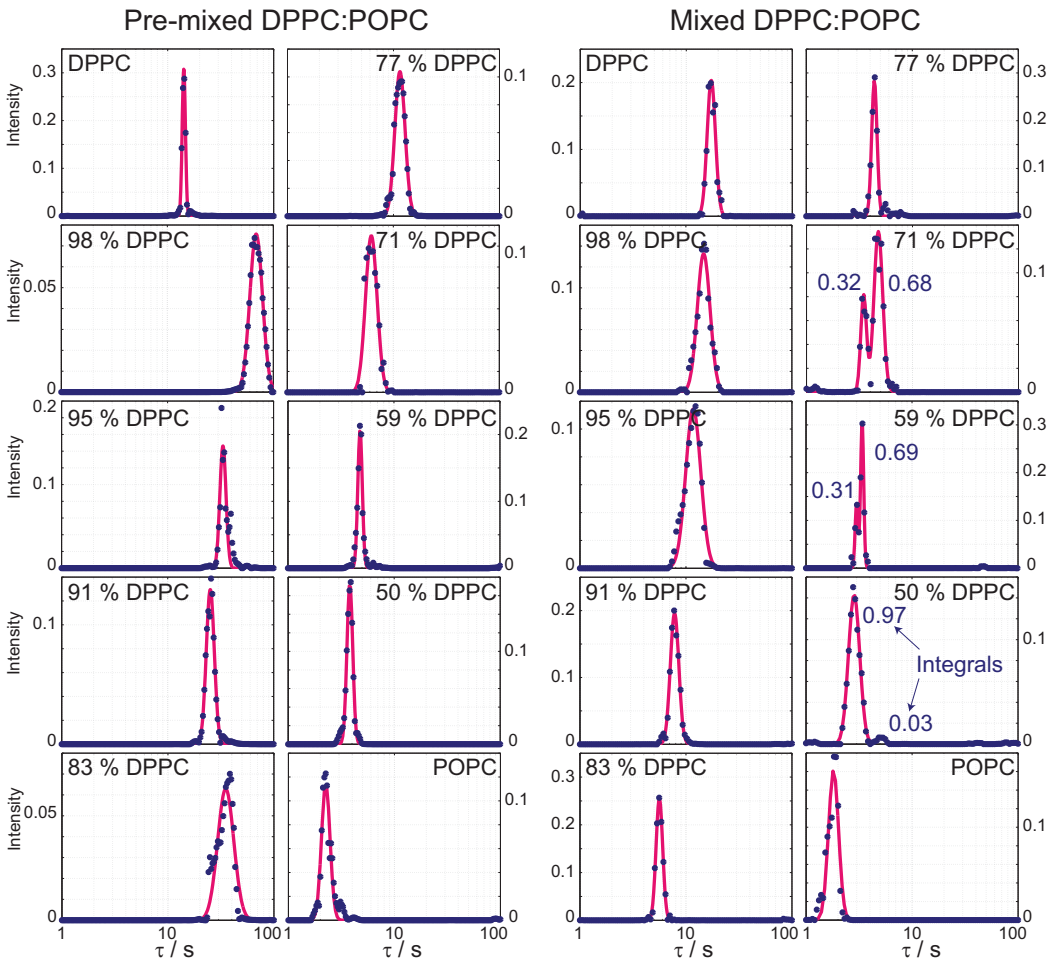

Figure 4.21 – Depolarization time distributions of the depolarization processes shown in Figure 4.20b and d. Mono-exponential depolarization processes were found except for DPPC concentrations of 71, 59 and 50 % in the mixtures of pure DPPC and pure POPC liposomes (mixed DPPC:POPC). Reproduced from reference [47]. Copyright © 2014 Elsevier Inc.

DeLTA: Analyzing the depolarization processes as shown in Figure 4.20b using DeLTA yielded a single depolarization time for each DPPC:POPC ratio. The depolarization time distributions are shown in Figure 4.21 in the two columns to the left. At a concentration of 100 % DPPC the depolarization time $\tau = (14.2 \pm 0.7)$ s was up to a factor 4.8 faster than the depolarization times in model biomembranes that contained a small amount of POPC (98, 95, 91 and 83 % DPPC), e.g. $\tau = (69.1 \pm 2.7)$ s at 98 % (see also Figure 4.22). Again we attribute this drastic increase in depolarization time to the fluctuations in domain size of the lipid rafts. The fluctuations might influence the Xe diffusion and exchange in and out of CrA such that it results into a less efficient Hyper-CEST effect.

The depolarization became significantly faster when the DPPC amount was smaller than 77 %. The fastest depolarization time $\tau = (2.3 \pm 0.1)$ s was found for pure POPC.

The ratio of $\tau_{\mathrm{DPPC}}/\tau_{\mathrm{POPC}} \approx 6$ is in very good agreement with the experiments presented in section 4.1.2 ($\tau_{\mathrm{DPPC}}/\tau_{\mathrm{POPC}} \approx 7$ for 200 µM of lipids and 5 µM of CrA at 303 K) and section 4.1.3 ($\tau_{\mathrm{DPPC}}/\tau_{\mathrm{POPC}} \approx 7$ for 1 mM of lipids and $\tau_{\mathrm{DPPC}}/\tau_{\mathrm{POPC}} \approx 10$ for 100 µM of lipids, both with 5 µM CrA at 293 K), even though the absolute depolarization times were different which we attribute to the different temperatures.

At 77 % DPPC, and hence only 13 % POPC, the depolarization time $\tau \leq (6.1 \pm 0.4)$ s was already quite fast and did not change that much to $\tau = (2.3 \pm 0.1)$ s for pure POPC. We assume that below 77 % DPPC stable domains of POPC in the L_d phase had been formed which were dominating the depolarization process and made the remaining, yet large, DPPC contribution negligible. This means that small amounts of POPC can overcome the depolarization of Xe atoms that are interacting with DPPC domains. This domination might be explained by a faster exchange rate of Xe atoms in and out of the L_d domains.

Beside the unusually high depolarization times at high DPPC concentrations (except for 100 %), it is interesting that mono-exponential decays were found when analyzing the depolarization data. That is surprising, because the lipid rafts with either the S_o or L_d phase should coexist in this regime [134]. An explanation could be that the timescale of the saturation pulse (in the order of seconds) is much longer than the time it takes for the Xe atoms and CrA molecules to diffuse in between the S_o and L_d domains. Therefore no biexponential depolarization process, that represents the two coexisting phases, could be detected. Unfortunately, the diffusion constants of neither Xe nor CrA have yet been measured in lipid bilayers, in particular not in DPPC:POPC model biomembranes.

Mixtures of pure DPPC and POPC liposomes

In liposomes that consist of only a single type of phospholipid lipid rafts cannot establish. They can either be in the S_o or L_d phase. At 297 K pure DPPC or POPC liposomes are far from the $S_o \rightarrow L_d$ phase transition which occurs at 314 K for DPPC and 271 K for POPC. As a control experiment for the domain formation with size-fluctuations detected in the pre-mixed liposomes in section 4.2.1, we again mixed solutions of DPPC and POPC at the same different molar ratios, but this time with pure liposomes that should not fuse. With that we can also check if the Hyper-CEST technique is able to sense two different lipids in a solution simultaneously.

Hyper-CEST spectra: The Xe@$\mathrm{CrA_{aq}}$ resonances for different ratios of DPPC and POPC liposomes at 62 ppm in Figure 4.20c again look very similar in all spectra as in the case of pre-mixed liposomes (Figure 4.20a), including the spillover of the broad Xe@$\mathrm{CrA_{lip}}$ resonance that affected the Xe@$\mathrm{CrA_{aq}}$ resonance at low DPPC concentrations. However, this time the order of intensities of the Xe@$\mathrm{CrA_{lip}}$ resonances

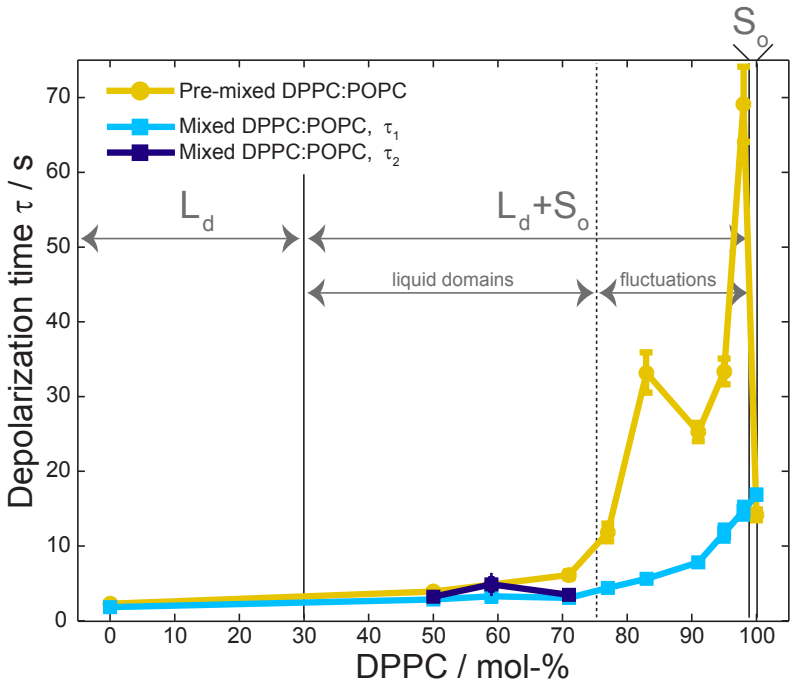

Figure 4.22 – Depolarization times τ obtained from the inverse Laplace transforms shown in Figure 4.21. The error bars represent the width of the maxima in the depolarization time distributions. The three phases L_d, $L_d + S_o$ and S_o in pre-mixed liposomes from reference [134] (see also Figure 3.14) are separated by the two solid vertical lines. The ranges where liquid domains and domains of fluctuating cluster size in the pre-mixed liposomes are assumed [135] are separated with the dashed vertical line. Two depolarization times τ_1 and τ_2 were found for mixed liposomes at DPPC concentrations of 50 %, 59 % and 71 % (represented in dark and light blue). Reproduced from reference [47]. Copyright © 2014 Elsevier Inc.

was different compared to the resonances of pre-mixed liposomes: M_z/M_{z0} decreased monotonically with decreasing DPPC content. Together with the results from the pre-mixed liposomes, this indicates, that no phase transition was detected.

DeLTA: Figure 4.20d shows the depolarization processes of the Xe@CrA$_{\text{lip}}$ resonances in the case of pure DPPC and POPC liposomes. The corresponding depolarization times distributions are shown in Figure 4.21 in the two columns to the right. This time there was no drastic increase in depolarization time detected, as shown in Figure 4.22. Because of this monotonicity we assume that the different liposomes did not fuse (which might be caused by the bubbling of the gas mixture into the solution) and, as expected, no phase transition with possible domain size fluctuations was detected.

Interestingly, for high DPPC contents ($\geq$ 77 %) the inverse Laplace transform yielded only one depolarization time τ, whereas with further decreasing DPPC content (71 %, 59 %, 50 %) DeLTA yielded a second τ-component (represented in light blue

and dark blue in Figure 4.22). Such a bi-exponential result agrees with the results presented in section 4.1.2, when pure DPPC and pure POPC liposomes were spatially separated in the two nested NMR tubes. However, this time the slower depolarization time that we attribute to the interaction with DPPC was not slower by a factor of 7. This might be explained by the absence of a physical separation in between the different types of liposomes which causes interference of the depolarization processes in DPPC and POPC. For example a Xe atom might travel from a DPPC liposome to a POPC liposome during a saturation pulse. This might also explain why only a single, intermediate depolarization time is detected over a large range which was closer to the faster depolarization process caused by POPC. Yet, when two depolarization times were found (Figure 4.21), the intensities of the two peaks were similar to the DPPC:POPC ratio, except for the case with 50 % DPPC.

To be able to interpret the data more quantitatively in terms of partitioning and Xe exchange in the different liposomes one has to do quantitative modeling of the data. This would require many more measurements as each Hyper-CEST spectra has to be recorded at different B_1 values [79]. By extending the maximal saturation time up to a few τ_{DPPC} one might resolve the DPPC related depolarization better and with more accuracy when it has to compete with the faster τ_{POPC} without a physical separation.

4.2.2 Impact of cholesterol content on Xe depolarization

Hyper-CEST spectra and DeLTA

When cholesterol is incorporated into pure POPC bilayers the ordering of the acyl chains gets increased [124] and the L_o phase is established (see section 3.3.2). Because Hyper-CEST is sensitive to changes in membrane fluidity as demonstrated in the previous sections it should also be possible to sense the influence of cholesterol on membrane fluidity. Therefore, we prepared POPC:cholesterol bilayers, where the cholesterol content was varied in the biologically relevant range of 0 – 50 %.

Figure 4.23 shows the dependence of the Xe@$\mathrm{CrA_{lip}}$ resonance on the cholesterol content at 310 K. The Xe@$\mathrm{CrA_{lip}}$ resonance clearly became weaker with increasing cholesterol content which indicates the establishing of a more ordered membrane structure that hampers Xe exchange in and out of the membrane as well as in and out of the membrane-embedded CrA molecules.

The Xe@$\mathrm{CrA_{aq}}$ resonance was much more pronounced than the Xe@$\mathrm{CrA_{lip}}$ resonance and even completely saturated in all Hyper-CEST spectra with the saturation power and saturation time used. This must be due to the elevated temperature as a similar behavior was found when increasing the temperature and detecting the CrA-dye conjugates in the presence of lipids (section 4.1.1). However, the resonance's right shoulder did not change with changing the cholesterol level as much as the Xe@$\mathrm{CrA_{lip}}$ resonance from which we conclude that the Xe@$\mathrm{CrA_{aq}}$ resonance did not change significantly.

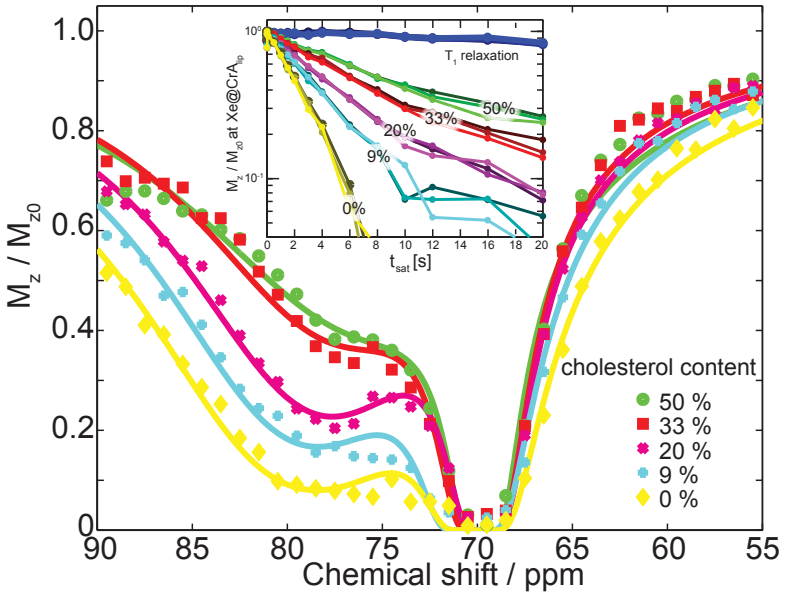

Figure 4.23 – Hyper-CEST spectra of POPC:cholesterol liposomes at 310 K. The cholesterol level is given in %. The inset shows the corresponding depolarization processes recorded at the Xe@CrA_{lip} resonance at 77 ppm. For each cholesterol concentration 3 independent measurements were performed. The T_1 relaxation was obtained by applying off-resonant saturation pulses at 313 ppm. Reproduced from reference [47]. Copyright © 2014 Elsevier Inc.

The broad overlap of the two resonances was due to the fast exchange of Xe atoms at 310 K [21, 46, 75]. This effect is also consistent with the smaller chemical shift difference of the two resonances that was caused by an increased temperature as demonstrated in section 4.1.1. Compared to the Hyper-CEST spectra in Figure 4.20, which were acquired at 297 K, the Xe@CrA_{aq} resonance was shifted from 62 to 70 ppm whereas the Xe@CrA_{lip} was shifted from 74 to 77 ppm.

In addition to the acquisition of the Hyper-CEST spectra we also applied saturation pulses of different lengths to the Xe@CrA_{lip} resonance and performed DeLTA. The results are shown in the inset in Figure 4.23. The accuracy and reproducibility of the method was demonstrated by repeating each measurement three times. DeLTA yielded a single peak in the depolarization time distributions. Figure 4.24a shows the obtained depolarization times in dependence of the cholesterol content. The depolarization times increased from (2.4 ± 0.2) s for pure POPC to (8.9 ± 0.3) s for 50 % cholesterol. The depolarization time seems to depend linearly on the cholesterol content. It should be possible to discriminate the amount of cholesterol in POPC liposomes with an accuracy of at least 5 % when taking the error bars that represent the standard deviation of the three measurements, into account.

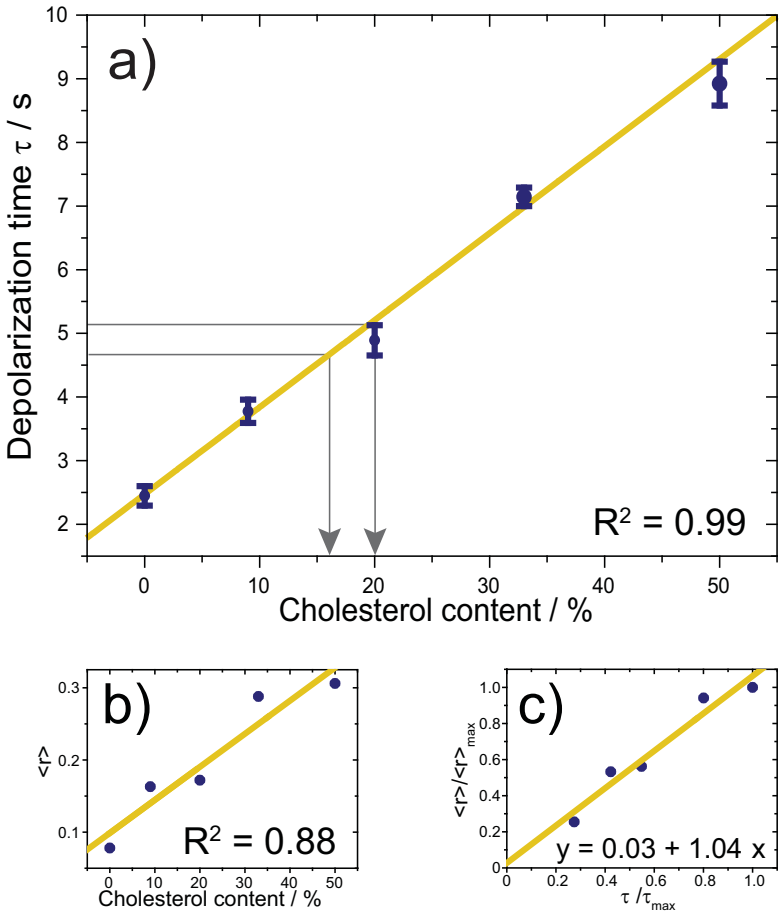

Figure 4.24 – (a) Depolarization times of the depolarization processes for the POPC:cholesterol liposomes shown in Figure 4.23. The depolarization time appears to depend linearly on the cholesterol level in the measured range. The error bars allow to determine the cholesterol content with an accuracy better than 5 % (gray arrows). (b) shows the fluorescence anisotropy measurements on the same POPC:cholesterol model biomembranes and the linear fit. (c) compares the Hyper-CEST method with the fluorescence anisotropy method (both normalized to their maximum) yielding a linear dependence of $y = (0.03 \pm 0.09) + (1.04 \pm 0.14)x$. Reproduced from reference [47]. Copyright © 2014 Elsevier Inc.

Fluorescence anisotropy control experiments

Usually the cholesterol content in model biomembranes is studied by steady-state fluorescence approaches, which are sensitive to the packing of the acyl chains of phospholipids and the presence of cholesterol. One approach is fluorescence anisotropy ($\langle r \rangle$) which uses 1,6-diphenyl-1,3,5-hexatriene (DPH) as a fluorescent probe [167]. The higher the fluidity of a membrane the higher the rotational diffusion rate of the DPH that is embedded into the membrane, which exhibits a faster decay of $\langle r \rangle$.

To validate the correct incorporation of cholesterol into the POPC bilayers we measured the fluorescent decay of DPH in the different POPC:cholesterol model biomembranes. Figure 4.24b shows the recorded fluorescence anisotropy $\langle r \rangle$ of the different POPC:cholesterol liposomes. Both the depolarization times and $\langle r \rangle$ appear to increase linearly with increasing cholesterol content. The linear increase of the fluorescent decay time of DPH in the presence of cholesterol is qualitatively in very good agreement to what has been measured at 296 K in reference [168], where DPH was used as well or at 313 K in reference [126], where *trans*-parinaric acid was used as a fluorescent probe. However, the noise of the Hyper-CEST data (adjusted $R^2 = 0.99$) is smaller compared to our measurements of $\langle r \rangle$ (adjusted $R^2 = 0.88$). Figure 4.24c compares the sensitivities of both methods. The linear fit yields for the y-axis intercept 0.03 ± 0.09 and 1.04 ± 0.14 for the slope. The slope (≈ 1) illustrates that the two methods possess similar sensitivities by covering a similar dynamical range.

4.2.3 Summary

Hyper-CEST and DeLTA can be used not only to sense the presence of lipid environment, the highly sensitive detection techniques can also be used to study biophysical properties of model biomembranes. The performed experiments showed, that it is possible to discriminate different composed model membranes, especially when domains of fluctuating sizes are present as proposed in the literature [135], which caused a drastic increase in depolarization time. Also the presence of cholesterol in lipid bilayers caused an increased depolarization time which could be sensed with an accuracy of 5 %.

However, we currently do not believe that it is possible to use the presented approaches to study real biomembranes from cells, as they are much more diverse. For example, the breast cancer cell line MCF7, which should have a much higher cholesterol content in its membrane, did not show the same trend as seen in the model membranes with Hyper-CEST, when we compared it to the non-tumorgenic epithelial cells MCF10A (Figure 4.25). We believe that the higher metabolic turnover of the breast cancer cell line caused a higher CrA cellular uptake than in the control cell line, which masks the impact of cholesterol on membrane fluidity.

Yet, using Hyper-CEST to study biophysical properties of biomembranes can provide complementary information to established methods. For example, an advantage of the Hyper-CEST approach is that no elaborate modification of the original membrane is required as it is the case for example in ^{13}C NMR spectroscopy, where the lipids have to be labeled isotopically.

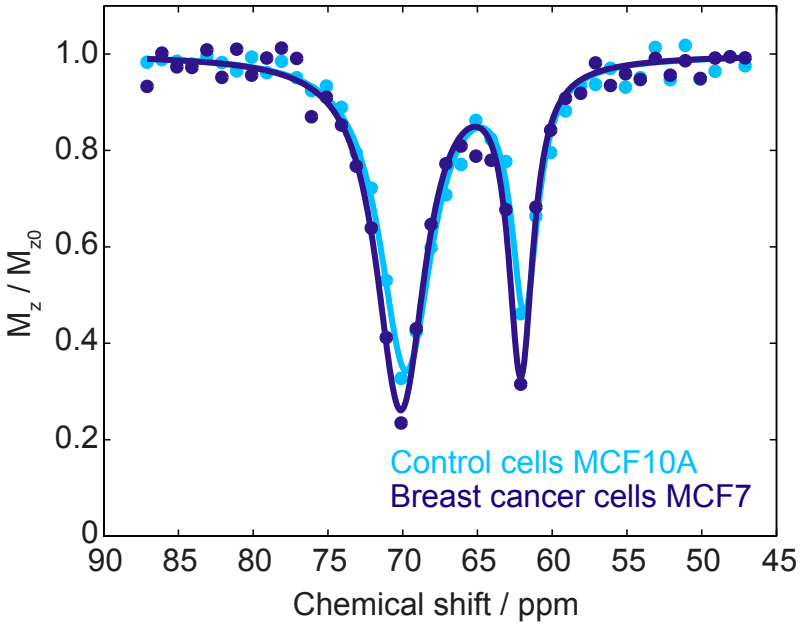

Figure 4.25 – Comparison of the Hyper-CEST effect of 5 µM CrA in cholesterol-rich human breast cancer cells and nontumorgenic epithelial cells MCF10A at 310 K. The Xe@CrA_{aq} resonance is at 62 ppm. The Xe@CrA_{lip} is at 70 ppm. Parameters: 7×10^6 cells/mL; CrA was added 60 min before the experiments. Saturation parameters: $B_1 = 3$ µT, $t_{sat} = 4$ s.

4.3 Sensing antimicrobial peptide action on biomembranes

Antimicrobial peptides (AMPs) can exhibit antibiotic, virucidal, funigicidal, hemolytic and tumoricidal activity by interacting with cellular membranes [169]. They are produced by various organisms, e.g. humans, fungi, amphibians or insects, basically to defend the organisms in the first line against bacterial infections, even before T and B cell defense action. Because of that they are not only used naturally by the organisms, they also play a crucial role in drug research as they do not show cytotoxic effects against healthy eukaryotic cells (at meaningful concentrations) [170]. Most AMPs consist of a short amino acid sequence (12 – 50 units, weight $<$ 10 kDa) and are therefore easy to synthesize.

4.3.1 Classes of antimicrobial peptides

With a mainly hydrophobic or amphiphilic amino acid sequence, AMPs attack bacterial cells by inducing pore formation in their characteristically charged cellular membrane. The pores allow ions and other small molecules to pass the cellular membrane which causes swelling of the cells and osmolysis followed by cell death. Because of different mechanisms in pore formation, the AMPs can basically be divided into three classes.

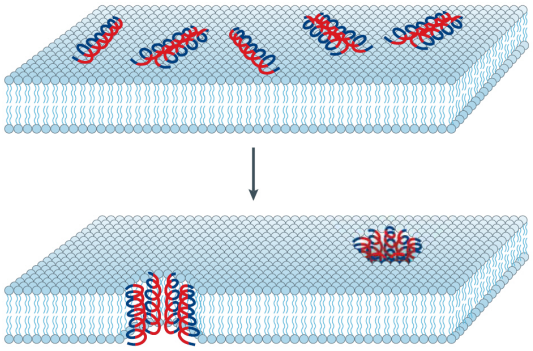

Figure 4.26 – Scheme of formation of barrel-stave pores by AMPs. The to the membrane attracted and attached AMPs aggregate and form stable pores by aligning their hydrophobic regions (blue) towards the lipid bilayer and the hydrophilic regions (red) towards the formed pore interior. Reproduced from reference [175]. Copyright © 2005 Macmillan Publishers Limited.

The principle of the three classes are sketched in Figure 4.26, 4.27 and 4.28. The classes are termed barrel-stave, carpet, and toroidal class due to the characteristic way of membrane interaction. The three classes have in common that at a low AMP/lipid ratio the AMPs are attached parallel to the lipid bilayer [171]. With increasing AMP/lipid ratio the AMPs orient perpendicular to the lipid bilayer and insert into it to form transmembrane pores which can be different for different AMPs.

Barrel-stave class: The peptides of the barrel-stave class form groups of helices that arrange in such a way that they span the lipid bilayer and act as the staves of a barrel through which ions or small molecules can pass [172, 173]. The AMP alamethicin is a well-studied representative of the barrel stave class. It is produced by the *Fungus Trichoderma Viride* with the amino acid sequence Acetyl-UPUAUAQUVUGLUPVUUQQ-Phenylalaniol (U stands for α-aminoisobutyric acid), where the hydrophobic regions of the sequence face the lipids and the hydrophilic regions form the water-filled channel that spans the lipid bilayer [171]. One barrel-stave pore produced by alamethicin usually is made up of 8 helices [171], but this number can change depending on the lipid composition [174].

Carpet class: Characteristic for the carpet class is the accumulation of a high number of AMP molecules that span the surface of the lipid bilayer in a carpet-like manner [176]. The AMPs are mainly attracted to the lipid bilayer by electrostatic interactions. Once their concentration is high enough they disrupt the lipid bilayer like a detergent and start to form transient pores which increases the total membrane surface so that additional AMPs can attach to the surface. Well-studied representatives of the carpet model are dermaseptin S from the frog *Phyllomedusa* with a lysine-rich but varying sequence [177] and cecropin which can be found in the moth *Hyalophora cecropia* and consists of 31 – 37 amino acids [178].

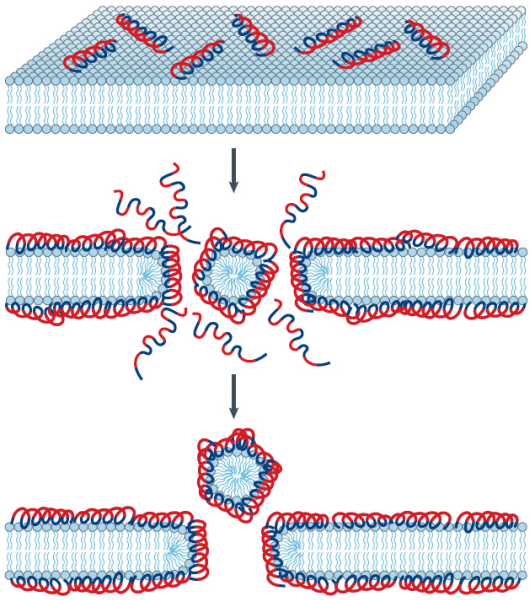

Figure 4.27 – Scheme of the AMP carpet model. The AMPs orient parallel to the lipid bilayer surface and span it by forming a carpet-like structure. The hydrophobic regions (blue) are facing the lipid bilayer surface whereas the hydrophilic regions are facing the surrounding aqueous medium. Reproduced from reference [175]. Copyright © 2005 Macmillan Publishers Limited.

Toroidal class: The last class, the toroidal class, is defined by transmembrane pores in which the lipid bilayer is bent with a very high curvature and the produced water channel is made up of both, phospholipids and AMP molecules that alternate [171]. The AMPs of the toroidal class tend to align with the head groups of the lipids, which causes the toroidal-like bending of the lipid bilayer and the alternating AMP-lipid wall of the pore. The AMPs melittin (main component of the honey bee venom, amino acid sequence GIGAVLKVLTTGLPALISWIKRKRQQ-NH_2), magainin (from the frog *Xenopus laevis*), piscidin (found in several fish) are well-studied representatives of the toroidal class. Although melittin is one of the most studied AMPs, it is not totally clear if it can be classified into the toroidal class, the barrel-stave class or a mixture of both [171]. However, most of the studies classify melittin as a toroidal pore AMP.

4.3.2 Techniques to study antimicrobial peptide action

Various techniques, which are briefly described in the following, are used to study the different interactions of AMPs with cellular membranes. One technique alone cannot provide full understanding of the interaction mechanism of an AMP, only the combination of complementary techniques is able to characterize and understand the mechanisms of the models as described above. The review article by Kim A. Brogden [175] nicely summarizes and describes the different techniques and their applications.

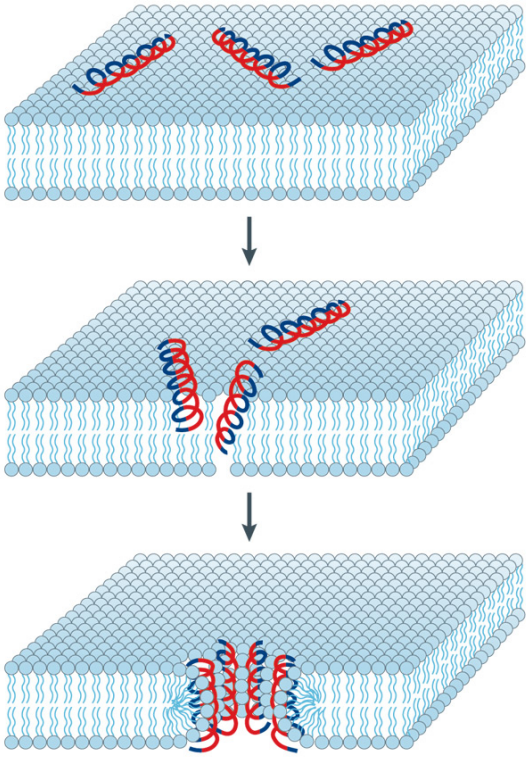

Figure 4.28 – Scheme of AMP toroidal pore formation. The AMPs aggregate and get inserted into the lipid bilayer. They induce a high curvature in the lipid monolayers which bend. The build pores are made up of both, the phospholipids and the AMPs. Reproduced from reference [175]. Copyright © 2005 Macmillan Publishers Limited.

Microscopy techniques can be used to visualize the general effects of AMP action, such as cell death, or to identify general target sites. The methods comprise optical confocal laser-scanning microscopy, transmission and scanning electron microscopy. The microscopy techniques helped to understand that different AMPs have different target sites, as for example shown in reference [179], where the actions of the AMPS SMAP29 and CAP18 on bacterial cells are compared. Furthermore, the study revealed, that the bacterial cells were killed after 15 min upon incubation with the AMPs, however, the peptides could be detected inside the cells almost immediately after incubation. Hence, to obtain a more detailed picture of the AMP interaction with cellular membranes further methods are required.

Much more simplified experiments can be performed when taking advantage of model membranes. They allow to study the AMP interaction with different phospholipids in detail such as their secondary structure, attachment, incorporation and orientation on the membrane. Techniques that are used in combination with model membranes are NMR spectroscopy, X-ray crystallography, neutron diffraction

and several optical spectroscopy techniques such as fluorescence, Fourier transform infrared, Raman or oriented circular dichroism.

For example, from solid and liquid state NMR spectroscopy measurements, information about the secondary structure, orientation and penetration into the lipid bilayer of model membranes can be obtained [169, 180]. Neutron in-plane and off-plane scattering could reveal differences in pore size induced by alamethicin and magainin [172, 181]. Fluorescent dyes, which are encapsulated in model membrane vesicles, enable for example to study their time-dependent release out of the vesicles upon the action of AMPs at different concentrations and membrane compositions [182–185], whereas with differently sized fluorescent dyes pore sizes can be estimated [186]. In contrast to vesicles, with planar model membranes ion channel formation can be studied by monitoring the voltage dependent electric currents over a lipid bilayer that are produced by ion fluxes upon pore formation [187].

With these existing methods it could be shown, that already at very low AMP concentrations, transient pores are formed by fluctuations, which cause ion conduction but not leakage of larger molecules over the cellular membrane [188]. Stable pores are formed beyond an AMP and a membrane specific threshold that also enable larger molecules to enter or leave the attacked cells [185].

4.3.3 Hyper-CEST experiments

As demonstrated in the previous sections, Hyper-CEST is sensitive to changes in membrane fluidity. We hypothesized that it also allows to distinguish the different mechanisms of pore formation caused by different AMPs. For initial experiments we chose melittin and alamethicin as AMPs and studied their action on prepared model membranes of either mixtures of POPC and 1-palmitoyl-2-oleoyl-*sn*-glycero-3-phospho-(1'-rac-glycerol) (POPG) at a POPC:POPG molar ratio of 3:1 or only POPC, representing prokaryotic or eukaryotic cell membranes, respectively. Before the measurements the model membranes (with a lipid concentration of 200 µM) were incubated with different concentrations of the AMPs at a fixed CrA concentration of 5 µM (used as the Hyper-CEST sensor) in 1.5 mL PBS at 300 K. A Hyper-CEST spectrum around the CrA_{lip} resonance was recorded to get the resonance's exact chemical shift upon which the depolarization process was measured.

Figure 4.29 shows the depolarization times in POPC and POPC:POPG model membranes in the presence of different concentrations of melittin and alamethicin.

Melittin The depolarization time in POPC model membranes dropped from ca. 1.7 s to ca. 1.2 s once the melittin:POPC ratio was larger than 0.1. A similar, but much more pronounced drop in depolarization time was induced by melittin in POPC:POPG mixtures at a approximately 10 times lower melittin:lipid ratio. We explain the drop in depolarization time with the formation of stable toroidal pores accompanied with large curvature of the lipid bilayer induced by melittin. The locally high curvature might have facilitated the traveling of Xe atoms in and out of

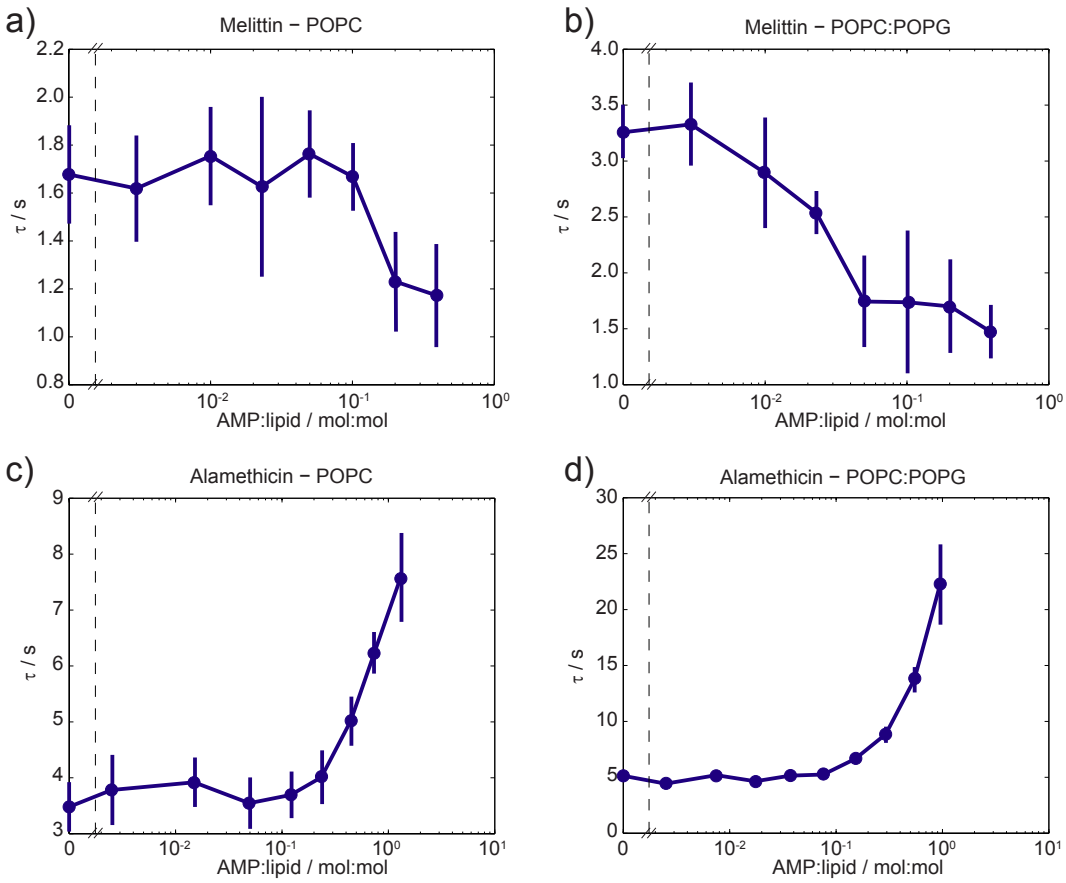

Figure 4.29 – Depolarization times of Xe@CrA in the presence of 5 µM CrA in 200 µM POPC and POPC:POPG (3:1 mol/mol) in dependence of the concentration of melittin (a, b) and alamethicin (c, d) in PBS at 300 K. Errorbars represent the uncertainty of the DeLTA result. Saturation pulse: $B_1 = 6$ µT.

the membrane which yielded the faster depolarization times. The higher affinity of melittin for prokaryotic membranes can explain the 10 times lower AMP:lipid ratio, where the drop in depolarization time occurs.

Also at a melittin:lipid ratio of ca. 0.01 Lee *et al.* [185] found a significant change in membrane thickness and orientation of the melittin helices measured by X-ray diffraction and oriented circular dichroism spectroscopy experiments, respectively. Figure 4.30 shows the results which were performed with a similar lipid mixture (DOPC:POPG at a ratio 7:3) at almost the same temperature (298 K). The measured parameters decreased linearly with increasing melittin:lipid ratios until a melittin:lipid ratio of ca. 0.01 – 0.02 was reached. Beyond that ratio no further change in the measured parameters was detected. Lee *et al.* interpret the range of linear decrease with the formation of transient pores and the range of unchanged measurement parameters with the presence of stable pores.

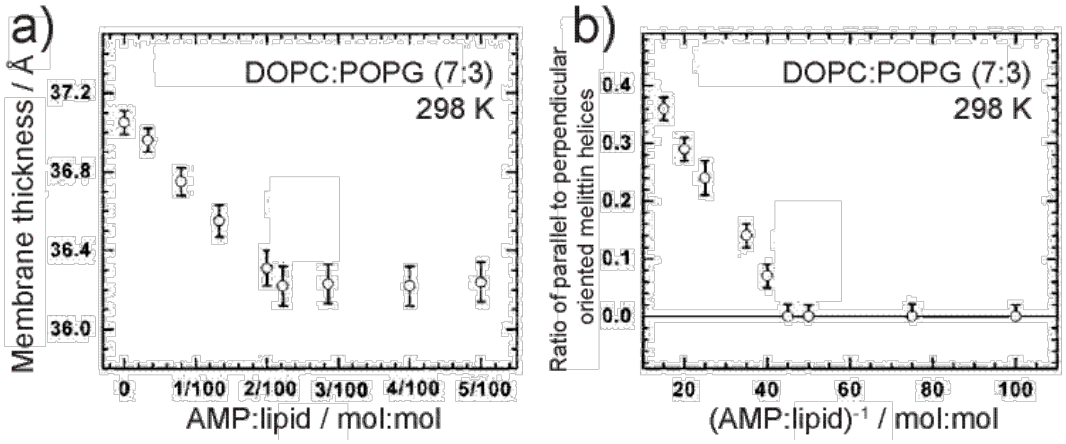

Figure 4.30 – a) DOPC:POPG membrane thickness measured by X-ray diffraction and b) the fraction of the melittin helices that are oriented perpendicular to the lipid bilayer measured by oriented circular dichroism spectroscopy. Reproduced from reference [185]. Copyright © 2013 National Academy of Sciences.

Alamethicin The situation was completely different in the presence of alamethicin. In both cases, POPC and POPC:POPG mixtures, the depolarization time increased significantly from ca. 4 s to almost 8 s in case of POPC and to ca. 23 s in case of POPC:POPG at a alamethicin:lipid ratio of 1. It is very likely that the formation of barrel-stave pores caused the increase in depolarization time as the pores could act as barriers that hindered intra-lipid diffusion of Xe atoms and CrA molecules. This concept gets supported by the continuous increase of the depolarization time with an increasing alamethicin:lipid ratio where more stable pores could be formed.

4.3.4 Summary

In initial experiments the depolarization time measurements revealed drastic differences in the action of melittin and alamethicin on POPC and POPC:POPG model membranes. The differences are most likely caused by the different pore formation mechanisms. Melittin causes a high curvature of the lipid bilayers whereas the barrel-stave pores produced by alamethicin might act as barriers and hinder Xe and CrA intra-lipid diffusion.

Although AMPs are already well explored, Hyper-CEST might be used as a complementary approach to study the action of AMPs on cellular membranes, because Hyper-CEST allows to study the AMP action in the original environment. For example to perform neutron in-plane scattering experiments, the water surrounding the model membranes has to be evaporated so that the dried lipid bilayers-AMP mixtures become oriented multilamellar layers on a flat quartz surface [189].

4.4 Liposomal Xe carriers for cell targeting

The hydrophobic character of CrA and the resulting interaction with lipid environments allows biophysical studies of biomembranes as demonstrated in the previous sections. Yet, in the context of cell experiments this hydrophobic-driven interaction was initially reported as an unwanted side-effect that can mask specific cell targeting [98]. Here we demonstrate that the hydrophobic interaction even provides possibilities in terms of a biocompatible delivery of CrA to a specific cell type. The results presented in this section are mainly based on the publication [20] (Schnurr *et al.*, Brain endothelial cell targeting via a peptide-functionalized liposomal carrier for xenon Hyper-CEST MRI, *Adv. Healthcare Mat.* 4 (1), 40 – 45, 2015).

Biocompatibility issues of CrA have to be considered in in vivo Xe-biosensor studies. CrA is hardly soluble in water and therefore has to be dissolved in a harmful solvent, e.g. DMSO, for stock solutions that are later diluted for cell incubation. The presence of a harmful solvent and the direct interaction of CrA with cells impact cell viability as seen in first cellular in vitro experiments [16, 19, 190, 191]. Figure 4.31 supports the reports about the cytotoxic effect of high concentrations of CrA on human cells. In this experiment human brain microvascular endothelial cells (HBMECs) showed a viability of only 70 % when being exposed to 100 µM CrA for 4 hours. To improve the water solubility of CrA by optimizing its chemical structure requires some noticeable synthetic effort [74, 94, 96]. However, when CrA is embedded into the lipid bilayer of a liposomal carrier the toxicity of CrA is shielded and there is no need for a harmful solvent to deliver CrA at a high concentration to cells as demonstrated in the following.

Liposomal carriers can be used to elegantly target cells by modifying their surface [137]. Therefore, any targeting or uptake mediating moieties, e.g. peptides, sugar moieties or antibodies, can easily be anchored into the carriers' lipid bilayers. Such liposomal carrier systems already proved their potential in terms of high sensitivity as a switchable contrast agent, for example in ^{1}H CEST-MRI [192, 193].

As liposomes provide space for hydrophobic compounds in their lipid bilayer and for hydrophilic compounds in their interior, they can also be used to transport more than one compound and therefore enable to deliver a therapeutic and a diagnostic agent together [193]. For cell targeting we anchored short arginine rich peptides into the liposomal surface via two covalently bound palmitoyl chains (named P2Rn) (synthesis provided by the group of Michael Beyermann (FMP, Berlin), see also [194]). Figure 4.32 shows the chemical structure of P2Rn. To have the opportunity to evaluate the cellular uptake of the carrier system by both fluorescence and Hyper-CEST carboxyfluorescein-labeled P2Rns were anchored into the liposomal carrier's lipid bilayer and loaded them with CrA.

The positive net charge at physiological pH (ca. 7.3) of the short arginine rich peptide should promote uptake into HBMECs [195, 196], which possess a highly negative charged glycocalyx and are the main component of the blood brain barrier [197]. Together with tight junctions in between the HBMECs, the glycocalyx makes

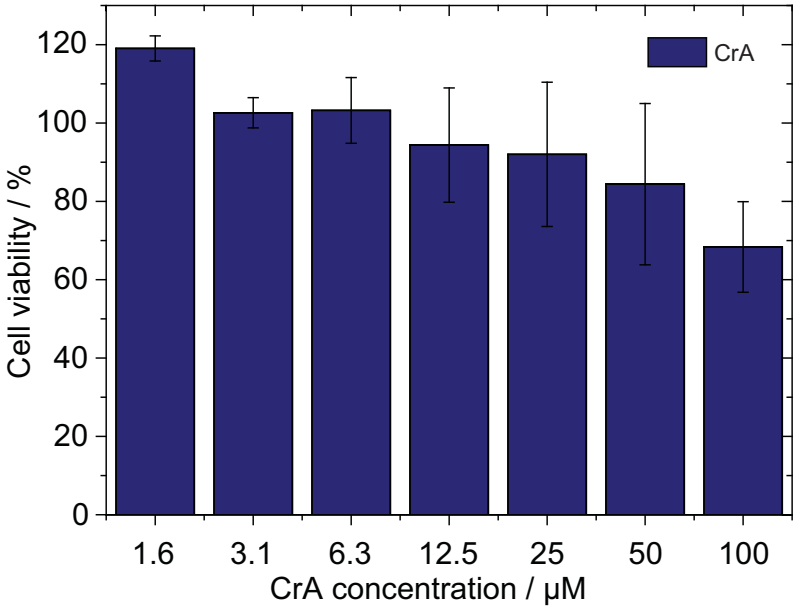

Figure 4.31 – Cell viability of human brain microvascular endothelial cells at different concentrations of CrA after 4 h incubation at 310 K. Complete viability (100 %) corresponds to cells that were not exposed to CrA.

sure that no unwanted substances can travel from the blood into the brain. To demonstrate the selectivity of the P2Rn-mediated uptake into HBMECs, we used human aortic endothelial cells (HAoECs) as a control cell line in the experiments, which have a differently sized and composed glycocalyx, which shows lower affinity for positively charged peptides such as P2Rn [198].

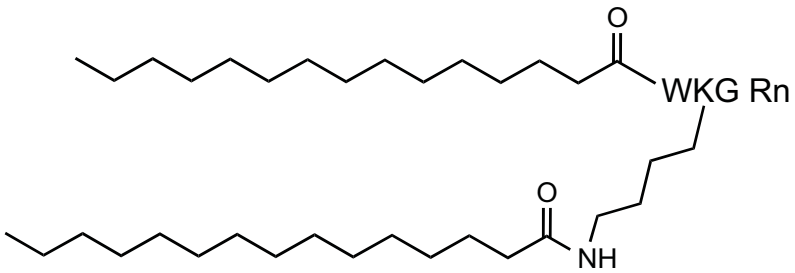

Figure 4.32 – Chemical structure of the targeting peptide P2Rn. Two palmitoyl chains are coupled to the multiple arginine sequence (Rn) by the amino acid sequence Tryptophan (W), Lysine (K) and Glycine (G).

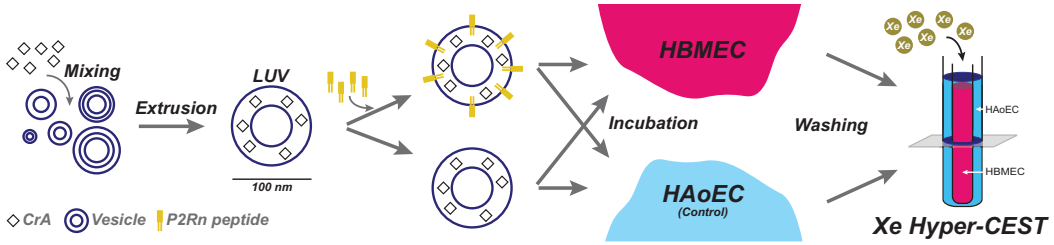

Figure 4.33 – The different steps from the preparation of the liposomal carrier for NMR (and fluorescence) experiments. Before extrusion, the vesicles were loaded with CrA in a lipid:CrA ratio of 20. The peptide P2Rn was anchored into the lipid bilayer at 310 K overnight. HBMECs and HAoECs were exposed to the prepared liposomal carriers with and without the peptide P2Rn for 4 h at 310 K. After washing and trypsination of the cells, Xe was bubbled into the cell suspension just before data acquisition. Reproduced from reference [20]. Copyright © 2015 John Wiley and Sons, Inc.

Table 4.4 – Physical characterization of CrA+LUV and CrA+LUV+P2Rn via DLS.

Carrier	Zeta potential / mV[a]	Diameter / nm[a]
CrA+LUV	-10.5 ± 2.8	116.0 ± 2.0
CrA+LUV+P2Rn	-9.0 ± 2.1	124.5 ± 3.4

[a]: mean and standard deviation of 2 independent samples with three measurements each

4.4.1 Preparation and physical characterization

Figure 4.33 illustrates the steps from the preparation of the liposomal carrier for the fluorescence and NMR experiments. The 100 nm liposomes were prepared and loaded with CrA in a lipid:CrA ratio of 20 as described in section 3.3.4. This corresponds to ca. 3800 CrA molecules per liposome. This loading with CrA did not influence the stability of the liposomes as demonstrated in section 3.3.5.

The extruded liposomes were mixed with the targeting peptide P2Rn at a lipid:peptide ratio of 1000 (ca. 80 peptides per liposome) and stored overnight at 310 K. The incorporation of the P2Rn peptides into the liposomal bilayer did not change the size distribution of the liposomes significantly as measured via DLS (Figure 4.34). Also the zeta potential, which is the electric charge difference between the dispersion medium and the shear layer of fluid that surrounds the liposome [199], did not change significantly upon anchoring P2Rn into the lipid bilayer (Table 4.4).

4.4.2 Cytotoxicity

To check the cytotoxic effect of the liposomal carrier on the target cell line, HBMEC, the cells (cultivated on a 96-well plate with a cell density of 5000 cells per well/100 µL) were exposed to 2 mL of the liposome preparation containing different concentrations of CrA for 4 h at 310 K. After that the cells were washed along with the alamarBlue assay reagent (10 µL/well) for staining of dead cells. Figure 4.35 shows the

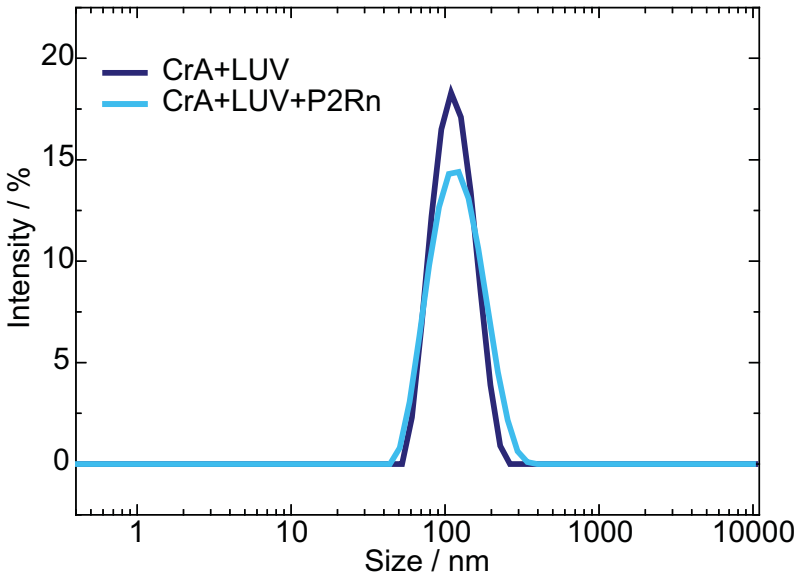

Figure 4.34 – Size distribution of CrA+LUV and after incubation with P2Rn (CrA+LUV+P2Rn) overnight at 310 K. The corresponding maximal sizes and zeta potentials are listed in Table 4.4.

fluorescence intensity at 590 nm of the samples that were incubated with either plain liposomes (LUV), liposomes loaded with CrA (CrA+LUV) and liposomes loaded with CrA and anchored peptides (CrA+LUV+P2Rn) at different concentrations of CrA. Compared to the cytotoxic effect of plain CrA, as shown in Figure 4.31, the liposomal carriers feature excellent biocompatibility, without significant decrease in cell viability with either CrA+LUV or CrA+LUV+P2Rn. Hence, the shielding effect mediated through the lipid bilayer substantially improved the cytotoxic effect of CrA. Furthermore, anchoring P2Rn into the lipid bilayer did not have a negative effect on cell viability. This is interesting because it is known that positively charged peptides alone, such as P2Rn, can mediate cell cytotoxicity [200, 201].

4.4.3 Fluorescence control experiments

Fluorescence microscopy

Qualitative information about the uptake of the liposomal carrier was performed by anchoring the carboxyfluorescein-labeled version of P2Rn (P2fRn, excitation wavelength 488 nm) into the liposomal bilayer and incorporating a rhodamine-labeled phospholipid (1,2-dipalmitoyl-*sn*-glycero-3-phosphoethanolamine-N-(lissamine rhodamine B sulfonyl) (RhPE), excitation wavelength 555 nm) into the POPC bilayer at a POPC:RhPE ratio of 100 (weight/weight). The use of the two different fluorescent molecules allowed to monitor the stability of the liposomal carrier upon cellular

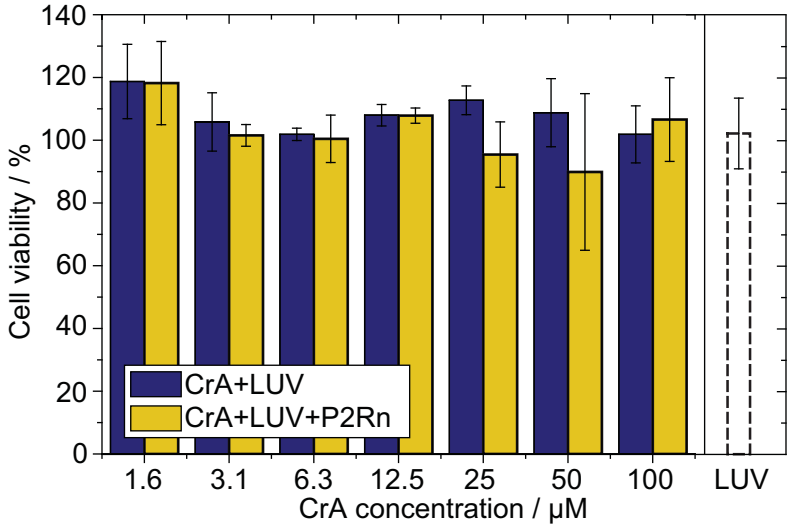

Figure 4.35 – Cytotoxicity studies of CrA+LUV and CrA+LUV+P2Rn at different concentrations of CrA and plain LUVs (separate column) on HBMECs after incubation of 4 h at 310 K measured with the alamar-Blue assay. Complete viability (100 %) corresponds to cells that were not exposed to any of the preparations. Reproduced from reference [20]. Copyright © 2015 John Wiley and Sons, Inc.

internalization and additionally to evaluate the fate of the liposomal lipid bilayer and the peptide independently.

The fluorescence microscopy experiments (Figure 4.36) confirmed that the labeled carrier CrA+LUV+P2Rn got taken up by the HBMECs. The intracellular co-localization of P2fRn and RhPE points to intact liposomal carriers after 4 h of incubation at 310 K. Furthermore, the dotted fluorescence, which agrees with cellular distribution patterns of other arginine-rich peptide-labeled liposomal carriers [200], suggests that the liposomal carriers accumulated in distinct cellular compartments, which might be lysosomes.

Flow cytometry

Quantitative information about the uptake of CrA+LUV+P2Rn was obtained by using flow cytometry analysis. Figure 4.37 shows the geometric mean fluorescence intensity of RhPE from the liposomal carrier to which the HBMECs and the control cell line (HAoEC) were exposed to for 4 h at 310 K at a carrier concentration of 13.3 nM. The flow cytometry analysis revealed the specificity of CrA+LUV+P2Rn for the HBMECs, which showed a significantly higher uptake of CrA+LUV+P2Rn over the HAoECs. Additionally, the analysis showed a significantly improved selectivity over other reported arginine-rich peptide-labeled carriers [200, 202]. Compared to the system without the targeting peptides P2Rn (CrA+LUV), anchoring P2Rn into the liposomal bilayer yielded a 7.4 fold increased uptake in HBMECs. Furthermore,

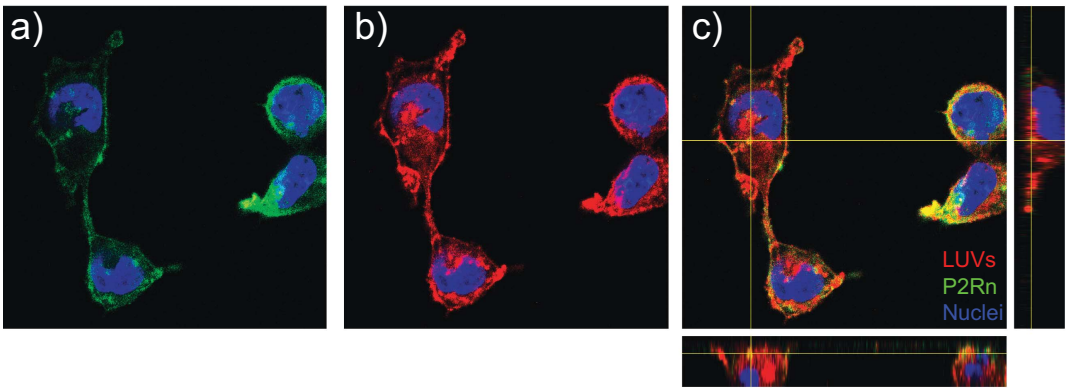

Figure 4.36 – Confocal laser scanning microscopy of HBMECs incubated with CrA+LUV+P2Rn for 4 h at 310 K with 13.3 nM of the liposomal carrier (equivalent to 50 µM CrA). The liposomal carriers were labeled with RhPE (red) (b), the peptides were labeled with carboxyfluorescein (green) (a) and the nuclei were stained with Hoechst 33342 (blue) ((a) and (b)). (c) shows all three channels plus sectional images of the perpendicular imaging planes. Reproduced from reference [20]. Copyright © 2015 John Wiley and Sons, Inc.

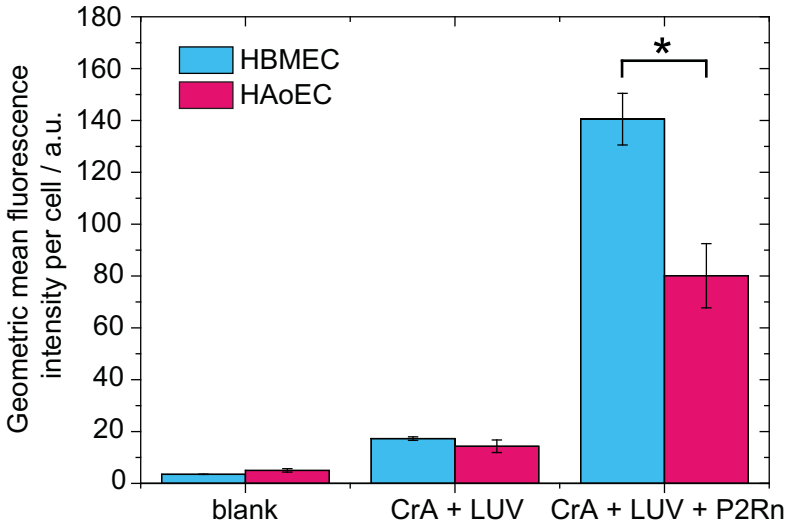

Figure 4.37 – Cellular uptake studies via flow cytometry analysis of HBMECs and HAoECs incubated with RhPE labeled CrA+LUV and CrA+LUV+P2Rn. $*p < 0.05$, Mann-Whitney U test [203]. Reproduced from reference [20]. Copyright © 2015 John Wiley and Sons, Inc.

the use of P2Rn showed much higher specificity for HBMECs than for the control HAoECs.

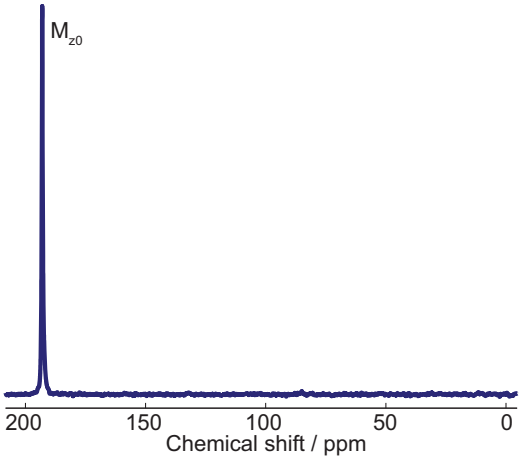

Figure 4.38 – Conventional ^{129}Xe NMR spectrum of 2.5×10^6 HBMECs at 310 K exposed to CrA+LUV+P2Rn (13.3 nM LUV concentration, equivalent to 50 µM CrA) for 4 h at 310 K. Number of averages NS = 4; gas mixture: 5 % Xe, 10 % N2, 85 % He. Except for the dissolved Xe signal all other resonances are masked by the noise. Reproduced from reference [20]. Copyright © 2015 John Wiley and Sons, Inc.

4.4.4 Hyper-CEST experiments

Spectroscopy response from liposomal carriers

The incorporation of CrA into the lipid bilayer of the carriers also allowed to perform Hyper-CEST spectroscopy. The cellular uptake of the liposomal carrier into HBMECs, that was observed with fluorescent techniques in section 4.4.3, was found in qualitative similar way using Hyper-CEST but not in conventional ^{129}Xe NMR spectroscopy as demonstrated in Figure 4.38. Conventional ^{129}Xe NMR spectroscopy was not sensitive enough to detect the small amount of CrA that got taken up by the cells, in particular at 310 K, where the resonances are broadened.

The Hyper-CEST technique allowed to detect as little as 0.5×10^6 cells/mL as shown in Figure 4.39. This cell number represents a substantial improvement in detection limit compared to former Xe NMR studies with cells [16, 19, 98]. All recorded Hyper-CEST spectra showed the two characteristic CrA resonances of Xe@CrA$_{aq}$ and Xe@CrA$_{lip}$ at ca. 62 and 71 ppm, respectively. The resonance at 62 ppm should result from CrA that got released from the cells after washing and trypsination. The larger Hyper-CEST effects in the presence of the target HBMECs compared to the control HAoECs qualitatively agrees with the flow cytometry results (Figure 4.37). The Hyper-CEST effect was the largest, when P2Rn was anchored into the liposomal carrier's bilayer and thus supports the cell specificity that is produced by P2Rn. Moreover, the specificity produced by P2Rn was significantly different ($p < 0.05$) when comparing the Hyper-CEST resonances of Xe@CrA$_{lip}$ in the presence of CrA+LUV (ca. 45 %) and CrA+LUV+P2Rn (ca. 80 %) for HBMECs. There

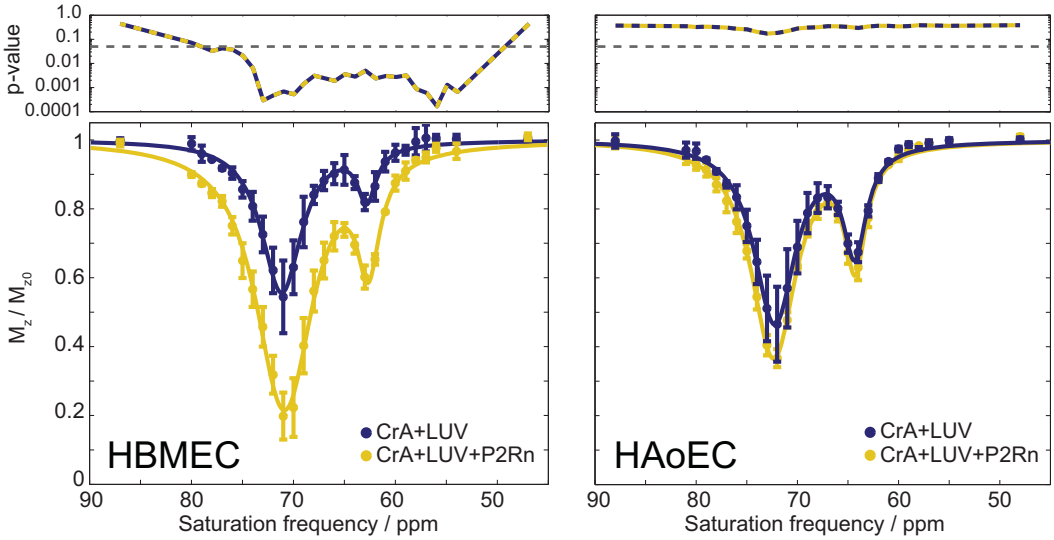

Figure 4.39 – Hyper-CEST spectra with 0.5×10^6/mL HBMECs (left) and HAoECs (right) exposed to CrA+LUV and CrA+LUV+P2Rn for 4 h at 310 K (mean and standard deviation of three independent cell batches). The p-value vs. saturation frequency from a paired t-test comparing the Hyper-CEST spectra is plotted as well. Horizontal dashed line: $p = 0.05$. Reproduced from reference [20]. Copyright © 2015 John Wiley and Sons, Inc.

was not such a significant difference for the control HAoECs when comparing the Hyper-CEST effects in the presence of both liposomal carriers.

Targeted MR imaging with liposomal carriers

The final goal for Xe biosensors is to deliver them to the target cell line in vivo and perform MR imaging. The spatial information that can be provided by MRI is essential in, for example, tumor diagnostics. To demonstrate the suitability of the liposomal carrier for MRI, Hyper-CEST MRI was performed at 310 K (Figure 4.40). Therefore the target HBMECs and the control HAoECs were exposed to 13.3 nM carrier concentration (equivalent to 50 µM CrA) of CrA+LUV+P2Rn as described before (4 h, 310 K) and put into two nested NMR tubes at a cell density of 0.8×10^6 cells/mL. The concentration of the liposomal carrier that was taken up by the 0.8×10^6 HBMECs/mL could be estimated to ca. 1 nM, which corresponds to a CrA concentration of 3.8 µM (see section 4.4.4).

This low carrier concentration was enough to produce sufficient contrast in between the two nested NMR tubes containing the two cell lines. In the field of MRI similar carrier concentrations are reached only when taking advantage of CEST (DIA-CEST and PARA-CEST) approaches [193, 204–207]. Yet, without taking advantage of hyperpolarized nuclei, those approaches have to use incubation concentrations of the original contrast agent of up to several mM.

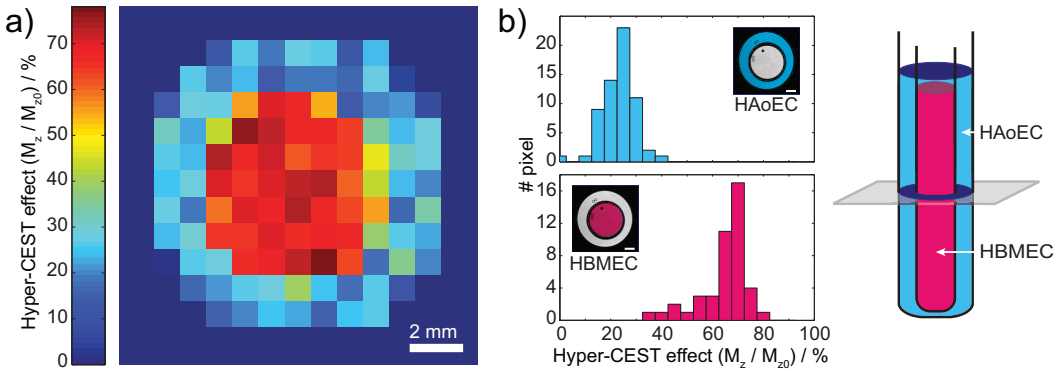

Figure 4.40 – (a) Axial Hyper-CEST MRI of the two nested NMR tubes containing each 0.8×10^6cells/mL. HBMECs in the inner and HAoECs in the outer compartment, both exposed to CrA+LUV+P2Rn for 4 h at 310 K at a carrier concentration of 13.3 nM. Number of averages NS = 20. The single MR images are shown in Figure 4.41. The Hyper-CEST effect outside the two NMR tubes was set to zero. (b) Histogram of the pixelwise Hyper-CEST effect in the outer (top) and the inner compartment (bottom). Reproduced from reference [20]. Copyright © 2015 John Wiley and Sons, Inc.

The cellular uptake of HBMECs mediated by the targeting peptide P2Rn yielded a Hyper-CEST effect of (68.4 ± 4.4) %. Compared to the outer compartment, that contained the HAoECs, this is a difference of a factor 2.9 ± 0.7, which showed a Hyper-CEST effect of (23.4 ± 5.3) %. These compartment-averaged Hyper-CEST effects arise from two clearly distinguishable populations when analyzing the Hyper-CEST effects pixelwise (Figure 4.40b). Again, this demonstrates the specificity of the liposomal carrier produced by P2Rn and the ability of Hyper-CEST MRI to accurately distinguish the two cell lines with only 1 nM carrier concentration.

The MR image shown in Figure 4.40 was determined on the average of 20 Hyper-CEST MR image acquisitions with a RARE pulse sequence (RARE factor 32; in-plane resolution 0.4 mm^2; slice thickness 20 mm). The raw data of the single MR image acquisitions without using any post-processing filter is shown in Figure 4.41. The on- and off-resonant MR images are plotted with the full dynamic range which varies for different images. This explains the different noise levels. In some cases the Hyper-CEST effects obtained from a single pair of off- and on-resonant image already allowed to distinguish the inner and outer compartment. This is particularly important for future in vivo experiments in which no arbitrary number of MR images can be acquired. Yet, for in vivo imaging, the MR signal has to be improved further, by optimizing the ^{129}Xe polarization, the pulse sequences and by using isotopically enriched ^{129}Xe.

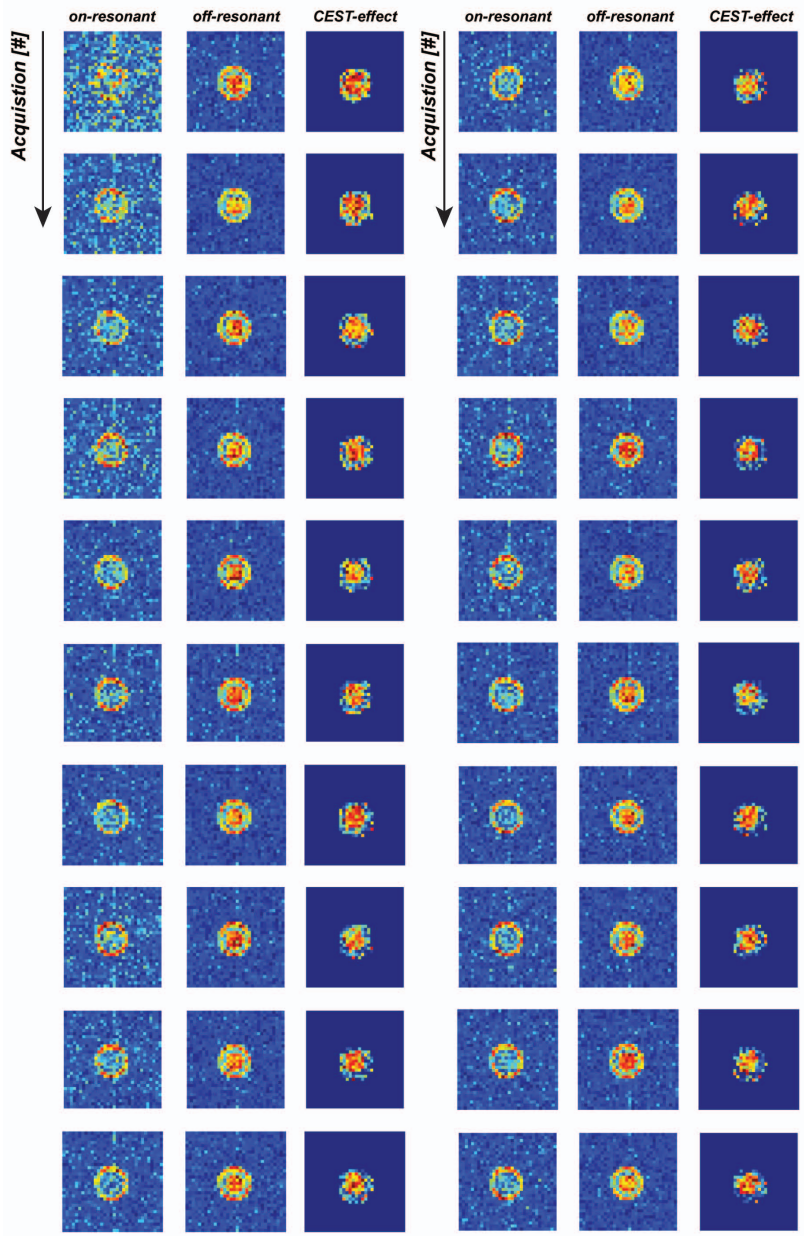

Figure 4.41 – Raw single MR image acquisition with applying saturation pulses with on- and off-resonant frequency (71 and 313 ppm) and the resulting Hyper-CEST effect. The different noise levels result from different dynamic ranges The average of all 20 MR images is shown in Figure 4.40. Reproduced from reference [20]. Copyright © 2015 John Wiley and Sons, Inc.

Estimation of [CrA] per carrier and cell

The concentration of CrA that was delivered by the liposomal carrier to the cells was estimated by measuring the fluorescence intensity of RhPE. Figure 4.42 shows the fluorescence intensity calibration curves of RhPE in dependence of the CrA concentration that was encapsulated in the labeled vesicles. As to be expected, the fluorescence intensity depended linearly on the RhPE and CrA concentration.

With this calibration we checked the cellular uptake of CrA with the different liposomal carriers. Figure 4.43 shows the measured fluorescence intensities in the presence of 3.34×10^5 HBMECs. As in the flow cytometry experiments the RhPE fluorescence in the HBMECs was much stronger when P2Rn was anchored into the liposomal surface. Yet, the highest fluorescence was measured in the supernatant (Figure 4.43b). This means that the largest amount of the carriers was not taken up by the HBMECs and remained in solution. Figure 4.44 relates these fluorescence intensities to the CrA concentration from the calibration curves in Figure 4.42.

1.6 µM CrA were taken up into the HBMECs. Thus the number of CrA molecules delivered through CrA+LUV+P2Rn into a single cell can be estimated by

$$\#\text{CrA/cell} = \frac{1.6\ \mu\text{M}}{3.34 \times 10^5/\text{mL}} \times N_A = 2.9 \times 10^9/\text{cell}. \tag{4.2}$$

Without the peptide P2Rn, the number of CrA molecules can be estimated by

$$\#\text{CrA/cell} = \frac{0.1\ \mu\text{M}}{3.34 \times 10^5/\text{mL}} \times N_A = 1.8 \times 10^8/\text{cell}. \tag{4.3}$$

During the Hyper-CEST experiment only 0.8×10^6 cells/mL were used in the NMR tube. Therefore the concentration of CrA delivered by CrA+LUV+P2Rn was:

$$[\text{CrA}] = \frac{0.8 \times 10^6}{3.34 \times 10^5} \times 1.6\ \mu\text{M} = 3.8\ \mu\text{M}. \tag{4.4}$$

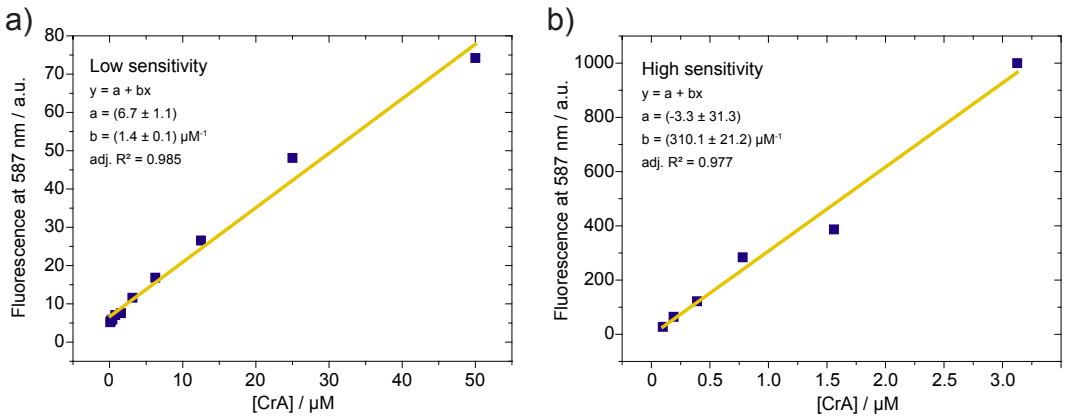

Figure 4.42 – Fluorescence calibration curves of RhPE-labeled CrA+LUV carriers for low (a) and high (b) fluorimeter sensitivity. Reproduced from reference [20]. Copyright © 2015 John Wiley and Sons, Inc.

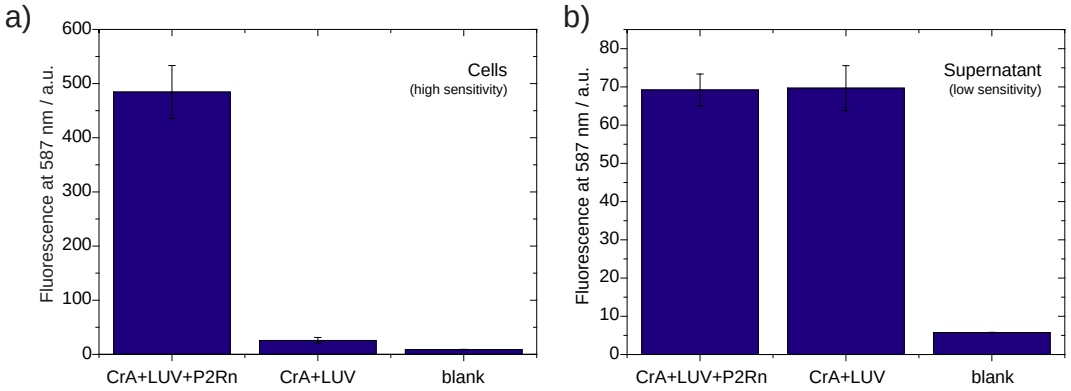

Figure 4.43 – a) RhPE fluorescence intensity at 587 nm of 3.34×10^5 HBMECs incubated with RhPE-labeled CrA+LUV+P2Rn and CrA+LUV for 4 h at 310 K and a blank sample containing HBMECs only. b) The RhPE fluorescence intensity of the supernatant after incubation. Reproduced from reference [20]. Copyright © 2015 John Wiley and Sons, Inc.

As the ratio of lipids to CrA was 75124/20, the concentration of LUVs that were taken up can be estimated by

$$[\text{LUV}] = [\text{CrA}] \times \frac{20}{75124} = 1.0 \text{ nM}. \tag{4.5}$$

4.4.5 Summary

Here, we demonstrated that one can take advantage of the hydrophobic character of CrA and embed it into the lipid bilayers of liposomal carriers. The carriers shield the cytotoxic effect of CrA which might be favorable for future in vivo studies. The specific cell targeting via the anchored peptides combined with the high sensitivity of Hyper-CEST allowed the detection of less than 10^6 cells/mL. The biggest advantage of the liposomal carrier might be that it circumvents direct chemical modifications of CrA. Furthermore, the carrier system can arbitrarily be modified. For example, the targeting peptides might be exchanged with antibodies, which can provide even more specific cell targeting. Adding other drugs and reporters than or next to CrA should also be possible. Thus, the presented system paves the way towards different cell targets and should facilitate first in vivo studies with Hyper-CEST MRI.

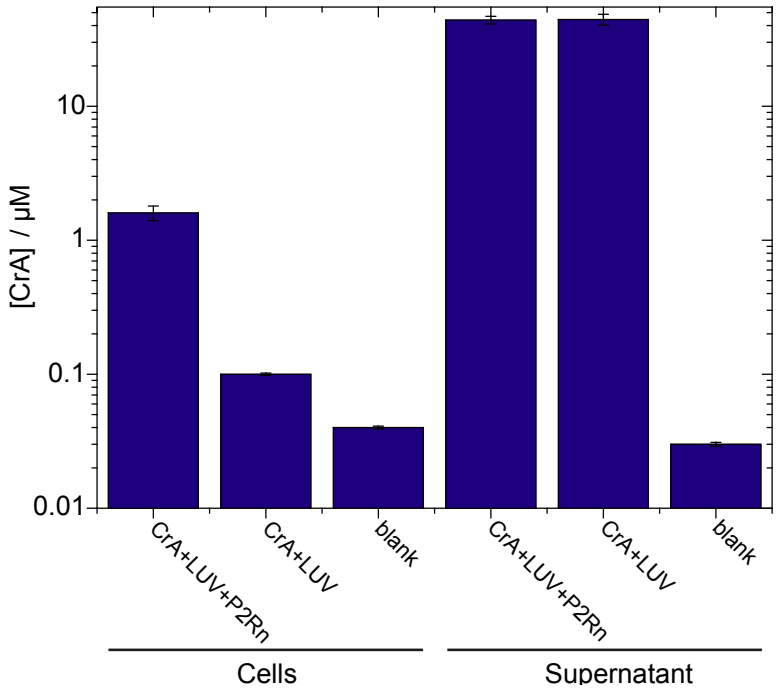

Figure 4.44 – CrA concentration in the samples determined from the RhPE fluorescence intensities shown in Figure 4.42 and 4.43. Reproduced from reference [20]. Copyright © 2015 John Wiley and Sons, Inc.

4.5 Enzymatic activity detected by competitive Xe binding

In molecular imaging cell targeting is usually achieved by targeted contrast agents or carrier systems, as demonstrated in section 4.4. Another possible targeting approach might be the detection of specific enzymes, as enzymatic activity is often upregulated in diseases, e.g. glycolytic enzymes in cancer [208] or antioxidant enzymes in multiple sclerosis [209]. This makes enzymes interesting markers for molecular imaging [11, 210–213].

There have been attempts to sense enzyme activity via a change in chemical shift in Xe NMR upon enzymatic action. However, the chemical shifts that are produced by enzymatic cleavage are very small and are therefore difficult to detect. For example the cleavage of a peptide-labeled CrA induced a chemical shift of the Xe@CrA resonance by only 0.5 ppm [214].

Here we designed a sensor for enzymatic activity that is based on a similar approach as introduced in the previous section by looking at the loss of a Hyper-CEST resonance. This time the reduction of the Hyper-CEST effect is caused by a competitive binding event between Xe atoms and the produced molecule upon enzymatic activity. As a molecular host we used cucurbiturils (CBs) with either 6 or

Figure 4.45 – Scheme of the LDC detection via Hyper-CEST. First Xe is encapsulated in CB (yellow hexagon) and Lys is in solution. The enzyme LDC produces Cad, which shows a higher binding affinity to CB than Xe.

7 subunits to which the binding affinity of an enzymatic substrate is much smaller and that of the corresponding product is much bigger than for Xe. Because of the stronger binding of the product than of Xe to CB, the access of Xe to the molecular hosts is hindered which results into a vanishing Hyper-CEST resonances of Xe@CB.

Figure 4.45 shows schematically the measured enzymatic reaction in presence of Xe atoms and CB molecules. We chose the well understood enzymatic process of decarboxylation of lysine (Lys) to cadavarine (Cad) by the lysine decarboxylase (LDC).

4.5.1 Mapping enzymatic activity in buffer with CB6

Spectroscopic detection of competitive binding

As the interaction of Xe atoms with CBs has not been studied in such detail by Hyper-CEST as the interaction with CrA, we first acquired a Hyper-CEST spectrum of 20 µM CB6 dissolved in 10 mM NH_4OAc buffer (pH 6.0) at 298 K (Figure 4.46). Similarly to the interaction with CrA two resonances were detected. The Hyper-CEST signal at ca. 193 ppm can be ascribed to the known resonance of dissolved Xe, whereas the resonance at 105 ppm arises from the encapsulation of Xe in CB6 (Xe@CB6). Compared to Xe@CrA this is a difference in chemical shift by ca. 45 ppm. Furthermore, the Xe@CB6 resonance is much broader than a typical Xe@CrA resonance at similar temperature and saturation parameters. This indicates a faster exchange rate of Xe out of CB6. Yet the exchange rate is slow enough to provide a separation in chemical shift between dissolved Xe and Xe@CB6.

Adding LDC to the solution did not influence the Xe@CB6 resonance (Figure 4.46), from which we conclude that no significant interaction between CB6 and LDC is present that might influence the Xe exchange in and out of CB6. This was different when 100 µM Lys were added to the solution containing CB6 only. A reduction by ca. 1/3 of the Hyper-CEST effect of the Xe@CB6 resonance was observed. This can be explained by a weak interaction between Lys and CB6 which hampers the interaction of Xe with CB6. However, when we added 15 µg/mL LDC to the solution containing Lys and CB6 the Xe@CB6 resonance vanished completely after a reaction time of 30 min at 298 K. The production of Cad by decarboxylation of Lys through LDC must cause this vanishing of the Xe@CB6 resonance as Cad shows high binding constants

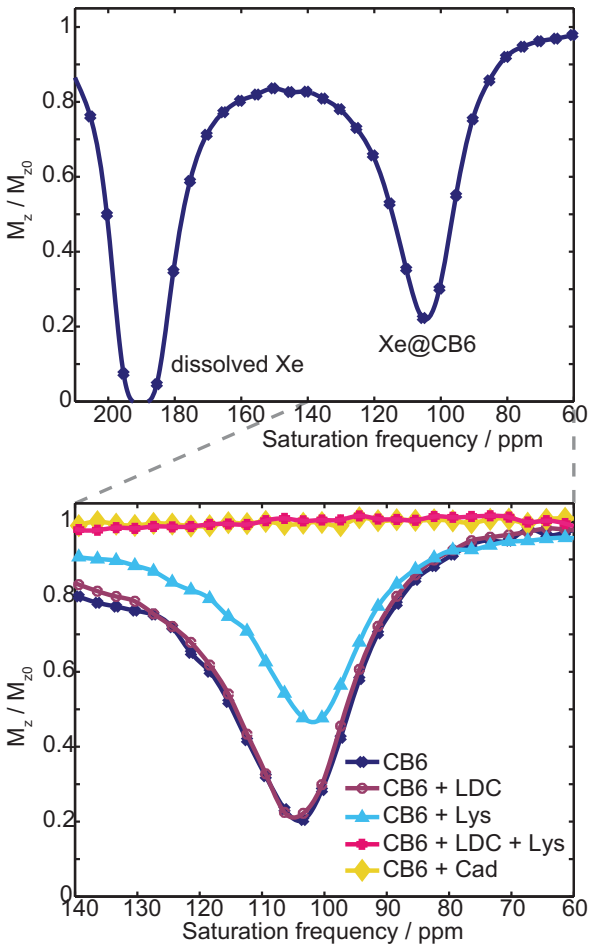

Figure 4.46 – (a) Hyper-CEST spectrum of 20 µM CB6 in 10 mM NH_4OAc buffer at 298 K. Dissolved Xe is at 193 ppm; Xe@CB6 is at 105 ppm. (b) Xe@CB6 resonance of 20 µM CB6 (dark blue spectrum) together with 15 µg/mL LDC (purple), with LDC and 100 µM Lys (magenta), with 50 µM Cad (yellow) and with 100 µM Lys (light blue). Saturation parameters: $B_1 = 16$ µT, $t_{sat} = 4$ s.

with CB6 [215]. Hence, Cad blocks the CB6 molecules and hinders the encapsulation of Xe inside CB6. Cad as the product of the enzymatic reaction blocks CB6 which could be confirmed by adding pure Cad to a solution containing CB6 only, as shown in Figure 4.46.

These experiments clearly demonstrate the possibility to use Hyper-CEST for the sensitive MR detection of enzymatic activity via the competitive interaction with CB6. Furthermore, the great sensitivity provided by Hyper-CEST allowed the detection of CB6 which is remarkable as CB6 was first considered to be unsuitable for direct Xe NMR detection due to its low water solubility [216]. Similar to Xe with CrA

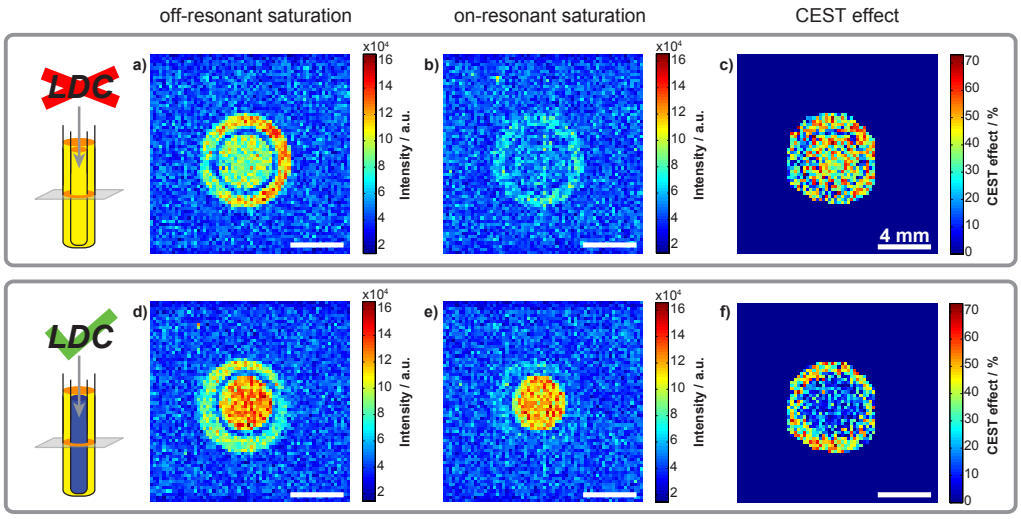

Figure 4.47 – Xe MRI at 298 K of two nested NMR tubes each containing 600 µL 10 mM NH_4OAc buffer with 20 µM CB6 and 100 µM Lys without LDC (a – c) and with 20 µg/mL LDC (d – f) in the inner tube. (a) and (d) show the signal intensity after off-resonant saturation, (c) and (f) after on-resonant saturation at Xe@CB6 and (c) and (f) the respective resulting Hyper-CEST effects. Saturation parameters: $B_1 = 20$ µT, $t_{sat} = 15$ s.

experiments, the large chemical shift difference of 88 ppm between the dissolved Xe and Xe@CB6 resonances even allows to image and thus to spatially encode the enzymatic activity as presented in the following.

MRI localization of enzymatic activity

Figure 4.47 demonstrates the applicability of Hyper-CEST MRI to visualize enzymatic activity at 298 K, here in the case of LDC acting on Lys. Again we used the two nested NMR tubes, where both of them contained 20 µM CB6 and 100 µM Lys in 600 µL 10 mM NH_4OAc buffer. In one experiment 20 µg/mL LDC was added 30 min before data acquisition to the inner compartment (Figure 4.47 d) – f)). In a control experiment (Figure 4.47a – c), no LDC was added to the inner compartment to clearly demonstrate the effect of LDC on Lys.

When applying an off-resonant saturation pulse at 281 ppm (Figure 4.47a and d) both compartments lighted up in both experiments. The slightly inhomogeneous signal distribution is due to the different number of bubbling capillaries in the two NMR tubes (3 in the outer compartment vs. 2 in the inner compartment). Furthermore, the stronger signal of the inner compartment in Figure 4.47d can be explained by the absence of the Xe@CB6 resonance at 105 ppm which results into a sharper resonance (lack of exchange broadening, better SNR) from Xe atoms in aqueous solution.

When applying an on-resonant saturation pulse at 105 ppm (Figure 4.47d and e) only the compartment containing LDC remained unsaturated, compared to the

outer compartment and both compartments in the experiment without LDC. The pixelwise Hyper-CEST effect, which was calculated by subtracting the signal intensity after on-resonant saturation from the signal intensity after off-resonant saturation and normalizing it, clearly highlights the inner compartment in Figure 4.47f where LDC was present. Without the presence of LDC the Hyper-CEST effect was similarly strong in the other compartments. Thus the blocking of CB6 by Cad that was produced by the enzymatic activity of LDC resulted in the spatial change in Hyper-CEST efficiency. To our knowledge this is the first time that enzyme activity was imaged by Xe MRI.

Compared to the other Xe MR images shown in the previous sections of this thesis, the high resolution of these MR images is noteworthy. The final in-plane resolution was 0.05 mm^2 with a slice thickness of 8 mm obtained from a 64×64 matrix, recorded with the RARE pulse sequence (section 3.2.2) with a RARE factor of 64 and only 6 averages. For even better signal quality one might use isotopically enriched gas mixtures and take advantage of faster and improved pulse sequences for data acquisition [217, 218].

4.5.2 Detecting enzymatic activity in a cell lysate with CB7

The larger cavity of CB7 compared to CB6 (279 vs. 164 Å [100]) should provide a much weaker binding of Xe which should result into a faster Xe exchange out of CB7. Because of the weak binding we did not consider CB7 as a suitable host for Xe NMR at first. However, a faster exchange rate might make it a very efficient Hyper-CEST agent. When we recorded a Hyper-CEST spectrum of 270 µM CB7 in H_2O at 295 K we observed indeed a clear Xe@CB7 resonance appeared (Figure 4.48). As with CB6, the resonance vanished upon addition of Cad which hinders the encapsulation of Xe in CB7. Additionally, the resonance of dissolved Xe narrowed a lot upon adding Cad, which can be explained by the absence of Xe exchange.

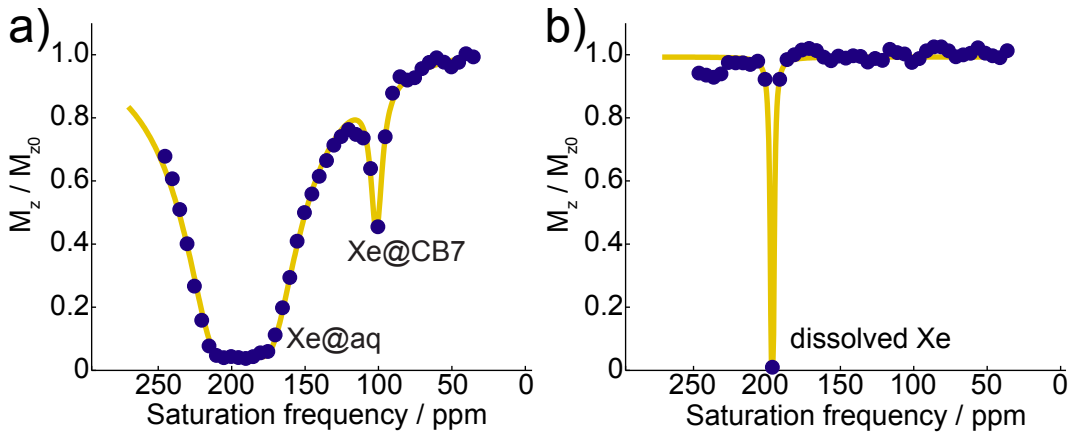

Figure 4.48 – (a) Hyper-CEST spectrum of 270 µM CB7 in H_2O at 295 K. (b) Hyper-CEST spectrum after the addition of 1.9 mM Cad. Saturation parameters: $B_1 = 11$ µT, $t_{sat} = 4$ s.

The great water solubility of CB7 compared to CB6 provided the possibility of recording the enzymatic activity of LDC in the presence of cells. This should simulate a more in-vivo-like situation than checking the activity of LDC just in buffer. For the cell experiments with CB7 we cultured 100×10^6 macrophage cells. The cells were lysed in 1 mL distilled H_2O which yielded 5.9 mg/mL proteins, as measured using the Bradford assay [219]. Protease inhibitors were added to the solution to prevent the destruction through proteolysis of LDC which was added later.

Before the acquisition of the Hyper-CEST spectra, the protein concentration of the cell lysate was diluted to 3 mg/mL in 10 mM NH_4OAc (pH 7.0) to which 2 mM CB7 were added. The resulting Hyper-CEST spectrum is shown in Figure 4.49. Both the dissolved Xe and Xe@CB7 resonances are very broad, similar to the Xe@CrA resonances in the presence of lipids or cells. Yet, the Xe@CB7 resonance was clearly detectable as a pronounced shoulder at ca. 110 ppm. Adding 2.5 mM Lys caused a reduction of the Xe@CB7 resonance that can be explained by the weak interaction between Lys and CB7. Yet, the effect on the Xe@CB7 resonance seems to be bigger than on the Xe@CB6 resonance as shown in section 4.5.1. This can be explained by the larger cavity of CB7 which should facilitate the encapsulation of Lys. Upon addition of 50 µg/mL LDC the Xe@CB7 resonance vanished completely and the dissolved Xe resonance narrowed a lot. Again the production of Cad and its subsequent encapsulation into CB7 should have dominated the Xe encapsulation and thus hindered the Xe exchange that is needed for Hyper-CEST.

4.5.3 Summary

These measurements were the first that detected the presence of an enzyme, namely LDC, using CBs and hyperpolarized Xe in Hyper-CEST NMR and MRI. The concept of a competitive binding to a host (CB) between a guest that is used for signal generation (Xe) and the product of interest (Cad) has not been studied with Hyper-CEST so far. The aim was to establish a complementary approach to existing fluorescence based methods rather than providing a method for in vivo imaging of enzymatic activity. The in vivo situation is much more complex than using such a simple cell lysate and small molecules other than Cad might block the cavity of CB6 or CB7 for Xe, which would require a higher concentration of the host molecule than the one used here. However, these issues are omnipresent in the field of all molecular imaging techniques as well as in biological applications that use supramolecular systems such as CBs. As demonstrated, CBs can be used as a perfect system to establish a highly sensitive NMR sensor for decarboxylation. Furthermore, with these results we believe that other host molecules such as cyclodextrins or calixarenes, that are also considered not to be suitable for conventional Xe NMR, might be used in Hyper-CEST approaches to detect other biological events via competitive binding.

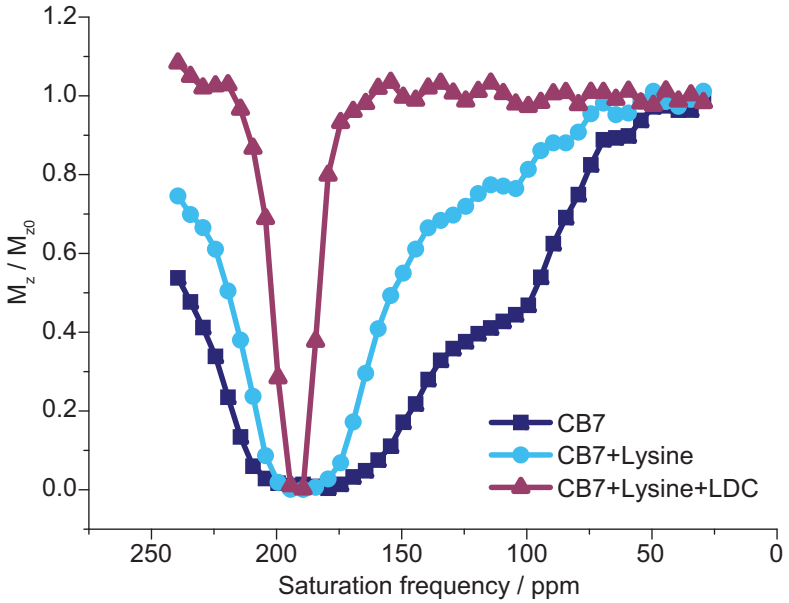

Figure 4.49 – Hyper-CEST spectra of 2 mM CB7 in 10 mM NH_4OAc (pH 7.0) at 298 K in the presence of 3 mg/mL proteins from macrophages (dark blue spectrum), after adding 2.5 mM Lys (light blue spectrum) and after adding 50 µg/mL LDC (purple spectrum). Saturation parameters: $B_1 = 10$ µT, $t_{sat} = 7$ s.

5

Conclusions and perspectives

With the research presented in this thesis we gained new insights into the origin of Hyper-CEST responses in cellular environments as they will occur in future in vivo studies. We also demonstrated the abilities to investigate biophysical properties of biomembrane systems and simple biochemical processes such as enzymatic activity.

As these were the first experiments with Hyper-CEST on membrane fluidity, we kept the studied biomembrane systems as simple as possible by using at maximum binary lipid mixtures. Yet, this allowed us to detect different phases in membrane fluidity, the formation of lipid rafts and the presence of cholesterol. The developed DeLTA approach enabled us to generate MRI contrast via the different phases of fluidity, which might be used to distinguish malignant tumor cells from healthy cells in the future. Because real cellular biomembranes can be arbitrarily complicated, as they contain several different types of lipids, proteins and other molecules, it will be interesting to investigate further model biomembranes with increasing complexity and different lipid mixtures in the future. Moreover, investigations of membrane fluidity of robust and therefore easy to handle bacterias such as bacillus subtilis might provide more knowledge about the action of membrane organizing proteins [8].

The reversible binding of Xe atoms in Hyper-CEST and their permeation into biomembranes allowed us also to measure the formation of small lipid domains, that fluctuated in size. The sensitivity of Hyper-CEST for such fluctuations is a main advantage over commonly used fluorescence microscopy approaches which are not applicable to detect domains that are not macroscopically phase separated. Only Monte-Carlo simulations, differential scanning calorimetry [135] and nearest neighbor recognition measurements [220] can so far also provide information about lipid raft formation in terms of submicroscopic domains.

We demonstrated that Hyper-CEST can also be used to distinguish structural changes in certain membranes that are induced by differently acting antimicrobial peptides. The toroidal pores, produced by the antimicrobial peptide melittin, caused a decrease of the depolarization time once the melittin-to-lipid ratio was above a threshold which was reported in the literature [185]. In contrast, the barrel-stave pores, produced by the antimicrobial peptide alamethicin, increased the depolarization time. Although studies about antimicrobial peptide action on artificial biomembranes started already several decades ago [221], still there exists a highly controversial discussion about the (different) mechanisms of interaction [171, 175, 185]. The

presented approach using Hyper-CEST might help to clarify the picture of how antimicrobial peptides damage and kill microorganisms. Furthermore, the sensitivity of Hyper-CEST on membrane fluidity might also allow to design experiments that support the idea that the action of antimicrobial peptides such as melittin depends not only on the charge of biomembranes but also correlates with the fluidity of the lipids [222]. An obvious advantage of Hyper-CEST over existing methods is the possibility to study the antimicrobial peptide interaction on model biomembranes in their original environment, namely in solution, and artificial conditions, such as attaching biomembranes to glass surfaces [189] can be bypassed.

The original and still main idea of Hyper-CEST is the use of Xe and CrA as biosensors to enable molecular imaging of different diseases [15]. By the presented approach of encapsulating CrA into a peptide-labeled liposomal carrier, biocompatibility and targeting issues of CrA could be bypassed. The chemistry to develop a novel imaging agent is a time-consuming and thus an expensive process. Therefore, one should focus on designing contrast agents based on building blocks. The presented approach to deliver the Xe host CrA via liposomal carriers to the target is such a case. This carrier system can arbitrarily be modified, for example by exchanging the targeting peptides with antibodies [137] or even modify them such that they can be used for therapy as well [223, 224]. Additionally, the possibility to modify such contrast agents can allow multiplexing, which means to visualize different chemical or biological relevant processes simultaneously with one molecular imaging technique [9]. With the additional dimension in terms of chemical shift, MRI is basically made for the demands of multiplexing. This could already be demonstrated in the case of Hyper-CEST [30]. Hence, the next steps regarding liposomal carriers for Hyper-CEST should now take advantage of the present knowledge in liposomal carrier design to achieve even more efficient and specific targeting, provided for example by antibody labeling. For in vivo studies it will be necessary to anchor long PEG molecules into the carrier's surface, which will prolong the blood-circulation time of the liposomal carriers through shielding effects.

For in vivo and in vitro studies competitive binding events of small molecules should be kept in mind, as blocking the imaging agent can affect the Hyper-CEST effect drastically as demonstrated with the decarboxylation of lysine. The resulting decrease in Hyper-CEST effect will unavoidably yield to wrong determinations of the imaging agent concentration. Our presented approach can be seen as a complementary approach to existing methods that are used to detect enzymatic activity rather than using that method in in vivo applications. In the future, fast Hyper-CEST acquisition methods [218] might extend the concept of detecting enzymatic activity through competitive binding events and will maybe allow to determine enzyme kinetics.

Almost all technologies that are present in the field of molecular imaging need imaging agents. A special case holds for conventional MRI which per se does not require an exogenous agent to obtain an image. However, as it is known, without the use of such contrast agents the MR images lack sensitivity. Recently, promising MR methods have been developed that allow the use of modified endogenous molecules as

contrast agents. For example, hyperpolarized ^{13}C-labeled glucose was used to MR image tumor glycolysis by observing the conversion of the labeled glucose into lactate [225]. Imaging endogenous molecules is very promising, as it is still a big challenge to design or to discover biomarkers that can be used for imaging. Although there are a lot of therapeutic biomarkers available that allow efficient and successful treatment of diseases, unfortunately those biomarkers might not be useful for imaging purposes as they demand different requirements. For example the pharmacological effect of a therapeutic biomarker is unwanted in the case of a biomarker that shall only be used for imaging.

To conclude, Hyper-CEST in combination with the presented developed methods gets closer to compare with existing molecular imaging methods. For example, the use of the liposomal carrier allowed us to detect less than 10^6 cells, which is a substantial improvement in Xe MRI sensitivity. The poor resolution of PET also allows the detection of ca. 10^6 cells [9] whereas in terms of sensitivity PET could detect much less cells. Yet, for the field of molecular imaging it is very important that the various techniques do not see each other as opponents but that they rather complement each other.

Bibliography

[1] J. P. Mugler, T. A. Altes, I. C. Ruset, I. M. Dregely, J. F. Mata, G. W. Miller, S. Ketel, J. Ketel, F. W. Hersman, and K. Ruppert. Simultaneous magnetic resonance imaging of ventilation distribution and gas uptake in the human lung using hyperpolarized xenon-129. *Proceedings of the National Academy of Sciences*, 107(50):21707–21712, 2010.

[2] John P. Mugler and Talissa A. Altes. Hyperpolarized ^{129}Xe MRI of the human lung. *Journal of Magnetic Resonance Imaging*, 37(2):313–331, 2013.

[3] Gerald L. Pollack, Richard P. Kennan, Jeffrey F. Himm, and Peter W. Carr. Solubility of xenon in 45 organic solvents including cycloalkanes, acids, and alkanals: Experiment and theory. *The Journal of Chemical Physics*, 90(11):6569–6579, 1989.

[4] Raymond A. Smith, Edith G. Porter, and Keith W. Miller. The solubility of anesthetic gases in lipid bilayers. *Biochimica et Biophysica Acta (BBA) - Biomembranes*, 645(2):327–338, 1981.

[5] R. Lipowsky and E. Sackmann. *Structure and Dynamics of Membranes: I. From Cells to Vesicles / II. Generic and Specific Interactions*. Elsevier, 1995.

[6] Frederick R. Maxfield and Ira Tabas. Role of cholesterol and lipid organization in disease. *Nature*, 438(7068):612–621, 2005.

[7] Reiner Zeisig, Tilen Koklič, Burkhard Wiesner, Iduna Fichtner, and Marjeta Sentjurc. Increase in fluidity in the membrane of MT3 breast cancer cells correlates with enhanced cell adhesion in vitro and increased lung metastasis in NOD/SCID mice. *Archives of Biochemistry and Biophysics*, 459(1):98–106, 2007.

[8] Henrik Strahl, Frank Bürmann, and Leendert W. Hamoen. The actin homologue MreB organizes the bacterial cell membrane. *Nature Communications*, 5:3442, 2014.

[9] Michelle L. James and Sanjiv S. Gambhir. A molecular imaging primer: Modalities, imaging agents, and applications. *Physiological Reviews*, 92(2):897–965, 2012.

[10] Evis Sala, Hebert Alberto Vargas, Olivio F. Donati, Wolfgang A. Weber, and Hedvig Hricak. Role of molecular imaging in the era of personalized medicine: A review. In *Functional Imaging in Oncology*, pages 43–58. Springer Berlin Heidelberg, 2014.

[11] Ralph Weissleder and Mikael J. Pittet. Imaging in the era of molecular oncology. *Nature*, 452(7187):580–589, 2008.

[12] Attila Lorincz, Daad Haddad, Ratna Naik, Vaman Naik, Alan Fung, Alex Cao, Prasad Manda, Abhilash Pandya, Greg Auner, Rajah Rabah, Scott E. Langenburg, and Michael D. Klein. Raman spectroscopy for neoplastic tissue differentiation: a pilot study. *Journal of Pediatric Surgery*, 39(6):953–956, 2004.

[13] Ronald I. Siphanto, Roy G.M. Kolkman, Arjan Huisjes, Magdalena C. Pilatou, Frits F.M. de Mul, Wiendelt Steenbergen, and Leon N.A. van Adrichem. Imaging of small vessels using photoacoustics: An in vivo study. *Lasers in Surgery and Medicine*, 35(5):354–362, 2004.

[14] Rakesh K. Jain, Lance L. Munn, and Dai Fukumura. Dissecting tumour pathophysiology using intravital microscopy. *Nature Reviews Cancer*, 2(4):266–276, 2002.

[15] Leif Schröder, Thomas J. Lowery, Christian Hilty, David E. Wemmer, and Alexander Pines. Molecular imaging using a targeted magnetic resonance hyperpolarized biosensor. *Science*, 314(5798):446–449, 2006.

[16] Stefan Klippel, Jörg Döpfert, Jabadurai Jayapaul, Martin Kunth, Federica Rossella, Matthias Schnurr, Christopher Witte, Christian Freund, and Leif Schröder. Cell tracking with caged xenon: Using cryptophanes as MRI reporters upon cellular internalization. *Angewandte Chemie*, 126(2):503–506, 2014.

[17] Honor M. Rose, Christopher Witte, Federica Rossella, Stefan Klippel, Christian Freund, and Leif Schröder. Development of an antibody-based, modular biosensor for ^{129}Xe NMR molecular imaging of cells at nanomolar concentrations. *Proceedings of the National Academy of Sciences*, 111(32):11697–11702, 2014.

[18] Mikhail G. Shapiro, R. Matthew Ramirez, Lindsay J. Sperling, George Sun, Jinny Sun, Alexander Pines, David V. Schaffer, and Vikram S. Bajaj. Genetically encoded reporters for hyperpolarized xenon magnetic resonance imaging. *Nature Chemistry*, 6(7):629–634, 2014.

[19] Krishnan K. Palaniappan, R. Matthew Ramirez, Vikram S. Bajaj, David E. Wemmer, Alexander Pines, and Matthew B. Francis. Molecular imaging of cancer cells using a bacteriophage-based ^{129}Xe NMR biosensor. *Angewandte Chemie International Edition*, 52(18):4849–4853, 2013.

[20] Matthias Schnurr, Karl Sydow, Honor May Rose, Margitta Dathe, and Leif Schröder. Brain endothelial cell targeting via a peptide-functionalized liposomal carrier for xenon Hyper-CEST MRI. *Advanced Healthcare Materials*, 4(1):40–45, 2015.

[21] Tyler Meldrum, Leif Schröder, Philipp Denger, David E. Wemmer, and Alexander Pines. Xenon-based molecular sensors in lipid suspensions. *Journal of Magnetic Resonance*, 205(2):242–246, 2010.

[22] Evan Unger, Thomas Porter, Jonathan Lindner, and Paul Grayburn. Cardiovascular drug delivery with ultrasound and microbubbles. *Advanced Drug Delivery Reviews*, 72:110–126, 2014.

[23] Miles N. Wernick and John N. Aarsvold. *Emission Tomography: The Fundamentals of PET and SPECT*. Academic Press, 2004.

[24] David J. Stephens and Victoria J. Allan. Light microscopy techniques for live cell imaging. *Science*, 300(5616):82–86, 2003.

[25] Kathryn E. Luker, Mudit Gupta, and Gary D. Luker. Imaging chemokine receptor dimerization with firefly luciferase complementation. *The FASEB Journal*, 23(3):823–834, 2009.

[26] Floris P. R. Verbeek, Joost R. van der Vorst, Boudewijn E. Schaafsma, Rutger-Jan Swijnenburg, Katja N. Gaarenstroom, Henk W. Elzevier, Cornelis J. H. van de Velde, John V. Frangioni, and Alexander L. Vahrmeijer. Intraoperative near infrared fluorescence guided identification of the ureters using low dose methylene blue: A first in human experience. *The Journal of Urology*, 190(2):574–579, 2013.

[27] Mikako Ogawa, Nobuyuki Kosaka, Peter L. Choyke, and Hisataka Kobayashi. In vivo molecular imaging of cancer with a quenching near-infrared fluorescent probe using conjugates of monoclonal antibodies and indocyanine green. *Cancer Research*, 69(4):1268–1272, 2009.

[28] Christopher Witte and Leif Schröder. NMR of hyperpolarised probes. *NMR in Biomedicine*, 26(7):788–802, 2013.

[29] Denis Le Bihan. Diffusion, confusion and functional MRI. *NeuroImage*, 62(2):1131–1136, 2012.

[30] Stefan Klippel, Christian Freund, and Leif Schröder. Multichannel MRI labeling of mammalian cells by switchable nanocarriers for hyperpolarized xenon. *Nano Letters*, 14(10):5721–5726, 2014.

[31] Peter Häussinger, Reinhard Glatthaar, Wilhelm Rhode, Helmut Kick, Christian Benkmann, Josef Weber, Hans-Jörg Wunschel, Viktor Stenke, Edith Leicht, and Hermann Stenger. Noble gases. In *Ullmann's Encyclopedia of Industrial Chemistry*. Wiley-VCH Verlag GmbH & Co. KGaA, 2000.

[32] Bryan D Jordan and Elizabeth Laura Wright. Xenon as an anesthetic agent. *AANA journal*, 78(5):387–392, 2010.

[33] Stephen Lang, Igor L. Moudrakovski, Christopher I. Ratcliffe, John A. Ripmeester, and Giles Santyr. Increasing the spin-lattice relaxation time of hyperpolarized xenon ice at 4.2 K. *Appl. Phys. Lett.*, 80(5):886–887, 2002.

[34] Andrea Stith, T. Kevin Hitchens, Denise P. Hinton, Stuart S. Berr, Bastiaan Driehuys, James R. Brookeman, and Robert G. Bryant. Consequences of ^{129}Xe-^{1}H cross relaxation in aqueous solutions. *Journal of Magnetic Resonance*, 139(2):225–231, 1999.

[35] M. S. Albert, V. D. Schepkin, and T. F. Budinger. Measurement of ^{129}Xe T1 in blood to explore the feasibility of hyperpolarized ^{129}Xe MRI. *Journal of Computer Assisted Tomography*, 19(6):975–978, 1995.

[36] Philippe Choquet, Jean-Noël Hyacinthe, Guillaume Duhamel, Emmanuelle Grillon, Jean-Louis Leviel, André Constantinesco, and Anne Ziegler. Method to determine in vivo the relaxation time T1 of hyperpolarized xenon in rat brain. *Magnetic Resonance in Medicine*, 49(6):1014–1018, 2003.

[37] Audi, Bersillon, Blachot, and Wapstra. The nubase evaluation of nuclear and decay properties. *Nuclear Physics*, A 729:3–128, 2003.

[38] G. E. Uhlenbeck and S. Goudsmit. Ersetzung der Hypothese vom unmechanischen Zwang durch eine Forderung bezüglich des inneren Verhaltens jedes einzelnen Elektrons. *Die Naturwissenschaften*, 13(47):953–954, 1925.

[39] F. Bloch. Nuclear induction. *Physical Review*, 70(7-8):460–474, 1946.

[40] E. M. Purcell, H. C. Torrey, and R. V. Pound. Resonance absorption by nuclear magnetic moments in a solid. *Physical Review*, 69(1-2):37–38, 1946.

[41] P. C. Lauterbur. Image formation by induced local interactions: Examples employing nuclear magnetic resonance. *Nature*, 242(5394):190–191, 1973.

[42] P Mansfield and P K Grannell. NMR 'diffraction' in solids? *Journal of Physics C: Solid State Physics*, (22):L422, 1973.

[43] Steven D. Bass. How Does the Proton Spin? *Science*, 315(5819):1672–1673, 2007.

[44] Keith W. Miller, Nicholas V. Reo, Antonius J. M. Schoot Uiterkamp, Diane P. Stengle, Thomas R. Stengle, and Kenneth L. Williamson. Xenon NMR: Chemical shifts of a general anesthetic in common solvents, proteins, and membranes. *Proceedings of the National Academy of Sciences of the United States of America*, 78(8):4946–4949, 1981.

[45] Seth M. Rubin, Seok-Yong Lee, E. Janette Ruiz, Alexander Pines, and David E. Wemmer. Detection and characterization of xenon-binding sites in proteins by ^{129}Xe NMR spectroscopy. *Journal of Molecular Biology*, 322(2):425–440, 2002.

[46] Leif Schröder, Tyler Meldrum, Monica Smith, Thomas J. Lowery, David E. Wemmer, and Alexander Pines. Temperature response of ^{129}Xe depolarization transfer and its application for ultrasensitive NMR detection. *Physical Review Letters*, 100(25):257603, 2008.

[47] Matthias Schnurr, Christopher Witte, and Leif Schröder. Depolarization laplace transform analysis of exchangeable hyperpolarized ^{129}Xe for detecting ordering phases and cholesterol content of biomembrane models. *Biophysical Journal*, 106(6):1301–1308, 2014.

[48] Todd K. Stevens, Krishnan K. Palaniappan, R. Matthew Ramirez, Matthew B. Francis, David E. Wemmer, and Alex Pines. HyperCEST detection of a ^{129}Xe-based contrast agent composed of cryptophane-a molecular cages on a bacteriophage scaffold. *Magnetic Resonance in Medicine*, 69(5):1245–1252, 2013.

[49] Todd K. Stevens, R. Matthew Ramirez, and Alexander Pines. Nanoemulsion contrast agents with sub-picomolar sensitivity for xenon NMR. *Journal of the American Chemical Society*, 135(26):9576–9579, 2013.

[50] M. S. Freeman, K. Emami, and B. Driehuys. Characterizing and modeling the efficiency limits in large-scale production of hyperpolarized Xe129. *Physical Review A*, 90(2):023406, 2014.

[51] Panayiotis Nikolaou, Aaron M. Coffey, Michael J. Barlow, Matthew S. Rosen, Boyd M. Goodson, and Eduard Y. Chekmenev. Temperature-ramped ^{129}Xe spin-exchange optical pumping. *Analytical Chemistry*, 2014.

[52] Panayiotis Nikolaou, Aaron M. Coffey, Laura L. Walkup, Brogan M. Gust, Nicholas Whiting, Hayley Newton, Scott Barcus, Iga Muradyan, Mikayel Dabaghyan, Gregory D. Moroz, Matthew S. Rosen, Samuel Patz, Michael J. Barlow, Eduard Y. Chekmenev, and Boyd M. Goodson. Near-unity nuclear polarization with an open-source ^{129}Xe hyperpolarizer for NMR and MRI. *Proceedings of the National Academy of Sciences*, 110(35):14150–14155, 2013.

[53] Panayiotis Nikolaou, Aaron M. Coffey, Kaili Ranta, Laura L. Walkup, Brogan M. Gust, Michael J. Barlow, Matthew S. Rosen, Boyd M. Goodson, and Eduard Y. Chekmenev. Multidimensional mapping of spin-exchange optical pumping in clinical-scale batch-mode ^{129}Xe hyperpolarizers. *The Journal of Physical Chemistry B*, 118(18):4809–4816, 2014.

[54] C. Witte, M. Kunth, F. Rossella, and L. Schröder. Observing and preventing rubidium runaway in a direct-infusion xenon-spin hyperpolarizer optimized for high-resolution hyper-CEST (chemical exchange saturation transfer using hyperpolarized nuclei) NMR. *The Journal of Chemical Physics*, 140(8):084203, 2014.

[55] I. Ruset, S. Ketel, and F. Hersman. Optical Pumping System Design for Large Production of Hyperpolarized Xe129. *Physical Review Letters*, 96(5):053002, 2006.

[56] Albert W. Overhauser. Polarization of nuclei in metals. *Physical Review*, 92(2):411–415, 1953.

[57] Charles P. Slichter. The discovery and renaissance of dynamic nuclear polarization. *Reports on Progress in Physics*, 77(7):072501, 2014.

[58] C. Russell Bowers and D. P. Weitekamp. Parahydrogen and synthesis allow dramatically enhanced nuclear alignment. *Journal of the American Chemical Society*, 109(18):5541–5542, 1987.

[59] Johannes Natterer and Joachim Bargon. Parahydrogen induced polarization. *Progress in Nuclear Magnetic Resonance Spectroscopy*, 31(4):293–315, 1997.

[60] Thad G. Walker and William Happer. Spin-exchange optical pumping of noble-gas nuclei. *Rev. Mod. Phys.*, 69(2):629–642, 1997.

[61] Kevin M. Brindle, Sarah E. Bohndiek, Ferdia A. Gallagher, and Mikko I. Kettunen. Tumor imaging using hyperpolarized ^{13}C magnetic resonance spectroscopy. *Magnetic Resonance in Medicine*, 66(2):505–519, 2011.

[62] K Golman, L E Olsson, O Axelsson, S Månsson, M Karlsson, and J S Petersson. Molecular imaging using hyperpolarized ^{13}C. *The British Journal of Radiology*, 76(76):S118–S127, 2003.

[63] Alfred Kastler. Quelques suggestions concernant la production optique et la détection optique d'une inégalité de population des niveaux de quantifigation spatiale des atomes. application à l'expérience de stern et gerlach et à la résonance magnétique. *J. Phys. Radium*, 11(6):255–265, 1950.

[64] Daniel A Steck. Rubidium 87 D line data. http://www.steck.us/alkalidata/rubidium87numbers.pdf, 2001. [accessed 21-Jan-2015].

[65] M. E. Wagshul and T. E. Chupp. Laser optical pumping of high-density Rb in polarized ^{3}He targets. *Physical Review A*, 49(5):3854–3869, 1994.

[66] A. Fink, D. Baumer, and E. Brunner. Production of hyperpolarized xenon in a static pump cell: Numerical simulations and experiments. *Physical Review A*, 72(5):05341–1–9, 2005.

[67] S. Appelt. From photon spin to magnetic resonance imaging, 2004.

[68] F. Colegrove, L. Schearer, and G. Walters. Polarization of ^{3}He gas by optical pumping. *Physical Review*, 132(6):2561–2572, 1963.

[69] Ming F. Hsu, G. D. Cates, I. Kominis, I. A. Aksay, and D. M. Dabbs. Sol-gel coated glass cells for spin-exchange polarized ^{3}He. *Applied Physics Letters*, 77(13):2069–2071, 2000.

[70] Leif Schröder, Thomas J. Lowery, Christian Hilty, David E. Wemmer, and Alexander Pines. Molecular imaging using a targeted magnetic resonance hyperpolarized biosensor. *Science*, 314(5798):446–449, 2006.

[71] Steven D. Wolff and Robert S. Balaban. NMR imaging of labile proton exchange. *Journal of Magnetic Resonance*, 86(1):164–169, 1990.

[72] K M Ward, A H Aletras, and R S Balaban. A new class of contrast agents for MRI based on proton chemical exchange dependent saturation transfer (CEST). *Journal of Magnetic Resonance*, 143(1):79–87, 2000.

[73] Moritz Zaiss and Peter Bachert. Chemical exchange saturation transfer (CEST) and MR z-spectroscopy in vivo: a review of theoretical approaches and methods. *Physics in Medicine and Biology*, 58(22):R221, 2013.

[74] Yubin Bai, P. Aru Hill, and Ivan J. Dmochowski. Utilizing a water-soluble cryptophane with fast xenon exchange rates for picomolar sensitivity NMR measurements. *Analytical Chemistry*, 84(22):9935–9941, 2012.

[75] Leif Schröder, Lana Chavez, Tyler Meldrum, Monica Smith, Thomas J. Lowery, David E. Wemmer, and Alexander Pines. Temperature-controlled molecular depolarization gates in nuclear magnetic resonance. *Angewandte Chemie International Edition*, 47(23):4316–4320, 2008.

[76] Martin Kunth, Jörg Döpfert, Christopher Witte, Federica Rossella, and Leif Schröder. Optimized use of reversible binding for fast and selective NMR localization of caged xenon. *Angewandte Chemie International Edition*, 51(33):8217–8220, 2012.

[77] Tyler Meldrum, Vikram S Bajaj, David E Wemmer, and Alexander Pines. Band-selective chemical exchange saturation transfer imaging with hyperpolarized xenon-based molecular sensors. *Journal of Magnetic Resonance*, 213(1):14–21, 2011.

[78] Moritz Zaiss, Matthias Schnurr, and Peter Bachert. Analytical solution for the depolarization of hyperpolarized nuclei by chemical exchange saturation transfer between free and encapsulated xenon (HyperCEST). *The Journal of Chemical Physics*, 136(14):144106–10, 2012.

[79] M. Kunth, C. Witte, and L. Schröder. Quantitative chemical exchange saturation transfer with hyperpolarized nuclei (qHyper-CEST): Sensing xenon-host exchange dynamics and binding affinities by NMR. *The Journal of Chemical Physics*, 141(19):194202, 2014.

[80] S. Peresada, A. Tonielli, R. Morici, and C. S. Johnson. Diffusion ordered nuclear magnetic resonance spectroscopy: principles and applications. *Progress in Nuclear Magnetic Resonance Spectroscopy*, 34(3):203–256, 1999.

[81] Harri Koskela, Outi Heikkinen, Ilkka Kilpeläinen, and Sami Heikkinen. Rapid and accurate processing method for amide proton exchange rate measurement in proteins. *Journal of Biomolecular NMR*, 37(4):313–320, 2007.

[82] Harri Koskela, Ilkka Kilpeläinen, and Sami Heikkinen. Evaluation of protein ^{15}N relaxation times by inverse laplace transformation. *Magnetic Resonance in Chemistry*, 42(1):61–65, 2004.

[83] Z Bajzer, A C Myers, S S Sedarous, and F G Prendergast. Padé-laplace method for analysis of fluorescence intensity decay. *Biophysical Journal*, 56(1):79–93, 1989.

[84] J. Jakeš and P. Štěpánek. Positive exponential sum method of inverting laplace transform applied to photon correlation spectroscopy. *Czechoslovak Journal of Physics*, 40(9):972–983, 1990.

[85] Per Christian Hansen. *Rank-Deficient and Discrete Ill-Posed Problems: Numerical Aspects of Linear Inversion*. SIAM, 1997.

[86] Iari-Gabriel Marino. rilt.m. `http://www.mathworks.com/matlabcentral/fileexchange/6523-rilt/content/rilt.m`, 2007. [accessed 18-March-2013].

[87] Stephen W. Provencher. CONTIN: A general purpose constrained regularization program for inverting noisy linear algebraic and integral equations. *Computer Physics Communications*, 27(3):229–242, 1982.

[88] Andreĭ Nikolaevich Tikhonov and Vasiliĭ Iakovlevich Arsenin. *Solutions of ill-posed problems*. Winston, 1977.

[89] Jacqueline Gabard and Andrea Collet. Synthesis of a (D 3)-bis(cyclotriveratrylenyl) macrocage by stereospecific replication of a (C 3)-subunit. *Journal of the Chemical Society, Chemical Communications*, (21):1137, 1981.

[90] Kristin Bartik, Michel Luhmer, Jean-Pierre Dutasta, André Collet, and Jacques Reisse. ^{129}Xe and 1h NMR study of the reversible trapping of xenon by cryptophane-a in organic solution. *Journal of the American Chemical Society*, 120(4):784–791, 1998-02-01.

[91] Olena Taratula, P. Aru Hill, Najat S. Khan, Patrick J. Carroll, and Ivan J. Dmochowski. Crystallographic observation of 'induced fit' in a cryptophane host-guest model system. *Nature Communications*, 1:148, 2010.

[92] S. Mecozzi and J. Rebek. The 55% solution: A formula for molecular recognition in the liquid state. *Chemistry*, 4(6):1016–1022, 1998.

[93] Thierry Brotin and Jean-Pierre Dutasta. Xecryptophane complexes with C2 symmetry: Synthesis and investigations by ^{129}Xe NMR of the consequences of the size of the host cavity for xenon encapsulation. *European Journal of Organic Chemistry*, 2003(6):973–984, 2003.

[94] Gaspard Huber, Thierry Brotin, Lionel Dubois, Hervé Desvaux, Jean-Pierre Dutasta, and Patrick Berthault. Water soluble cryptophanes showing unprecedented affinity for xenon: candidates as NMR-based biosensors. *Journal of the American Chemical Society*, 128(18):6239–6246, 2006.

[95] Megan M. Spence, E. Janette Ruiz, Seth M. Rubin, Thomas J. Lowery, Nicolas Winssinger, Peter G. Schultz, David E. Wemmer, and Alexander Pines. Development of a functionalized xenon biosensor. *Journal of the American Chemical Society*, 126(46):15287–15294, 2004.

[96] Robert M. Fairchild, Akil I. Joseph, K. Travis Holman, Heather A. Fogarty, Thierry Brotin, Jean-Pierre Dutasta, Ceéline Boutin, Gaspard Huber, and Patrick Berthault. A water-soluble xe@cryptophane-111 complex exhibits very high thermodynamic stability and a peculiar ^{129}Xe NMR chemical shift. *J. Am. Chem. Soc.*, 132(44):15505–15507, 2010.

[97] Emmanuelle Dubost, Naoko Kotera, Sébastien Garcia-Argote, Yves Boulard, Estelle Léonce, Céline Boutin, Patrick Berthault, Christophe Dugave, and Bernard Rousseau. Synthesis of a functionalizable water-soluble cryptophane-111. *Organic letters*, 15(11):2866–2868, 2013.

[98] Céline Boutin, Antoine Stopin, Fatimazohra Lenda, Thierry Brotin, Jean-Pierre Dutasta, Nadège Jamin, Alain Sanson, Yves Boulard, François Leteurtre, Gaspard Huber, Aurore Bogaert-Buchmann, Nawal Tassali, Hervé Desvaux, Marie Carrière, and Patrick

Berthault. Cell uptake of a biosensor detected by hyperpolarized ^{129}Xe NMR: The transferrin case. *Bioorganic & Medicinal Chemistry*, 19(13):4135–4143, 2011.

[99] W. A. Freeman, W. L. Mock, and N. Y. Shih. Cucurbituril. *Journal of the American Chemical Society*, 103(24):7367–7368, 1981.

[100] Jason Lagona, Pritam Mukhopadhyay, Sriparna Chakrabarti, and Lyle Isaacs. The cucurbit[n]uril family. *Angewandte Chemie International Edition*, 44(31):4844–4870, 2005.

[101] Eric Masson, Xiaoxi Ling, Roymon Joseph, Lawrence Kyeremeh-Mensah, and Xiaoyong Lu. Cucurbituril chemistry: a tale of supramolecular success. *RSC Advances*, 2(4):1213–1247, 2012.

[102] Jianzhang Zhao, Hee-Joon Kim, Jinho Oh, Soo-Young Kim, Jae Wook Lee, Shigeru Sakamoto, Kentaro Yamaguchi, and Kimoon Kim. Cucurbit[n]uril derivatives soluble in water and organic solvents. *Angewandte Chemie*, 113(22):4363–4365, 2001.

[103] Byoung Soo Kim, Young Ho Ko, Youngkook Kim, Hyeong Ju Lee, N. Selvapalam, Hee Cheon Lee, and Kimoon Kim. Water soluble cucurbit[6]uril derivative as a potential xe carrier for ^{129}Xe NMR-based biosensors. *Chemical Communications*, (24):2756–2758, 2008.

[104] Gaspard Huber, François-Xavier Legrand, Véronique Lewin, Delphine Baumann, Marie-Pierre Heck, and Patrick Berthault. Interaction of xenon with cucurbit[5]uril in water. *ChemPhysChem*, 12(6):1053–1055, 2011.

[105] Roy N. Dsouza, Andreas Hennig, and Werner M. Nau. Supramolecular tandem enzyme assays. *Chemistry - A European Journal*, 18(12):3444–3459, 2012.

[106] Andreas Hennig, Hüseyin Bakirci, and Werner M. Nau. Label-free continuous enzyme assays with macrocycle-fluorescent dye complexes. *Nature Methods*, 4(8):629–632, 2007.

[107] Werner M. Nau, Garima Ghale, Andreas Hennig, Hüseyin Bakirci, and David M. Bailey. Substrate-selective supramolecular tandem assays: Monitoring enzyme inhibition of arginase and diamine oxidase by fluorescent dye displacement from calixarene and cucurbituril macrocycles. *Journal of the American Chemical Society*, 131(32):11558–11570, 2009.

[108] Andreas Hennig, Garima Ghale, and Werner M. Nau. Effects of cucurbit[7]uril on enzymatic activity. *Chemical Communications*, (16):1614–1616, 2007.

[109] P. R. Locher. Computer simulation of selective excitation in n.m.r. imaging. *Philosophical Transactions of the Royal Society of London. Series B, Biological Sciences*, 289(1037):537–542, 1980.

[110] J. Hennig, A. Nauerth, and H. Friedburg. RARE imaging: A fast imaging method for clinical MR. *Magnetic Resonance in Medicine*, 3(6):823–833, 1986.

[111] J. Hennig and H. Friedburg. Clinical applications and methodological developments of the RARE technique. *Magnetic Resonance Imaging*, 6(4):391–395, 1988.

[112] P. S. Melki, R. V. Mulkern, L. P. Panych, and F. A. Jolesz. Comparing the FAISE method with conventional dual-echo sequences. *Journal of Magnetic Resonance Imaging*, 1(3):319–326, 1991.

[113] P. Mansfield. Multi-planar image formation using NMR spin echoes. *Journal of Physics C Solid State Physics*, 10:L55–L58, 1977.

[114] P Mansfield and I. L Pykett. Biological and medical imaging by NMR. *Journal of Magnetic Resonance*, 29(2):355–373, 1978.

[115] D. G. Norris. Ultrafast low-angle RARE: U-FLARE. *Magnetic Resonance in Medicine*, 17(2):539–542, 1991.

[116] Bruce Alberts, Alexander Johnson, Peter Walter, Julian Lewis, Martin Raff, Keith Roberts, and Nigel Orme. *Molecular Biology of the Cell*. Taylor & Francis Ltd., New York, 2007.

[117] W. Dowhan. MOLECULAR BASIS FOR MEMBRANE PHOSPHOLIPID DIVERSITY:why are there so many lipids? *Annual Review of Biochemistry*, 66(1):199–232, 1997.

[118] Nathan S. Ihrcke, Lucile E. Wrenshall, Bonnie J. Lindman, and Jeffrey L. Platt. Role of heparan sulfate in immune system-blood vessel interactions. *Immunology Today*, 14(10):500–505, 1993.

[119] Barbro B. Johansson. Blood-brain barrier: Role of brain endothelial surface charge and glycocalyx. In *Ischemic Blood Flow in the Brain*, number 6 in Keio University Symposia for Life Science and Medicine, pages 33–38. Springer Japan, 2001.

[120] Derek Marsh. Liquid-ordered phases induced by cholesterol: A compendium of binary phase diagrams. *Biochimica et Biophysica Acta (BBA) - Biomembranes*, 1798(3):688–699, 2010.

[121] Derek Marsh. Cholesterol-induced fluid membrane domains: A compendium of lipid-raft ternary phase diagrams. *Biochimica et Biophysica Acta (BBA) - Biomembranes*, 1788(10):2114–2123, 2009.

[122] Rumiana Koynova and Martin Caffrey. Phases and phase transitions of the phosphatidylcholines. *Biochimica et Biophysica Acta (BBA) - Reviews on Biomembranes*, 1376(1):91–145, 1998.

[123] Sharmin N. Ahmed, Deborah A. Brown, and Erwin London. On the origin of sphingolipid/cholesterol-rich detergent-insoluble cell membranes: Physiological concentrations of cholesterol and sphingolipid induce formation of a detergent-insoluble, liquid-ordered lipid phase in model membranes. *Biochemistry*, 36(36):10944–10953, 1997.

[124] M. Lafleur, P. R. Cullis, and M. Bloom. Modulation of the orientational order profile of the lipid acyl chain in the l_α phase. *European Biophysics Journal*, 19(2):55–62, 1990.

[125] T.X. Xiang and B.D. Anderson. Permeability of acetic acid across gel and liquid-crystalline lipid bilayers conforms to free-surface-area theory. *Biophysical Journal*, 72(1):223–237, 1997.

[126] C Reyes Mateo, A Ulises Acuna, and J C Brochon. Liquid-crystalline phases of cholesterol/lipid bilayers as revealed by the fluorescence of trans-parinaric acid. *Biophysical Journal*, 68(3):978–987, 1995.

[127] Sarah L. Veatch and Sarah L. Keller. Separation of liquid phases in giant vesicles of ternary mixtures of phospholipids and cholesterol. *Biophysical Journal*, 85(5):3074–3083, 2003.

[128] Anton Rietveld and Kai Simons. The differential miscibility of lipids as the basis for the formation of functional membrane rafts. *Biochimica et Biophysica Acta (BBA) - Reviews on Biomembranes*, 1376(3):467–479, 1998.

[129] Kai Simons and Elina Ikonen. Functional rafts in cell membranes. *Nature*, 387(6633):569–572, 1997.

[130] J. L. Thewalt and M. Bloom. Phosphatidylcholine: cholesterol phase diagrams. *Biophysical Journal*, 63(4):1176–1181, 1992.

[131] Rodrigo F. M. de Almeida, Aleksandre Fedorov, and Manuel Prieto. Sphingomyelin/phosphatidylcholine/cholesterol phase diagram: Boundaries and composition of lipid rafts. *Biophysical Journal*, 85(4):2406–2416, 2003.

[132] Laura Anchisi, Sandra Dessi, Alessandra Pani, and Antonella Mandas. Cholesterol homeostasis: a key to prevent or slow down neurodegeneration. *Membrane Physiology and Membrane Biophysics*, 3:486, 2013.

[133] L. J. Pike. The challenge of lipid rafts. *The Journal of Lipid Research*, 50(Supplement):S323–S328, 2008.

[134] William Curatolo, Barry Sears, and Leo J. Neuringer. A calorimetry and deuterium NMR study of mixed model membranes of 1-palmitoyl-2-oleylphosphatidylcholine and saturated phosphatidylcholines. *Biochimica et Biophysica Acta (BBA) - Biomembranes*, 817(2):261–270, 1985.

[135] James A. Svetlovics, Sterling A. Wheaten, and Paulo F. Almeida. Phase separation and fluctuations in mixtures of a saturated and an unsaturated phospholipid. *Biophysical Journal*, 102(11):2526–2535, 2012.

[136] Roland Faller. *Biomembrane Frontiers: Nanostructures, Models, and the Design of Life*. Springer, 2009.

[137] Vladimir P. Torchilin. Recent advances with liposomes as pharmaceutical carriers. *Nature Reviews Drug Discovery*, 4(2):145–160, 2005.

[138] Robert C. MacDonald, Ruby I. MacDonald, Bert Ph.M. Menco, Keizo Takeshita, Nanda K. Subbarao, and Lan-rong Hu. Small-volume extrusion apparatus for preparation of large, unilamellar vesicles. *Biochimica et Biophysica Acta (BBA) - Biomembranes*, 1061(2):297–303, 1991.

[139] A. Moscho, O. Orwar, D. T. Chiu, B. P. Modi, and R. N. Zare. Rapid preparation of giant unilamellar vesicles. *Proceedings of the National Academy of Sciences*, 93(21):11443–11447, 1996.

[140] John Charles Marshall Stewart. Colorimetric determination of phospholipids with ammonium ferrothiocyanate. *Analytical Biochemistry*, 104(1):10–14, 1980.

[141] Gregory Gregoriadis. *Liposome Technology: Liposome Preparation and Related Techniques*. CRC Press, 2006.

[142] Bruce J. Berne and Robert Pecora. *Dynamic Light Scattering: With Applications to Chemistry, Biology, and Physics*. Courier Dover Publications, 2000.

[143] Th Förster. Zwischenmolekulare Energiewanderung und Fluoreszenz. *Annalen der Physik*, 437(1):55–75, 1948.

[144] Soumi Mukherjee, H. Raghuraman, and Amitabha Chattopadhyay. Membrane localization and dynamics of nile red: Effect of cholesterol. *Biochimica et Biophysica Acta (BBA) - Biomembranes*, 1768(1):59–66, 2007.

[145] Robert M. Clegg. Chapter 1 Förster resonance energy transfer-FRET what is it, why do it, and how it's done. In *Laboratory Techniques in Biochemistry and Molecular Biology*, volume 33 of *Fret and Flim Techniques*, pages 1–57. Elsevier, 2009.

[146] Bo Medhage, Emad Mukhtar, Björn Kalman, Lennart B.-Å Johansson, and Julian G. Molotkovsky. Electronic energy transfer in anisotropic systems. part 5. *Journal of the Chemical Society, Faraday Transactions*, 88(19):2845–2851, 1992.

[147] L. M. Loura, A. Fedorov, and M. Prieto. Fluid-fluid membrane microheterogeneity: a fluorescence resonance energy transfer study. *Biophysical Journal*, 80(2):776–788, 2001.

[148] Lesley Davenport, Robert E. Dale, Roger H. Bisby, and Robert B. Cundall. Transverse location of the fluorescent probe 1,6-diphenyl-1,3,5-hexatriene in model lipid bilayer membrane systems by resonance excitation energy transfer. *Biochemistry*, 24(15):4097–4108, 1985.

[149] Malin Ardhammar, Per Lincoln, and Bengt Nordén. Invisible liposomes: Refractive index matching with sucrose enables flow dichroism assessment of peptide orientation in lipid vesicle membrane. *Proceedings of the National Academy of Sciences*, 99(24):15313–15317, 2002.

[150] P. N. Yi and R. C. MacDonald. Temperature dependence of optical properties of aqueous dispersions of phosphatidylcholine. *Chemistry and Physics of Lipids*, 11(2):114–134, 1973.

[151] C. S. Chong and Konrad Colbow. Light scattering and turbidity measurements on lipid vesicles. *Biochimica et Biophysica Acta (BBA) - Biomembranes*, 436(2):260–282, 1976.

[152] Christian Wuürth, Markus Grabolle, Jutta Pauli, Monika Spieles, and Ute Resch-Genger. Comparison of methods and achievable uncertainties for the relative and absolute measurement of photoluminescence quantum yields. *Analytical Chemistry*, 83(9):3431–3439, 2011.

[153] Douglas. Magde, James H. Brannon, Teresa L. Cremers, and John. Olmsted. Absolute luminescence yield of cresyl violet. a standard for the red. *The Journal of Physical Chemistry*, 83(6):696–699, 1979.

[154] Adrienn Cser, Krisztina Nagy, and László Biczók. Fluorescence lifetime of nile red as a probe for the hydrogen bonding strength with its microenvironment. *Chemical Physics Letters*, 360(5-6):473–478, 2002.

[155] Baltazar de Castro, Paula Gameiro, José L. F. C Lima, Carla Matos, and Salette Reis. Location and partition coefficients of anti-inflammatory drugs in EPC liposomes. a fluorescence quenching study using n-(9-anthroyloxy)-stearic probes. *Colloids and Surfaces A: Physicochemical and Engineering Aspects*, 190(1-2):205–212, 2001.

[156] J. F. Nagle and M. C. Wiener. Structure of fully hydrated bilayer dispersions. *Biochimica et Biophysica Acta (BBA) - Biomembranes*, 942(1):1–10, 1988.

[157] Bernd W. Koenig and Klaus Gawrisch. Specific volumes of unsaturated phosphatidylcholines in the liquid crystalline lamellar phase. *Biochimica et Biophysica Acta (BBA) - Biomembranes*, 1715(1):65–70, 2005.

[158] Bernard Kwok-Keung Fung and Lubert Stryer. Surface density determination in membranes by fluorescence energy transfer. *Biochemistry*, 17(24):5241–5248, 1978.

[159] P K Wolber and B S Hudson. An analytic solution to the förster energy transfer problem in two dimensions. *Biophysical journal*, 28(2):197–210, 1979.

[160] Céline Boutin, Hervé Desvaux, Marie Carrière, François Leteurtre, Nadège Jamin, Yves Boulard, and Patrick Berthault. Hyperpolarized ^{129}Xe NMR signature of living biological cells. *NMR in Biomedicine*, 24(10):1264–1269, 2011.

[161] Jagoda Sloniec, Matthias Schnurr, Christopher Witte, Ute Resch-Genger, Leif Schröder, and Andreas Hennig. Biomembrane interactions of functionalized cryptophane-a: Combined fluorescence and ^{129}Xe NMR studies of a bimodal contrast agent. *Chemistry – A European Journal*, 19(9):3110–3118, 2013.

[162] Werner M. Nau and Xiangyang Zhang. An exceedingly long-lived fluorescent state as a distinct structural and dynamic probe for supramolecular association: An exploratory study of host–guest complexation by cyclodextrins. *Journal of the American Chemical Society*, 121(35):8022–8032, 1999.

[163] Kannie W. Y. Chan, Guanshu Liu, Xiaolei Song, Heechul Kim, Tao Yu, Dian R. Arifin, Assaf A. Gilad, Justin Hanes, Piotr Walczak, Peter C. M. van Zijl, Jeff W. M. Bulte, and Michael T. McMahon. MRI-detectable pH nanosensors incorporated into hydrogels for in vivo sensing of transplanted-cell viability. *Nature Materials*, 12(3):268–275, 2013.

[164] Matthias Schnurr, Christopher Witte, and Leif Schröder. Functionalized ^{129}Xe as a potential biosensor for membrane fluidity. *Physical Chemistry Chemical Physics*, 15(34):14178–14181, 2013.

[165] Jörg Polzehl and Karsten Tabelow. Structural Adaptive Smoothing in Diffusion Tensor Imaging: The R Package dti. *Journal of Statistical Software*, 31(9):1–24, 2009.

[166] Burkhard Ludewig and Matthias W. Hoffmann. *Adoptive Immunotherapy: Methods and Protocols*. Springer Science & Business Media, 2005.

[167] Joseph R. Lakowicz. *Principles of Fluorescence Spectroscopy*. Springer, 2006.

[168] Ajuna Arora, H. Raghuraman, and Amitabha Chattopadhyay. Influence of cholesterol and ergosterol on membrane dynamics: a fluorescence approach. *Biochemical and Biophysical Research Communications*, 318(4):920–926, 2004.

[169] B. Bechinger. The structure, dynamics and orientation of antimicrobial peptides in membranes by multidimensional solid-state NMR spectroscopy. *Biochimica Et Biophysica Acta*, 1462(1-2):157–183, 1999.

[170] L. Jacob and M. Zasloff. Potential therapeutic applications of magainins and other antimicrobial agents of animal origin. *Ciba Foundation Symposium*, 186:197–223, 1994.

[171] L Yang, T A Harroun, T M Weiss, L Ding, and H W Huang. Barrel-stave model or toroidal model? a case study on melittin pores. *Biophysical Journal*, 81(3):1475–1485, 2001.

[172] K. He, S. J. Ludtke, H. W. Huang, and D. L. Worcester. Antimicrobial peptide pores in membranes detected by neutron in-plane scattering. *Biochemistry*, 34(48):15614–15618, 1995.

[173] Alexander Spaar, Christian Münster, and Tim Salditt. Conformation of peptides in lipid membranes studied by x-ray grazing incidence scattering. *Biophysical Journal*, 87(1):396–407, 2004.

[174] Robert S. Cantor. Size distribution of barrel-stave aggregates of membrane peptides: influence of the bilayer lateral pressure profile. *Biophysical Journal*, 82(5):2520–2525, 2002.

[175] Kim A. Brogden. Antimicrobial peptides: pore formers or metabolic inhibitors in bacteria? *Nature Reviews Microbiology*, 3(3):238–250, 2005.

[176] Yehonathan Pouny, Doron Rapaport, Amram Mor, Pierre Nicolas, and Yechiel Shai. Interaction of antimicrobial dermaseptin and its fluorescently labeled analogs with phospholipid membranes. *Biochemistry*, 31(49):12416–12423, 1992.

[177] M. Amiche, A. A. Seon, T. N. Pierre, and P. Nicolas. The dermaseptin precursors: a protein family with a common preproregion and a variable c-terminal antimicrobial domain. *FEBS letters*, 456(3):352–356, 1999.

[178] Alison J. Moore, Wayne D. Beazley, Michael C. Bibby, and Deirdre A. Devine. Antimicrobial activity of cecropins. *Journal of Antimicrobial Chemotherapy*, 37(6):1077–1089, 1996.

[179] V. C. Kalfa, H. P. Jia, R. A. Kunkle, P. B. McCray, B. F. Tack, and K. A. Brogden. Congeners of SMAP29 kill ovine pathogens and induce ultrastructural damage in bacterial cells. *Antimicrobial Agents and Chemotherapy*, 45(11):3256–3261, 2001.

[180] Satoru Yamaguchi, Teresa Hong, Alan Waring, Robert I. Lehrer, and Mei Hong. Solid-state NMR investigations of peptide-lipid interaction and orientation of a beta-sheet antimicrobial peptide, protegrin. *Biochemistry*, 41(31):9852–9862, 2002.

[181] L Yang, T A Harroun, W T Heller, T M Weiss, and H W Huang. Neutron off-plane scattering of aligned membranes. i. method of measurement. *Biophysical Journal*, 75(2):641–645, 1998.

[182] A S Ladokhin, M E Selsted, and S H White. Sizing membrane pores in lipid vesicles by leakage of co-encapsulated markers: pore formation by melittin. *Biophysical Journal*, 72(4):1762–1766, 1997.

[183] J. H. Kang, S. Y. Shin, S. Y. Jang, M. K. Lee, and K. S. Hahm. Release of aqueous contents from phospholipid vesicles induced by cecropin a (1-8)-magainin 2 (1-12) hybrid and its analogues. *The Journal of Peptide Research: Official Journal of the American Peptide Society*, 52(1):45–50, 1998.

[184] K. Hristova, M. E. Selsted, and S. H. White. Critical role of lipid composition in membrane permeabilization by rabbit neutrophil defensins. *The Journal of Biological Chemistry*, 272(39):24224–24233, 1997.

[185] Ming-Tao Lee, Tzu-Lin Sun, Wei-Chin Hung, and Huey W. Huang. Process of inducing pores in membranes by melittin. *Proceedings of the National Academy of Sciences*, 110(35):14243–14248, 2013.

[186] K Matsuzaki, S Yoneyama, and K Miyajima. Pore formation and translocation of melittin. *Biophysical Journal*, 73(2):831–838, 1997.

[187] T. D. Lockey and D. D. Ourth. Formation of pores in escherichia coli cell membranes by a cecropin isolated from hemolymph of heliothis virescens larvae. *European journal of biochemistry / FEBS*, 236(1):263–271, 1996.

[188] H Duclohier, G Molle, and G Spach. Antimicrobial peptide magainin i from xenopus skin forms anion-permeable channels in planar lipid bilayers. *Biophysical Journal*, 56(5):1017–1021, 1989.

[189] Huey W. Huang. Molecular mechanism of antimicrobial peptides: The origin of cooperativity. *Biochimica et Biophysica Acta (BBA) - Biomembranes*, 1758(9):1292–1302, 2006.

[190] Garry K. Seward, Yubin Bai, Najat S. Khan, and Ivan J. Dmochowski. Cell-compatible, integrin-targeted cryptophane-^{129}Xe NMR biosensors. *Chem. Sci.*, 2(6):1103–1110, 2011.

[191] Olena Taratula and Ivan J Dmochowski. Functionalized ^{129}Xe contrast agents for magnetic resonance imaging. *Current Opinion in Chemical Biology*, 14(1):97–104, 2010.

[192] Daniela Delli Castelli, Enzo Terreno, Dario Longo, and Silvio Aime. Nanoparticle-based chemical exchange saturation transfer (CEST) agents. *NMR in biomedicine*, 26(7):839–849, 2013.

[193] Kannie W. Y. Chan, Tao Yu, Yuan Qiao, Qiang Liu, Ming Yang, Himatkumar Patel, Guanshu Liu, Kenneth W. Kinzler, Bert Vogelstein, Jeff W. M. Bulte, Peter C. M. van Zijl, Justin Hanes, Shibin Zhou, and Michael T. McMahon. A diaCEST MRI approach for monitoring liposomal accumulation in tumors. *Journal of Controlled Release*, 180:51–59, 2014.

[194] Ines Sauer, Heike Nikolenko, Sandro Keller, Khalid Abu Ajaj, Michael Bienert, and Margitta Dathe. Dipalmitoylation of a cellular uptake-mediating apolipoprotein e-derived peptide as a promising modification for stable anchorage in liposomal drug carriers. *Biochimica et biophysica acta*, 1758(4):552–561, 2006.

[195] Karl Sydow, Vladimir P. Torchilin, and Margitta Dathe. Lipopeptide-modified PEG-PE-based pharmaceutical nanocarriers for enhanced uptake in blood-brain barrier cells and improved cytotoxicity against glioma cells. *European Journal of Lipid Science and Technology*, 116(9):1174–1183, 2014.

[196] Eik Leupold, Heike Nikolenko, Michael Beyermann, and Margitta Dathe. Insight into the role of HSPG in the cellular uptake of apolipoprotein e-derived peptide micelles and liposomes. *Biochimica et biophysica acta*, 1778(12):2781–2789, 2008.

[197] N. Joan Abbott, Adjanie A. K. Patabendige, Diana E. M. Dolman, Siti R. Yusof, and David J. Begley. Structure and function of the blood-brain barrier. *Neurobiology of Disease*, 37(1):13–25, 2010.

[198] Sietze Reitsma, Dick W. Slaaf, Hans Vink, Marc A. M. J. van Zandvoort, and Mirjam G. A. oude Egbrink. The endothelial glycocalyx: composition, functions, and visualization. *Pflugers Archiv*, 454(3):345–359, 2007.

[199] Robert J. Hunter. *Zeta Potential in Colloid Science: Principles and Applications*. Academic Press, 1981.

[200] Eik Leupold, Heike Nikolenko, and Margitta Dathe. Apolipoprotein e peptide-modified colloidal carriers: the design determines the mechanism of uptake in vascular endothelial cells. *Biochimica et biophysica acta*, 1788(2):442–449, 2009.

[201] Andre E. Nel, Lutz Mädler, Darrell Velegol, Tian Xia, Eric M. V. Hoek, Ponisseril Somasundaran, Fred Klaessig, Vince Castranova, and Mike Thompson. Understanding biophysicochemical interactions at the nano-bio interface. *Nature Materials*, 8(7):543–557, 2009.

[202] Sören Gehne, Karl Sydow, Margitta Dathe, and Michael U. Kumke. Characterization of cell-penetrating lipopeptide micelles by spectroscopic methods. *The Journal of Physical Chemistry B*, 117(46):14215–14225, 2013.

[203] H. B. Mann and D. R. Whitney. On a test of whether one of two random variables is stochastically larger than the other. *The Annals of Mathematical Statistics*, 18(1):50–60, 1947.

[204] Silvio Aime, Carla Carrera, Daniela Delli Castelli, Simonetta Geninatti Crich, and Enzo Terreno. Tunable imaging of cells labeled with MRI-PARACEST agents. *Angewandte Chemie International Edition*, 44(12):1813–1815, 2005.

[205] Patrick M. Winter. Magnetic resonance chemical exchange saturation transfer imaging and nanotechnology. *Wiley Interdisciplinary Reviews: Nanomedicine and Nanobiotechnology*, 4(4):389–398, 2012.

[206] Guanshu Liu, Matthew Moake, Yah-el Har-el, Chris M. Long, Kannie W.Y. Chan, Amanda Cardona, Muksit Jamil, Piotr Walczak, Assaf A. Gilad, George Sgouros, Peter C.M. van Zijl, Jeff W.M. Bulte, and Michael T. McMahon. In vivo multicolor molecular MR imaging using diamagnetic chemical exchange saturation transfer liposomes. *Magnetic Resonance in Medicine*, 67(4):1106–1113, 2012.

[207] Kannie W.Y. Chan, Jeff W.M. Bulte, and Michael T. McMahon. Diamagnetic chemical exchange saturation transfer (diaCEST) liposomes: physicochemical properties and imaging applications. *Wiley Interdisciplinary Reviews: Nanomedicine and Nanobiotechnology*, 6(1):111–124, 2014.

[208] Peggy P. Hsu and David M. Sabatini. Cancer cell metabolism: Warburg and beyond. *Cell*, 134(5):703–707, May 2008.

[209] Gerty Schreibelt, Jack van Horssen, Saskia van Rossum, Christine D. Dijkstra, Benjamin Drukarch, and Helga E. de Vries. Therapeutic potential and biological role of endogenous antioxidant enzymes in multiple sclerosis pathology. *Brain Research Reviews*, 56(2):322–330, December 2007.

[210] Jianming Zhang, Priscilla L. Yang, and Nathanael S. Gray. Targeting cancer with small molecule kinase inhibitors. *Nature Reviews Cancer*, 9(1):28–39, 2009.

[211] Bart De Strooper, Robert Vassar, and Todd Golde. The secretases: enzymes with therapeutic potential in alzheimer disease. *Nature Reviews Neurology*, 6(2):99–107, 2010.

[212] Carlos López-Otín and Tony Hunter. The regulatory crosstalk between kinases and proteases in cancer. *Nature Reviews Cancer*, 10(4):278–292, 2010.

[213] Kim Naylor and Richard Eastell. Bone turnover markers: use in osteoporosis. *Nature Reviews Rheumatology*, 8(7):379–389, 2012.

[214] Qian Wei, Garry K. Seward, P. Aru Hill, Brian Patton, Ivan E. Dimitrov, Nicholas N. Kuzma, and Ivan J. Dmochowski. Designing ^{129}Xe NMR biosensors for matrix metalloproteinase detection. *Journal of the American Chemical Society*, 128(40):13274–13283, 2006.

[215] Mikhail V. Rekharsky, Young Ho Ko, N. Selvapalam, Kimoon Kim, and Yoshihisa Inoue. Complexation thermodynamics of cucurbit[6]uril with aliphatic alcohols, amines, and diamines. *Supramolecular Chemistry*, 19(1-2):39–46, 2007.

[216] Mustapha El Haouaj, Michel Luhmer, Young Ho Ko, Kimoon Kim, and Kristin Bartik. NMR study of the reversible complexation of xenon by cucurbituril. *Journal of the Chemical Society, Perkin Transactions 2*, (5):804–807, 2001.

[217] Jörg Döpfert, Christopher Witte, Martin Kunth, and Leif Schröder. Sensitivity enhancement of (hyper-)CEST image series by exploiting redundancies in the spectral domain. *Contrast Media & Molecular Imaging*, 9(1):100–107, 2014.

[218] Jörg Döpfert, Christopher Witte, and Leif Schröder. Fast gradient-encoded CEST spectroscopy of hyperpolarized xenon. *ChemPhysChem*, 15(2):261–264, 2014.

[219] Marion M. Bradford. A rapid and sensitive method for the quantitation of microgram quantities of protein utilizing the principle of protein-dye binding. *Analytical Biochemistry*, 72(1-2):248–254, 1976.

[220] Chang Wang, Martin R. Krause, and Steven L. Regen. Push and pull forces in lipid raft formation: The push can be as important as the pull. *Journal of the American Chemical Society*, 2015.

[221] Michael R. Yeaman and Nannette Y. Yount. Mechanisms of antimicrobial peptide action and resistance. *Pharmacological Reviews*, 55(1):27–55, 2003.

[222] August Andersson, Henrik Biverståhl, Jon Nordin, Jens Danielsson, Emma Lindahl, and Lena Mäler. The membrane-induced structure of melittin is correlated with the fluidity of the lipids. *Biochimica et Biophysica Acta (BBA) - Biomembranes*, 1768(1):115–121, 2007.

[223] Vladimir P. Torchilin. Multifunctional nanocarriers. *Advanced Drug Delivery Reviews*, 64, Supplement:302–315, 2012.

[224] Irène Brigger, Catherine Dubernet, and Patrick Couvreur. Nanoparticles in cancer therapy and diagnosis. *Advanced Drug Delivery Reviews*, 64, Supplement:24–36, 2012.

[225] Tiago B. Rodrigues, Eva M. Serrao, Brett W. C. Kennedy, De-En Hu, Mikko I. Kettunen, and Kevin M. Brindle. Magnetic resonance imaging of tumor glycolysis using hyperpolarized ^{13}C-labeled glucose. *Nature Medicine*, 20(1):93–97, 2014.

List of Figures

List of Tables

A

Pixelwise DeLTA of Figure 4.12

The depolarization time map shown in Figure 4.12 is obtained by analyzing each pixel by DeLTA. On the following two pages the depolarization time distributions of all pixels that cover the two nested NMR tubes are shown.

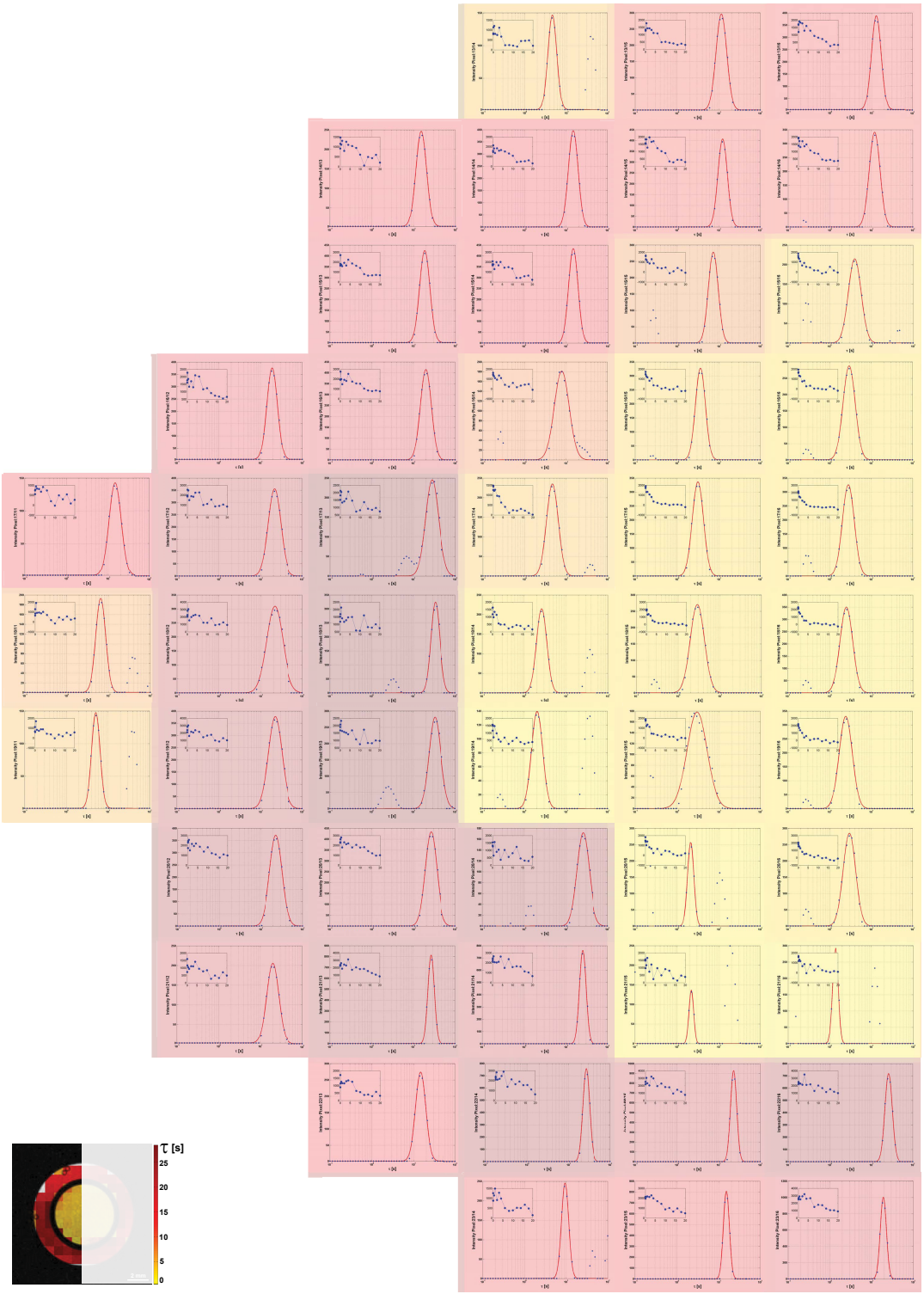

Figure A.1 – Pixelwise DelTA of the two nested NMR tubes (left half). For each pixel DeLTA was performed which yielded a depolarization time distribution. The superimposed colors represent the maximum depolarization time of each pixel. Reproduced from reference [164]. Copyright ©2013 Royal Society of Chemistry.

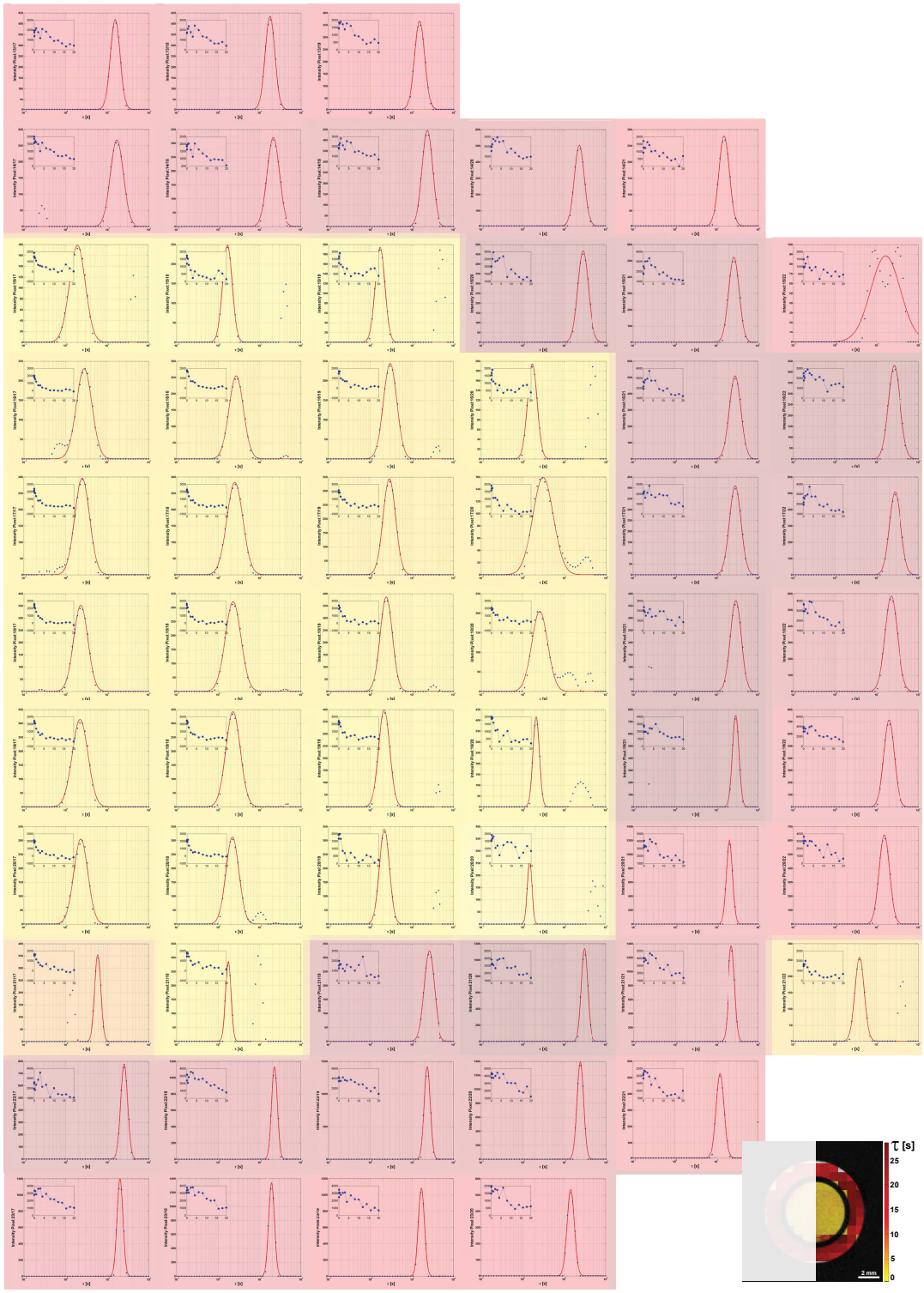

Figure A.2 – Pixelwise DelTA of the two nested NMR tubes (right half). For each pixel DeLTA was performed which yielded a depolarization time distribution. The superimposed colors represent the maximum depolarization time of each pixel. Reproduced from reference [164]. Copyright ©2013 Royal Society of Chemistry.

B

DeLTA MATLAB routine

```
%
%%%%%%%%%%%%%%%%%%%%%%%%%%%%%%%%%%%%%%%%%%%%%%%%%%%%%%%%%%%%%%%%%%%%%%%%%%%%%%%
%  DeLTA to analyse depolarization processes
%%%%%%%%%%%%%%%%%%%%%%%%%%%%%%%%%%%%%%%%%%%%%%%%%%%%%%%%%%%%%%%%%%%%%%%%%%%%%%%
%
%  Choose experimental data from folder "999", generated by bruker.
%
%  Set a big range of the lower und upper limit. To easily check where the
%  maxima constants are.
%
%  by M. Schnurr (2015/01/13).
%
%%%%%%%%%%%%%%%%%%%%%%%%%%%%%%%%%%%%%%%%%%%%%%%%%%%%%%%%%%%%%%%%%%%%%%%%%%%%%%%
%%%%%%%%%%%%%%%%%%%%%%%%%%%%%%%%%%%%%%%%%%%%%%%%%%%%%%%%%%%%%%%%%%%%%%%%%%%%%%%
%%%%%%%%%%%%%%%%%%%%%%%%%%%%%%%%%%%%%%%%%%%%%%%%%%%%%%%%%%%%%%%%%%%%%%%%%%%%%%%
%% Choose saturation data in raw file and corresponding vdlist

% choose an apropriate Filename under which the data will be saved
filename='FileXY';

% get y-data from a raw data file via the routine "rbnmr"
Datafolder = uigetdir('E:','Choose data');
cd(Datafolder);
rbnmr=rbnmr;

% write y-Data in a new structure
data.YdataB=rbnmr.Data;

% get corresponding x-data automatically (t_sat)
cd ../..;
data.XdataB = importdata('vdlist');
```

```
% To get the correct t_sat, choose every second entry from the data file
hlength=(length(data.XdataB))/2;
for k = 2:hlength
    data.Xdata(k-1,1) = data.XdataB(2*k,1);
end

% delete filled zeros in y-data at the end of the file
for k = 2:hlength
    data.Ydata(k-1,1) = data.YdataB(k,1);
end

% clear temporarily used variables in struct "data"
data=rmfield(data,'XdataB');
data=rmfield(data,'YdataB');

% normalize data and write into column 2
data.Ydata(:,2)=data.Ydata(:,1)/(mean(data.Ydata(1:2,1)));

% save original data to the structure {Tsat}
Tsat.(filename)=data;

% clear some variables
clear fnameY fnameX path ans k hlength data.YdataB data.XdataB

% plot the original data
figure
semilogy(data.Xdata(1:end,1),data.Ydata(1:end,2),'-o','Color','b');
title('Experimental decay data')
xlabel('t_{sat} [s]')
ylabel('Normalized Signal')
set(gcf,'Color',[1 1 1])
ylim([0.01 1.05])

%% Beginning of routine rilt.m

close all
for i=1:6
filename=['FileXY',num2str(i)];

%%%%%%%%%%%%%%%%%%%%%%%%%%%%%%%%%%%%%%%%%%%%%%%%%%%%%%%%%%%%%%%%%%%%%%%%%%%%%%%
%%%%%%%%%%%%%%%%%%%%%%%%%%%%%%%%%%%%%%%%%%%%%%%%%%%%%%%%%%%%%%%%%%%%%%%%%%%%%%%
%%%%%%%%%%%%%%%%%%%%%%%%%%%%%%%%%%%%%%%%%%%%%%%%%%%%%%%%%%%%%%%%%%%%%%%%%%%%%%%
% Definition of parameters and variables
```

```
clear g g0 s s0 s_new g_new
l = -2 ; % lower limit 10^l in s-space
u = 1.5; % upper limit 10^u in s-space
numPoints = 25; % initial number of points in s-space
loops = 4; % number of increments to increase the resolution (see below)

alpha = 0.05; % alpha value
% comment to alpha:
% In this script the second derivative of g is minimized with
% weight alpha^2 ("principle of parsimony"): hor high alpha
% values, the output g distribution will be smooth and
% regular. For alpha==0, the output g distribution will
% be totally 'free'.

% arbitrary target function for the routine to start with:
% (starting point for the routine):
 A1=15;
 A2=3971;
 sigma1=0.1;
 mean1=15;
 sigma2=0.01;
 mean2=2;
s = logspace(l,u,numPoints)';
for x=1:length(s);
g0(x)=A1/(sqrt(2*pi)*sigma1)*exp(-(s(x)-mean1)^2/(2*sigma1^2)) + ...
      A2/(sqrt(2*pi)*sigma2)*exp(-(s(x)-mean2)^2/(2*sigma2^2));
end

% initial s space with lower and upper limit
s0  = logspace(l,u,length(g0))';

% initial depolarization time distribution for the routine:
g = ones(size(s));

% read-in x and y data
xx = Tsat.(filename).Xdata(:,1);
yy = Tsat.(filename).Ydata(:,2);

% fitting weights
w=ones(length(xx),1);

%%%%%%%%%%%%%%%%%%%%%%%%%%%%%%%%%%%%%%%%%%%%%%%%%%%%%%%%%%%%%%%%%%%%%%%%%%%%%%%
%%%%%%%%%%%%%%%%%%%%%%%%%%%%%%%%%%%%%%%%%%%%%%%%%%%%%%%%%%%%%%%%%%%%%%%%%%%%%%%
%%%%%%%%%%%%%%%%%%%%%%%%%%%%%%%%%%%%%%%%%%%%%%%%%%%%%%%%%%%%%%%%%%%%%%%%%%%%%%%
```

```
% routine based on rilt.m
[g,yfit,cfg] =rilt(xx,yy,s,g,alpha,'logarithmic',[],[],'decay',{'g>0'},[],w);

% increase resolution of s and the arbitrary target function
for k =2:loops;
s_new = logspace(l,u,k*numPoints)';
s = s_new;

g0 = interp1(s,cfg.g0,s_new,'linear');%
% add noise to g0 and use the noisy g0 as a new arbitrary target function:
 for z=1:length(g0);
       noise(z) = randn(1)*0.01;
       g_new(z) = g0(z) * (1+noise(z));
 end
clear z noise
g=g_new';
g(1:3)=0; % boundary condition for small depolarization times
g(end-1:end)=0; % boundary condition for large depolarization times

% perform another rilt.m routine with the increased resolution of s and g
[g,yfit,cfg] =rilt(xx,yy,s,g,alpha,'logarithmic',[],[],'decay',{'g>0'},[],w);
cfg
clear s_new

%plot the intermediate result:
figure(5)
subplot(2,5,k)
s0  = logspace(l,u,length(g0))';
semilogx(s0,g0/max(g0),s,g/max(g),'o-');
title('g-target and g');

% Find Maximum in g(s) = DecayTime and write in output window
maxIndex = localMaximum(g,length(g)/4, true);
DecayTime.MaximumValue = g(maxIndex);
DecayTime.MaximumDecayTime = s(maxIndex);
disp('DecayTime =')
disp(DecayTime.MaximumDecayTime)
disp('k = ')
disp(k)

%%%%%%%%%%%%%%%%%%%%%%%%%%%%%%%%%%%%%%%%%%%%%%%%%%%%%%%%%%%%%%%%%%%%%%%%%%%%%%%
%%%%%%%%%%%%%%%%%%%%%%%%%%%%%%%%%%%%%%%%%%%%%%%%%%%%%%%%%%%%%%%%%%%%%%%%%%%%%%%
%%%%%%%%%%%%%%%%%%%%%%%%%%%%%%%%%%%%%%%%%%%%%%%%%%%%%%%%%%%%%%%%%%%%%%%%%%%%%%%
% end of routine based on rilt.m
```

```
end

%%%%%%%%%%%%%%%%%%%%%%%%%%%%%%%%%%%%%%%%%%%%%%%%%%%%%%%%%%%%%%%%%%%%%%%%%%%%%%%
%%%%%%%%%%%%%%%%%%%%%%%%%%%%%%%%%%%%%%%%%%%%%%%%%%%%%%%%%%%%%%%%%%%%%%%%%%%%%%%
%%%%%%%%%%%%%%%%%%%%%%%%%%%%%%%%%%%%%%%%%%%%%%%%%%%%%%%%%%%%%%%%%%%%%%%%%%%%%%%
%% Fitting of the depolarization time distribution

 s = Tsat.(filename).Decay.s;
 g = Tsat.(filename).Decay.g;

%%%%%%%%%%%%%%%%%%%%%%%%%%%%
% enter number of maximas to be fitted here:
numPeaks = 2;
%%%%%%%%%%%%%%%%%%%%%%%%%%%%
if numPeaks == 1;
    % fitting a normal distribution with one maximum
        [fitresult,gof, ci]=cf1peaks(s, g);
        s1=fitresult.s1;
        u1=fitresult.u1;
        Ds11 = (s1 - ci(1,2));
        Du11 = (u1 - ci(1,3));
        % calculate the maxima's properties
        peakprop.decayTime = exp(u1-s1^2);
        peakprop.decayTimeUpper = exp(u1-s1^2)*sqrt(Du11^2+(2*s1*Ds11)^2);
        peakprop.FWHM = sqrt(exp(2*u1+s1^2)*(exp(s1^2)-1));
        peakprop

elseif numPeaks == 2;
    % fitting two normal distributed maxima
        [fitresult,gof]=cf2peaks(s, g);
        s1=fitresult.s1;
        u1=fitresult.u1;
        s2=fitresult.s2;
        u2=fitresult.u2;
        % calculate the maximas' properties
        peakprop.decayTime1 = exp(u1-s1^2); % MODE of log norm distribution
        peakprop.FWHM1 = 2*sqrt(2*log(2))*sqrt(exp(2*u1+s1^2)*(exp(s1^2)-1)); %FWHM = factor *
        peakprop.decayTime2 = exp(u2-s2^2);
        peakprop.FWHM2 = 2*sqrt(2*log(2))*sqrt(exp(2*u2+s2^2)*(exp(s2^2)-1));
        peakprop

else
    disp('warning: numPeaks > 2.')
end
```

```
% save all the data in the structure {Tsat}:
Tsat.(filename).Decay.alpha=alpha;
Tsat.(filename).Decay.s=s;
Tsat.(filename).Decay.g=g;
Tsat.(filename).Decay.gof=gof;
Tsat.(filename).Decay.peakprop=peakprop
Tsat.(filename).Decay.yfit=yfit;
Tsat.(filename).Decay.fitresult=fitresult;
Tsat.(filename).Decay.x=xx;
Tsat.(filename).Decay.y=yy;
title(filename)

% save figures
saveas(gcf, filename, 'epsc')
saveas(gcf, filename, 'fig')



end
```

C

Publications

Parts of this thesis are already published in scientific journals. The publications, which are listed below, include three first author articles ([P2], [P3] and [P5]), one first author book chapter ([B1]), one shared first author article ([P1]) and one co-author article ([P4]). The work was additionally presented on conferences by talks ([T1] – [T4]) and peer-reviewed poster presentations ([p1] – [p5]).

Publications

[P1] Jagoda Sloniec[$], Matthias Schnurr[$], Christopher Witte, Ute Resch-Genger, Leif Schröder, and Andreas Hennig
Biomembrane Interactions of Functionalized Cryptophane-A: Combined Fluorescence and ^{129}Xe NMR Studies of a Bimodal Contrast Agent
Chem. Eur. J. 19 (9), 3110 – 3118, **2013**
DOI: 10.1002/chem.201203773
([$] both authors contributed equally to this work)

[P2] Matthias Schnurr, Christopher Witte, and Leif Schröder
Functionalized ^{129}Xe as a Potential Biosensor for Membrane Fluidity
Phys. Chem. Chem. Phys. 15(34), 14178 – 14181, **2013**
DOI: 10.1039/C3CP51227D
(highlighted as inside front cover article)

[P3] Matthias Schnurr, Christopher Witte, and Leif Schröder
Depolarization Laplace transform analysis of exchangeable hyperpolarized ^{129}Xe for detecting ordering phases and cholesterol content of biomembrane models
Biophys. J. 106(6), 1301 – 1308, **2014**
DOI: 10.1016/j.bpj.2014.01.041

[P4] Stefan Klippel, Jörg Döpfert, Jabadurai Jayapaul, Martin Kunth, Federica Rossella, Matthias Schnurr, Christopher Witte, Christian Freund and Leif Schröder
Cell tracking with caged xenon: Using cryptophanes as MRI reporters upon cellular internalization
Angew. Chem. Int. Ed. 126 (2), 503 – 506, **2014**
DOI: 10.1002/anie.201307290
(highlighted as back cover article)

[P5] Matthias Schnurr, Karl Sydow, Honor May Rose, Margitta Dathe, and Leif Schröder
Brain endothelial cell targeting via a peptide-functionalized liposomal carrier for xenon Hyper-CEST MRI
Adv. Healthcare Mater. 4(1), 40 – 45, **2015**
DOI: 10.1002/adhm.201400224
(highlighted as front cover article)

[B1] Matthias Schnurr, Christopher Witte, and Leif Schröder
Caged Xenon in Phospholipid Membrane Environments
New Developments in NMR: Hyperpolarized Xenon-129 Magnetic Resonance – Concepts, Production, Techniques and Applications, 288 – 300, **2015**
Edited by Thomas Meersmann and Eike Brunner
Royal Society of Chemistry
ISBN: 978-1-84973-889-7

Talks

[T1] Matthias Schnurr, Christopher Witte, and Leif Schröder
Investigating biomembrane models using Xenon Hyper-CEST
2nd COST Action TD1103 EuroHyperPol (European Network for Hyperpolarisation Physics and Methodology in NMR and MRI), Working group: Chemistry-Physics Interface, Hersonissos, Greece, Jun 28 – 29 2013

[T2] Matthias Schnurr
Caged xenon in membrane environments for MRI contrast
1st FMP NMR retreat, Brückentinsee, Germany, Oct 28 – 30 2013

[T3] Matthias Schnurr, Karl Sydow, Honor May Rose, Margitta Dathe, and Leif Schröder
Xenon Hyper-CEST MRI of nanocarrier-targeted brain endothelial cells
MDC/FMP Campus Symposium, Berlin, Germany, May 26 – 27 2014

[T4] Matthias Schnurr
Differences in antimicrobial peptide membrane interactions revealed with xenon Hyper-CEST
2nd FMP NMR retreat, Rheinsberg, Germany, Jun 10 – 12 2014

Poster presentations

[p1] Matthias Schnurr, Jagoda Sloniec, Christopher Witte, Ute Resch-Genger, Andreas Hennig, and Leif Schröder
Discriminating Biomembrane Compositions using Functionalized 129Xe via Hyper-CEST-NMR and FRET
14th joint PhD Retreat of MDC and FMP, Liebenwalde, Germany, Aug 30 – Sep 1 2012 (Abstract 57)

[p2] Matthias Schnurr, Christopher Witte, Jörg Döpfert, Martin Kunth, Stefan Klippel, Federica Rossella, Jabadurai Jayapaul, and Leif Schröder
High-sensitivity hyperpolarized 129Xe-NMR for detecting differences in biomembrane fluidity
64. Mosbacher Kolloquium - Membranes in Motion, Mosbach, Germany, Apr 4 – 6 2013 (Abstract O8)

[p3] Matthias Schnurr, Jörg Döpfert, Martin Kunth, Christopher Witte, and Leif Schröder
Depolarization-Time Mapping of Functionalized ^{129}Xe in Biomembranes Possessing Different Fluidity
54th ENC, Asilomar, CA, USA, Apr 14 – 19 2013 (Abstract 299)

[p4] Matthias Schnurr, Christopher Witte, and Leif Schröder
Investigating biomembrane models using Xenon Hyper-CEST
EUROMAR 2013, Hersonissos, Greece, Jun 30 – Jul 05 2013 (Abstract 554 TH)

[p5] Matthias Schnurr, Christopher Witte, and Leif Schröder
Discrimination of Differences in Membrane Cholesterol Content using ^{129}Xe Hyper-CEST
1st FMP NMR retreat, Brückentinsee, Germany, Oct 28 – 30 2013 (no abstract available)

[p6] Matthias Schnurr, Karl Sydow, Honor May Rose, Margitta Dathe, and Leif Schröder
A peptide-modified liposomal carrier for selective cell labeling via Hyper-CEST MRI
World Molecular Imaging Congress, Seoul, Korea, Sep 17 – 20 2014 (Abstract P357)

[p7] Matthias Schnurr, Christopher Witte, and Leif Schröder
Cell-selective Hyper-CEST MRI using targeted liposomes
36th Discussion Meeting of the Magnetic Resonance Spectroscopy division of the German Chemical Society, Berlin, Germany, Sep 29 – Oct 02 2014 (Abstract P96)

D

Curriculum vitae

For reasons of data protection, the curriculum vitae is not included in the online version.

E

Acknowledgments

For reasons of data protection, the acknowledgments are not included in the online version.